Dynamics of dense non-Brownian suspensions under impact

Pradipto

2022

Acknowledgements

I would like to express my appreciation to my supervisor, Prof. Hisao Hayakawa for his critical comments and discussions during the progress of this research, including the writings of the papers and this thesis. I would like to thank Prof. Ryohei Seto and Dr. Satoshi Takada for a lot of fruitful discussions with them. I also thank Prof. Hiroaki Katsuragi for his insights on the early stages of this thesis, and Prof. Michio Otsuki and Prof. Tetsuo Yamaguchi for their useful comments. I would also like to express my gratitude to Prof. Takenobu Nakamura for the discussions regarding persistent homology analysis. I also thank Dr. Amit Kumar Chatterjee for his critical reading of this thesis. Then, I would also like to acknowledge Dr. Alessandro Leonardi for sharing his lattice Boltzmann with free surface code.

I would like to thank the Ministry of Education, Culture, Sports, Science and Technology of Japan (MEXT) for providing the scholarship and allowance throughout my stay in Japan. This research is partially supported by Grants-in-Aid of MEXT, Japan for Scientific Research, Grant Nos. JP16H04025 and JP21H01006. This thesis is also partially supported by ISHIZUE 2020 of Kyoto University Research Development Program. Most of the numerical calculations were carried out at the Yukawa Institute for Theoretical Physics (YITP) Computer Facilities, Kyoto University, Japan. I am also grateful to all supporting staffs of Yukawa Institute for Theoretical Physics (YITP) and Division of Physics and Astronomy, Graduate School of Science, Kyoto University for their kind support.

I am grateful to my lab mate Daisuke Ishima and colleague Kiwamu Yoshii for the discussions, and to other current and previous lab mates, Dr. Ville M. M. Paasonen, Yuki Hino, Dr. Hiroyasu Tajima, Dr. Yu Watanabe, and Kazuhito Kuramoto for their insights and moral supports. Finally, I would like to express my gratitude for my family and friends in Indonesia, Kyoto, and other places around the world for their endless support and encouragement.

Abstract

We numerically and theoretically study the transient response of dense non-Brownian suspensions under impacts. We use the coupled lattice Boltzmann and discrete element method (LBM-DEM) simulation for dense suspensions. First, we investigate a free-falling impactor into dense suspensions and focus on the elastic rebound and investigate its parameter dependences. We find that the rebound depends on the impact speed, the volume fraction of the suspensions, and frictional contact between suspended particles. We then visualize local quantities inside the suspensions after the impact. We find a region with high normal stress but no high shear stress is observed after the impact, opposite to what was observed in the discontinuous shear thickening (DST). Then, we analyze the topological structure of the contact network between suspended particles using persistent homology. Second, we propose a simple phenomenology called the floating + force chain model that captures the viscoelastic response of the impact process. We observe power-law relationships among the impact velocity, the maximum force exerted on the impactor, and the time to reach the maximum force on high impact speed, which can be solely explained by the viscous process while percolating force chains are necessary to recover the elastic rebound. Third, we delineate the dynamically jammed region (DJR) induced by the impact and quantify its viscosity and elasticity. Using the contributions from the DJR, elastic response can be recovered even without percolating force chains. Finally, we discuss the impact of a foot-spring-body system to mimic the hopping motion on dense suspensions.

Publication list for requirement of this thesis

1. Pradipto and Hisao Hayakawa
   "Impact-induced hardening in dense frictional suspensions"
   Phys. Rev. Fluids, **6**, 033301 (2021). (Chapter 3)

2. Pradipto and Hisao Hayakawa
   "Viscoelastic response of the impact process on dense suspensions"
   Phys. Fluids., **33**, 093110 (2021). (Chapter 4)

3. Pradipto and Hisao Hayakawa
   "Effective viscosity and elasticity of dynamically jammed region and their role for the hopping motion on dense suspensions"
   Submitted to Phys. Rev. E. (Chapter 5)

Reference papers

1. Pradipto and Hisao Hayakawa
   "Simulation of dense non-Brownian suspensions with the lattice Boltzmann method: shear jammed and fragile states"
   Soft Matter, **16**, 945 (2020).

Table of contents

Chapter 1

Introduction

1.1 Non-Brownian Suspensions

Mixtures are physical combinations of two or more substances. It is interesting to understand the physics of such mixtures since they yield different behavior compared to their constituents alone. In this thesis, we are interested in mixtures of solid particles and fluid solvents. The size of the particles can dictate how these mixtures behave (See Fig. 1.1). If the particles are very small (less than 1 *nm*), they dissolve in the solvent and become a homogenous mixture which is called a *solution*. A suspension is a heterogeneous mixture of solid solute particles and solvent medium, in which the solute particles do not dissolve but are suspended in the solvent and are floating around freely in the medium [11]. When the size of particles is ranged between 1 *nm* and 1 μm, the behavior is dictated by thermal agitations, which is a *Brownian (colloidal) suspension*. The interaction between charged colloidal particles is described by the Derjaguin-Landau-Verwey-Overbeek (DLVO) theory, including the effects of the van der Waals interactions and the electrostatic forces [25, 112], and the hydrodynamic interaction between colloidal particles. Finally, if the particle size is ranged between 1 μm and 100 μm, the Brownian effects are negligible. Therefore, only mechanical agitations are important to dictate the behavior of such systems. We denote them *non-Brownian suspensions* which are the systems of interest for this thesis.

Non-Brownian suspensions are ubiquitous in nature and in our daily life. The most popular example is the suspension of cornstarch in water. Cornstarch can be easily bought in supermarkets and most of us even have it in our kitchen. There are a lot of videos on YouTube that demonstrate the properties of cornstarch and water suspensions under mechanical disturbance. For example, hitting them with a hammer or people trying to run on top of it, in which the suspensions behave as solids right after the impacts and become fluid-like again afterwards. This phenomenon can also be utilized for industrial applications

such as protective vests, where the vests can become rigid in response to impacts of shooting, while otherwise remaining fluid-like and comfortable to wear [62]. This thesis focuses on this hardening behavior of dense suspensions under impact.

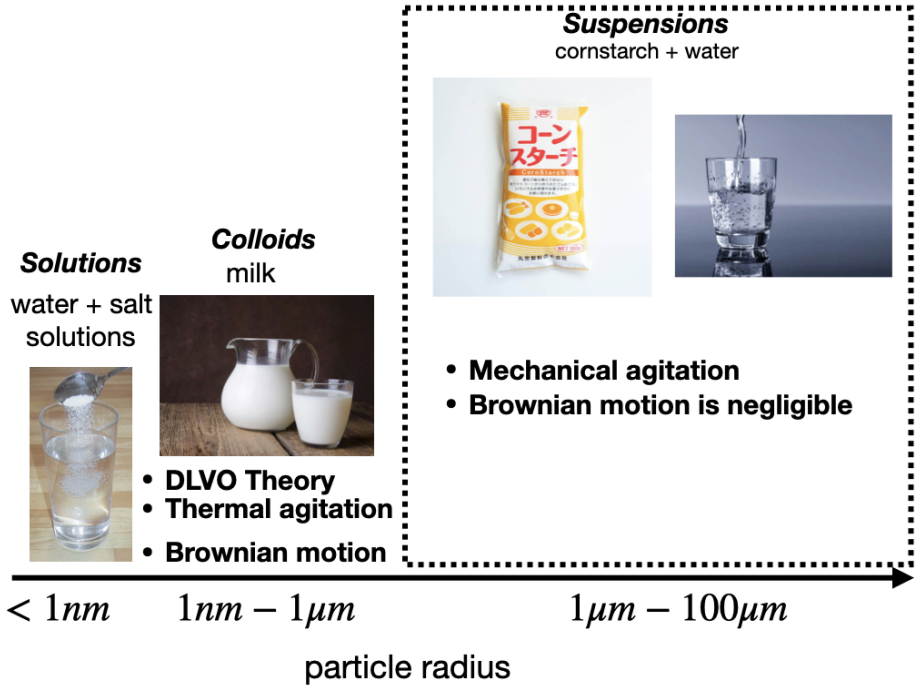

Fig. 1.1 Various kinds of heterogeneous mixtures based on the particle size, the mixtures within the scope of this thesis (suspensions) are confined by the dotted box.

1.2 Steady-state rheology of dense suspensions

In this section, we briefly review the current understanding regarding the steady-state rheology of dense suspensions. Rheology is a branch of physics that deals with the deformation and flow of materials. In many rheological experiments, the shear stress σ_{xy} is measured under the condition where steady simple shear is applied to the suspension with shear rate $\dot{\gamma}$. The viscosity η is defined as

$$\eta = \frac{\sigma_{xy}}{\dot{\gamma}}. \tag{1.1}$$

In other words, the viscosity η tells us how "hard" for the suspensions to flow. As one might expect, the suspended solid particles play an important role in determining η. Studies on how the solid particles affect the viscosity was initiated by Einstein in his seminal paper in

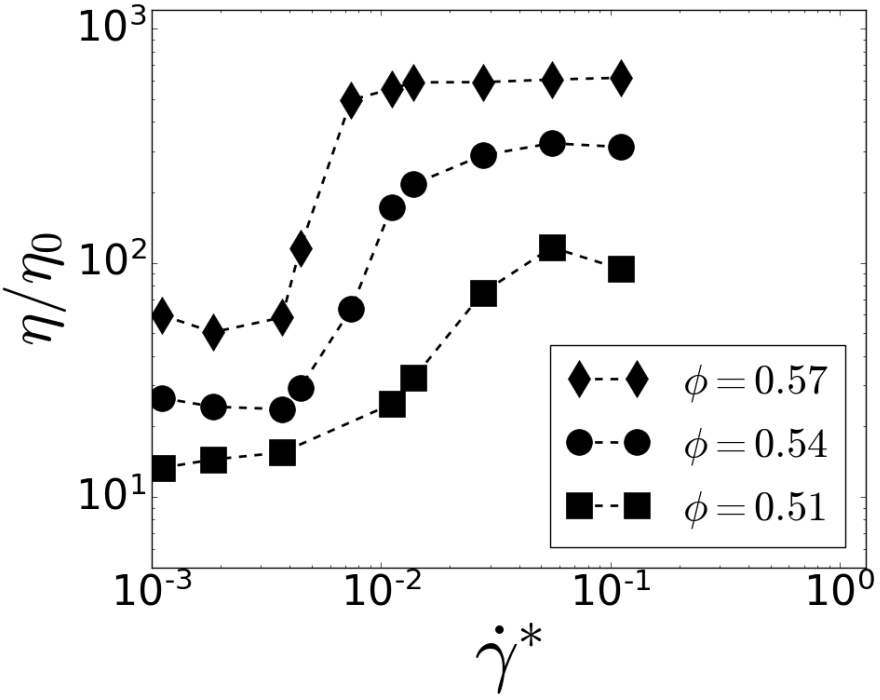

Fig. 1.2 Continuous ($\phi \leq 0.54$) and discontinuous ($\phi > 0.54$) shear thickenings of dense suspensions under simple shear in the numerical simulation.

1905 [28]. The obtained viscosity for dilute suspensions in Ref. [28] is given by

$$\frac{\eta}{\eta_0} = 1 + \frac{5\phi}{2} + O(\phi^2), \tag{1.2}$$

where η_0 is the viscosity of the solvent and ϕ is the volume fraction of the suspended particles. There is a certain fraction $\phi = \phi_J$ beyond which the suspensions cannot flow anymore i.e. jammed, where ϕ_J is the jamming fraction. Thus, viscosity diverges with ϕ approaching ϕ_J as

$$\eta \propto \left(1 - \frac{\phi}{\phi_J}\right)^{-\lambda}, \tag{1.3}$$

where the exponent λ has been shown to be $\lambda \approx 2$ [54, 72, 105].

For Newtonian fluids, the viscosity is independent of the shear rate and is regarded as an intrinsic material parameter. This is not the case for suspensions, where the rheological behavior is non-Newtonian in which the apparent viscosity η depends on the shear rate. In some cases, the viscosity may decrease as the shear-rate increases, which is called shear thinning. In another case, the viscosity increases as the shear rate increases. Such a phenomenon is denoted as a shear thickening. The shear thickening can be further categorized

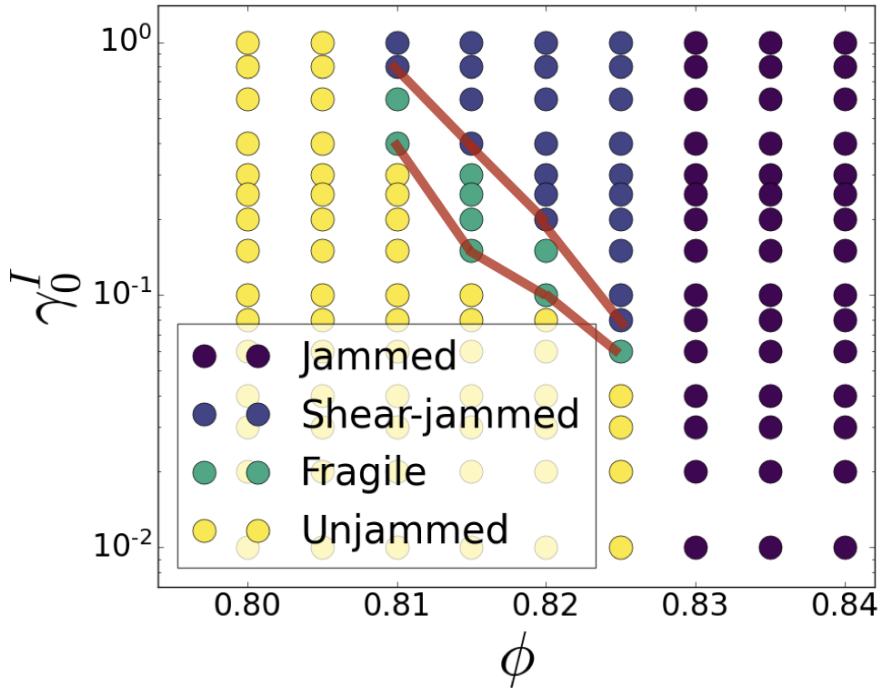

Fig. 1.3 Phase diagram on the plane of the control parameters ϕ and γ_0^I (initial strain amplitude) for monolayer dense suspensions under oscillatory shear. The lines represent the occurrences of DST-like phenomena.

into two cases: one is the continuous shear thickening (CST) and the other is the discontinuous shear thickening (DST) (See Fig. 1.2). The DST is an abrupt increase of the apparent viscosity at a critical shear rate $\dot{\gamma}_c$ if the volume fraction of the solvent is larger than the critical value ϕ_c. It is noteworthy that such DST also takes place in an assembly of dry frictional granular particles under a simple shear [83]. We also note that DST-like discontinuous change of the viscosity can be observed in dilute inertial suspensions [49, 37, 111, 100, 50, 49, 30, 97, 1, 98, 38, 108].

The DST has been extensively studied experimentally [116, 3, 27, 17, 15, 23]. Since it is not easy to visualize suspended particles, insights regarding the microscopic mechanism of DST are gained through numerical simulations [101, 72, 73, 87]. Seto and his coworkers confirmed the role of the mutual friction between particles for the DST in the non-Brownian[101, 72] and Brownian suspensions[73] as in the case of dry granular materials [83]. Extensive reviews along this line have been published in Refs. [16, 24, 80]. On the theoretical side, the phenomenological Wyart-Cates (WC) model that is based on the fraction of frictional contact between particles is widely used in many cases [117, 103, 36]. References [110] analyzed the force in the correlations in the dual of the position space and found a relationship between DST and the anisotropy of the stress tensor. Then, Ref. [87]

reproduced the viscosity using a phenomenology based on the angular distribution of the contact forces.

As mentioned earlier, the viscosity diverges if the suspension is jammed. Jammed systems do not flow under applied stresses, whereas unjammed systems flow under any applied stresses [67, 68]. The jamming transition between unjammed and jammed states should be distinguished from the temperature-driven glass transition. For frictionless monodisperse spheres in the zero shear limit, the jamming occurs at $\phi_J \approx 0.64$, close to the random close packing (RCP) of identical spheres in a box. Once the system is jammed, it behaves as a solid and its mechanical response of it is expressed as

$$G = \frac{\sigma_{xy}}{\gamma}, \tag{1.4}$$

where G and γ are the shear modulus and strain, respectively. In other words, G must be non-zero if the system is jammed. In two-dimensional dry frictional granular particles, the system goes through two new different states as one increases the applied stress at $\phi_S < \phi_J$ [7, 84]: (i) Fragile state, where the system can only sustain load in one direction and (ii) shear jammed state, where the system can sustain load in all directions [84]. Shear jammed state has also been observed in dense suspensions experimentally under a steady shear [86], and numerically under an oscillatory shear [87], where both studies suggest that DST correspond to the fragile states (Fig. 1.3).

1.3 Transient dynamics of dense suspensions

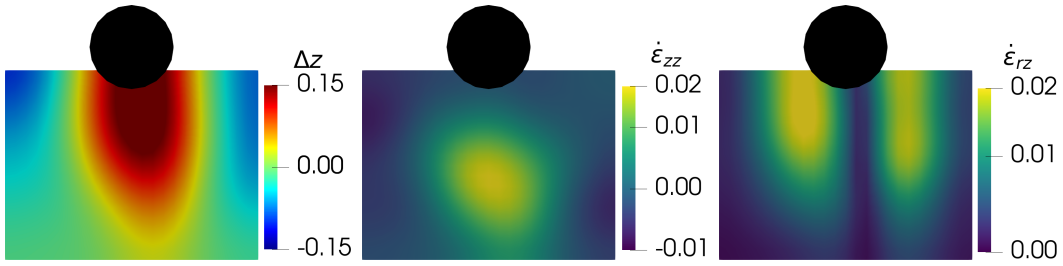

(a) (b) (c)

Fig. 1.4 (a) The displacement field of dense suspensions undergoing an impact. (b) The strain-rate fields of dense suspensions under impact in vertical direction. (c) The strain-rate fields of dense suspensions under impact in lateral direction.

A typical example of the hardening behaviour of dense suspensions is that a running person can stay afloat on the top of suspensions. Once the person starts to walk or stop running, the person sinks into the suspensions. The DST is often used to explain such an impact-induced hardening [62, 2, 79]. There are, however, several differences between the two processes. One is that the impact-induced hardening is the process to have large normal stress with small shear stress, while the DST is the process to get a discontinuous jump of both the shear stress and normal stress. Second, DST is a steady process while impact-induced hardening is a transient process. Thus, we believe that the explanation of the hardening process by using the DST is misleading. In this section, we review our current understanding of the transient response of dense suspensions. Surprisingly enough, the transient dynamics of dense suspensions are less studied than the steady-state ones.

The earliest experiments to investigate the response of dense suspensions under an impact used a free-falling impactor and discovered a solid-like region right beneath the impactor, while the other part remains fluid-like [114] (Fig. 1.4(a)). This adds another difference between the DST and the impact-induced hardening, where DST is homogeneous while impact-induced hardening is localized and inhomogeneous. Such region is called the *dynamically jammed region* (DJR), in which DJR was expected to have a higher volume fraction compared to the rest of the suspensions [115]. However, using high-speed ultrasound imaging, Ref. [34] discovered that there is no significant change in the volume fraction of the DJR. Thus, the DJR is not formed through compression. Moreover, they were also able to visualize the flow field inside the suspensions using particle-image velocimetry (PIV) and found that the strain rate peaked in the boundary of the DJR (Figs. 1.4(b) and 1.4(c)). They proposed that the mechanism behind the forming of the DJR is closely related to shear jamming. Such a picture is then extended to discuss the transient behavior of suspensions under shear [35, 36]. However, due to the difficulties in visualizing the stress distribution and force propagation in experiments, little is still known about the mechanical properties such as the stress, viscosity, and rigidity of the DJR. Therefore, numerical simulations for this problem are necessary.

For a free-falling impactor, one can discuss the relation between the impact speed u_0 and the maximum force acting on the impactor $F_{\max}$ or the elapsed time $t_{\max}$ to reach $F_{\max}$. Previous studies [13, 79, 114] showed the existence of power-law relations

$$F_{\max} \propto u_0^{\alpha}, \qquad t_{\max} \propto u_0^{\beta}. \tag{1.5}$$

Experiments observed that $\alpha \approx 1.5$ and $\beta \approx -0.5$. It is noteworthy that similar relations are also found in impact processes for dry granular materials [55]. To explain the motion of the impactor, Ref. [114] proposed a phenomenology called the added-mass model, where impact

on suspensions can be regarded as an inelastic collision between the impactor and a growing DJR. Added-mass model can be solved numerically and yields $\alpha = 2$ and $\beta = -1$ [79]. Then, based on the observation in Ref. [34], where strain rate is peaked at the boundary of DJR, Ref. [13] proposed a phenomenology based on the viscous force acting on the boundary of DJR. This viscous force model yields $\alpha = 3/2$ and $\beta = -1/2$, which agrees well with the experimental results.

Another interesting aspect of the transient response of dense suspensions under impact is the emergence of elasticity. Experiments have observed a much stronger response than that observed in suspensions undergoing DST. For shallow suspensions, even fractures can be observed on the surface of the suspensions [95]. In a series of experiments using penetrating intruders [71, 2, 79], a huge increase of stress exerted on the intruder is observed once the intruder is close to the bottom boundary, indicating the existence of a system-spanning DJR. Alternatively, the elastic response of dense suspensions under impact can also be captured from the free-falling impactor experimental setup [26], where rebounds of the impactor are observed for impact in a shallow container. Indeed, no DJR-based model mentioned above can explain such an elastic response. Furthermore, the connection between the elastic rebound of an impactor and the relations among u_0, $F_{\max}$, and $t_{\max}$ also needs to be clarified.

As far as we know, the only attempt to simulate the transient dynamics of dense suspensions was done using fluid-based multiphase simulations that contain the solvent and granular phases [5], where such simulations can reproduce the transient dynamics in various setups. However, their fluid simulations require the usage of constitutive equations with a tremendous amount of fitting parameters and a fluid-based method cannot capture the particle dynamics. In contrast, the particle-based simulation that is often used for simulating dense suspensions under shear [101, 72] cannot be used for the impact problem since such simulations cannot handle the free-surface of the suspensions. In this thesis, we extend the coupled lattice Boltzmann [104, 58, 59] and discrete element method [22, 70] that has been used to simulate DST and shear jamming of dense suspensions [87] to include the free-surface of the suspensions [106, 64].

1.4 Scope of this thesis

The main goal of this thesis is to understand the transient dynamics of dense suspensions under impacts. The main part is divided into four parts. In Chapter 2, we describe the coupled lattice Boltzmann method and discrete element method for simulating dense suspensions, including its extension to include the free surface of the suspensions. In Chapter 3, which corresponds to the paper published in Ref. [88], we use the simulation scheme to simulate

the impact of a free-falling impactor into dense suspensions. Here we focus on the elastic rebound and investigate its parameter dependences. We also visualize several local quantities including the stress inside the suspensions after the impact. Interestingly, no high shear stress is observed after the impact, in contrast to what was observed in the DST. Finally, we analyze the topological structure of the contact network between suspended particles using persistent homology. In Chapter 4, which corresponds to the paper published in Ref. [89], we focus on the connection between elastic rebound and the power-law relationship among u_0, $F_{\max}$, and $t_{\max}$. We observe that such power laws are independent of the system size, while rebound strongly depends on the depth of the container. We propose a phenomenology called the floating + force chains model that contains both viscous and elastic contributions. The floating model which does not include any effect of force chains can recover both the power-law exponents and the crossover from the low to high u_0 regime. We also find that the elastic force from the percolating contact force network is necessary to recover rebound. In Chapter 5, which corresponds to Ref. [90], we investigate the effective viscosity and elasticity of the DJR by replacement of the fitting effective viscosity in the floating + force chains model with the evaluated values of effective viscosity and elasticity of the DJR. Then, we extend such a model to discuss the possibility to run on top of suspensions by simulating a hopper that consists of a foot, spring, and body part. In Chapter 6, we conclude our results and discuss the future prospects of this research. In Appendix A, we describe the persistent homology analysis used in Chapter 3. In Appendix B, we describe the dynamic Hertzian contact model to explain the motion of the impactor. In Appendix C, we present the complete analytical solution of the floating model. In Appendix D, we describe the details of the algorithm to determine the percolating force chains, which are used in Chapter 4. In Appendix E, we show the relationships among u_0, $F_{\max}$, and $t_{\max}$ depend on the volume fraction of the suspensions.

Chapter 2

Coupled DEM-LBM simulation for dense suspensions

2.1 Overview

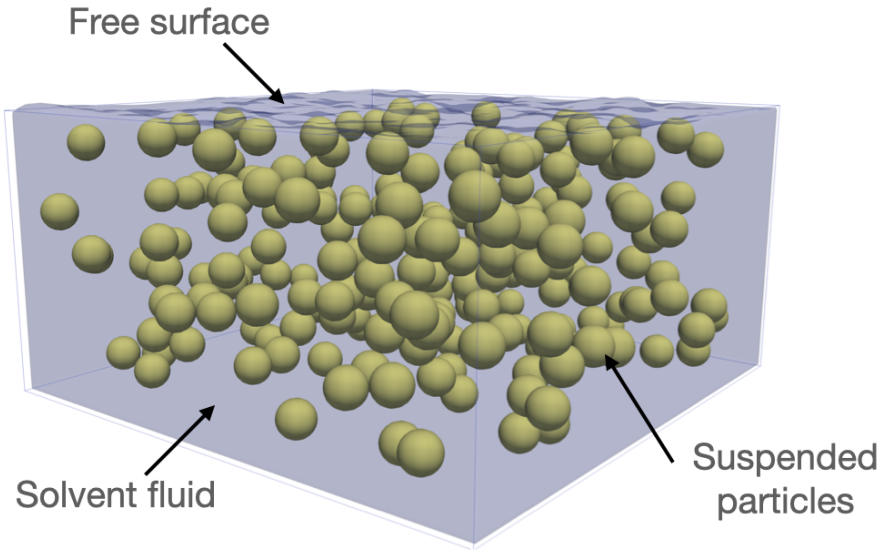

Fig. 2.1 An illustration of a suspension with free surface, yellow spheres are the suspended particles.

In this chapter, we explain the simulation method used in this thesis. The simulated system consists of suspended particles and a solvent fluid in a container box. To study the

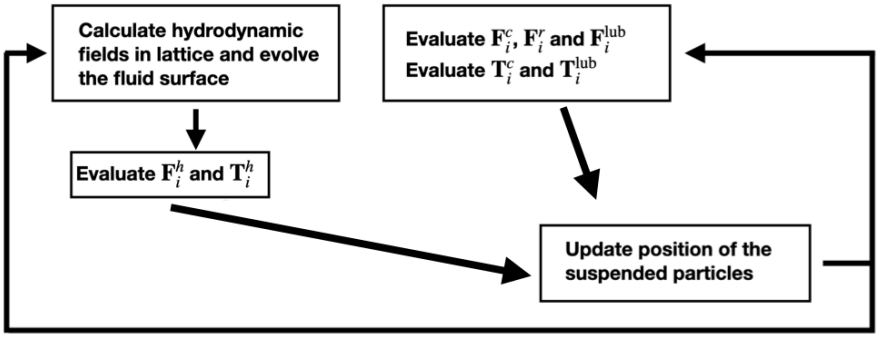

Fig. 2.2 Summary of the coupled LBM-DEM simulations [89].

impact problem in such suspensions, the free surface also needs to be taken into account. The schematic of the suspensions with a free surface can be seen in Fig. 2.1.

The suspended particles are assumed to be spherical particles which are, in general, not monodisperse in size distribution. Equations of motion including the torque balance of the particle i are given by

$$m_i \frac{d\boldsymbol{u}_i}{dt} = \boldsymbol{F}_i^c + \boldsymbol{F}_i^h + \boldsymbol{F}_i^{\mathrm{lub}} + \boldsymbol{F}_i^r + \boldsymbol{F}_i^g, \tag{2.1}$$

$$I_i \frac{d\boldsymbol{\omega}_i}{dt} = \boldsymbol{T}_i^c + \boldsymbol{T}_i^{\mathrm{lub}} + \boldsymbol{T}_i^h, \tag{2.2}$$

where $\boldsymbol{u}_i$, $\boldsymbol{\omega}_i$, m_i, and $I_i = (2/5)m_i a_i^2$ (with a_i the radius of $i-$th particle), are the translational velocity, angular velocity, mass, and the moment of inertia of particle i, respectively. $\boldsymbol{F}_i^g = -m_i g \hat{\boldsymbol{z}}$ is the gravitational force acting on the suspended particle i, where g is the gravitational acceleration and $\hat{\boldsymbol{z}}$ is the unit vector in the vertical direction. The summary of this method can be seen in Fig. 2.2. Our method accounts for both the short lubrication (force $\boldsymbol{F}_i^{\mathrm{lub}}$ and torque $\boldsymbol{T}_i^{\mathrm{lub}}$) in addition to the hydrodynamic force $\boldsymbol{F}_i^h$ and torque $\boldsymbol{T}_i^h$ from the lattice Boltzmann method (LBM)[81, 87], though some previous simulations contains only the short-range force for dense suspensions [101, 72]. In Section 2.2, we explain the LBM, treatment of hydrodynamic interactions, and the method to simulate the free surface of the suspensions. The contact forces $\boldsymbol{F}_{ij}^c$ and torques $\boldsymbol{T}_{ij}^c$ are computed using the linear-dashpot model with

Coulomb friction rules and friction coefficient μ [70]. We also introduce the electrostatic repulsive force $\boldsymbol{F}_{ij}^{r}$ arising from the double layer to prevent particles from clustering when we neglect the Brownian force [87, 72]. Details of such particle-particle interactions is written in Section 2.3.

2.2 Lattice Boltzmann method for dense suspensions

2.2.1 Hydrodynamic interactions

On molecular level, hydrodynamic interactions are the result of momentum transfer from a suspended particle to solvent molecules, and then from the solvent molecules to another suspended particle [21]. Nevertheless, since the length-scale and time-scale separations between suspended particles and solvent molecules are, at least, two orders of magnitude, the solvent is treated as a continuum fluid [10]. For suspensions, such dynamics can be described by the Stokes equations for the mass density ρ, and momentum density $\rho\boldsymbol{v}$

$$\nabla \cdot \boldsymbol{v} = 0, \tag{2.3}$$

$$\boldsymbol{\nabla} \cdot \overleftrightarrow{\sigma}^{v} = \nabla p + \eta_0 \nabla^2 \boldsymbol{v} = -\boldsymbol{f}, \tag{2.4}$$

where p is the pressure, $\overleftrightarrow{\sigma}^{v}$ is the viscous (deviatoric) stress tensor, $\boldsymbol{v}$ is the fluid velocity, $\boldsymbol{f}$ represents the body force, and η_0 is the solvent's shear viscosity. It is usually assumed that a stick boundary condition exists on the solid particle surfaces. In other words, the velocity of the fluid adjacent to the surface of particle i is equal to the local velocity of the surface at that point

$$\boldsymbol{v}(\boldsymbol{r}_s) = \boldsymbol{u}_i + \boldsymbol{\omega}_i \times (\boldsymbol{r}_s - \boldsymbol{R}_i), \tag{2.5}$$

for all points $\boldsymbol{r}_s$ on the surface S, where $\boldsymbol{R}_i$ and $\boldsymbol{u}_i$ is the position and velocity of the center of mass of the particle i and $\boldsymbol{\omega}_i$ is its angular velocity. The hydrodynamic force and torque are then obtained by integrating the stress over the particle surface

$$\begin{aligned} \boldsymbol{F}_i^h &= \oint_S \boldsymbol{t}(\boldsymbol{r}_s) dS \\ \boldsymbol{T}_i^h &= \oint_S \boldsymbol{r}_s \times \boldsymbol{t}(\boldsymbol{r}_s) dS, \end{aligned} \tag{2.6}$$

where $\boldsymbol{t} = p\boldsymbol{n} + \overleftrightarrow{\sigma}^{v} \cdot \boldsymbol{n}$ is the surface traction and $\boldsymbol{n}$ is the outward surface normal unit vector.

2.2.2 Lattice Boltzmann method

The hydrodynamic interactions (Eqs. (2.3) - (2.6)) are solved using the LBM. The LBM was introduced as an extension of the lattice gas automata and has been extensively used as a computational fluid dynamics solver [74, 104]. There are also several studies on suspensions using the LBM [94, 56, 60, 61], where this method has been confirmed to be efficient and accurate for sedimentation simulations [82]. Since the hydrodynamic fields are explicitly calculated in the LBM, one can simulate the flow of suspensions in various types of flows. Then, the free surface of the suspensions can also be incorporated. Such extension is not possible using the implicit or resistance matrix-based simulation for suspensions such as Stokesian dynamics [12] or LF-DEM [101, 72]. Indeed, such advantages of the LBM make it computationally expensive. However, the implementation of parallelized LBM is straightforward.

In the LBM, the hydrodynamic fields are calculated by computing the discrete distribution function on lattices. Due to such discrete nature of the LBM, one needs to discretize the unit of length into the lattice unit Δx and $\Delta c = \Delta x/\Delta t$.. We take the lattice unit Δx as $\Delta x = 0.2a_{\min}$, where $a_{\min}$ is the radius of the smallest particle. The hydrodynamic fields (mass density ρ_f and momentum density $\rho_f \boldsymbol{v}$) are calculated on the Eulerian node $\boldsymbol{r}$ inside cells of a fixed Cartesian grid as

$$\rho_f(\boldsymbol{r}) = \sum_{\boldsymbol{q}} f_{\boldsymbol{q}}(\boldsymbol{r}), \qquad \rho_f \boldsymbol{v}(\boldsymbol{r}) = \sum_{\boldsymbol{q}} f_{\boldsymbol{q}} \boldsymbol{c}_{\boldsymbol{q}}(\boldsymbol{r}), \tag{2.7}$$

where $\boldsymbol{c}_{\boldsymbol{q}}$ is the lattice velocity of the direction $\boldsymbol{q}$. All simulations in this thesis adopt nineteen directions (LBM community calls these lattices as D3Q19 lattices for 19 directions/quadratures in 3 dimensions) of $\boldsymbol{c}_{\boldsymbol{q}}$ [64, 94, 104, 106]. $f_{\boldsymbol{q}}(\boldsymbol{r})$ is the abbreviation of $f_{\boldsymbol{q}}(\boldsymbol{r},t)$ which is the discrete distribution function and has the dimension of mass density. The evolution equation of $f_{\boldsymbol{q}}(\boldsymbol{r},\boldsymbol{c}_{\boldsymbol{q}})$ is

$$f_{\boldsymbol{q}}(\boldsymbol{r}+\boldsymbol{c}_{\boldsymbol{q}}\Delta t, t+\Delta t) = f_{\boldsymbol{q}}(\boldsymbol{r},t) + \Delta t(\Omega_{\boldsymbol{q},c} + \Omega_{\boldsymbol{q},f}), \tag{2.8}$$

where $\Omega_{\boldsymbol{q},c}$ is the collision operator and $\Omega_{\boldsymbol{q},f}$ is an additional operator if a volumetric force density $\widetilde{\boldsymbol{f}}$ acts on the system. We use the Bhatnagar-Gross-Krook approximation for the collision operator [6], which relaxes the system to the equilibrium state $f_{\boldsymbol{q}}^{\mathrm{eq}}$ as

$$\Omega_{\boldsymbol{q},c} = \frac{f_{\boldsymbol{q}}^{\mathrm{eq}} - f_{\boldsymbol{q}}}{\tau_r}, \tag{2.9}$$

where τ_r is the relaxation time and is related to the kinematic viscosity ν as $\nu = \eta_0/\rho_f$, through the Chapman-Enskog expansion [19, 104] as

$$\tau_r = \Delta t/2 + \nu/c_s^2, \tag{2.10}$$

with c_s is the lattice sound speed, $c_s = \sqrt{\Delta c^2/3}$. The equilibrium distribution function $f_{\boldsymbol{q}}^{\mathrm{eq}} = f_{\boldsymbol{q}}^{\mathrm{eq}}(\rho_f, \boldsymbol{v})$ can be written as

$$f_{\boldsymbol{q}}^{\mathrm{eq}}(\rho_f, \boldsymbol{v}) = w_{\boldsymbol{q}}\rho_f\left[1 + \frac{\boldsymbol{c_q}\cdot\boldsymbol{v}}{c_s^2} + \frac{(\boldsymbol{vv} : (\boldsymbol{c_q c_q} - c_s^2\boldsymbol{I}))}{2c_s^4}\right], \tag{2.11}$$

where $w_{\boldsymbol{q}}$ is the lattice weight that depends on the configurations and : denotes the double inner product. The volumetric force density $\widetilde{\boldsymbol{f}}$ is incorporated through $\Omega_{\boldsymbol{q},f}$ as [33]

$$\Omega_{\boldsymbol{q},f} = w_{\boldsymbol{q}}\left(1 - \frac{\Delta t}{2\tau_r}\right)\left[\frac{(\boldsymbol{c_q} - \boldsymbol{v})}{c_s^2} + \frac{(\boldsymbol{c_q}\cdot\boldsymbol{v})}{c_s^4}\boldsymbol{c_q}\right]\cdot\widetilde{\boldsymbol{f}}. \tag{2.12}$$

As a result, the fluid velocity is changed so the momentum density introduced in Eq. (2.7) becomes

$$\rho_f \boldsymbol{v}(\boldsymbol{r}) = \sum_{\boldsymbol{q}}\left\{f_{\boldsymbol{q}}\boldsymbol{c_q}(\boldsymbol{r}) + \frac{\Delta t\widetilde{\boldsymbol{f}}(\boldsymbol{r})}{2}\right\}. \tag{2.13}$$

2.2.3 Mass-tracking algorithm for simulating free surface

To simulate the free surface, we need to implement the mass tracking algorithm [52, 106, 65]. First, we label each node as a fluid, gas, or interface node, where the interface node exists between the fluid and gas nodes as in Fig. 2.3. Note that Eqs. (2.7) and (2.8) are only used in the fluid and interface nodes.

A gas node represents the cell which is not occupied by the fluid, hence $f_{\boldsymbol{q}} = 0$. An interface node expresses the interface between fluid and gas, where the streaming and collision of $f_{\boldsymbol{q}}$ exist as in fluid nodes. Here, we introduce a variable m_f, which represents the density of the fluid in a single cell, to track the evolution of the surface. The interface node turns into a fluid node if $m_f \geq \rho_f^*$ or into a gas node if $m_f \leq 0$, where ρ_f^* is the unit density of the fluid. Therefore, the state of each node is characterized by the liquid fraction λ:

$$\begin{cases} \lambda = 1 & \text{if the node is liquid} \\ 0 < \lambda < 1 & \text{if the node is interface,} \\ \lambda = 0 & \text{if the node is gas,} \end{cases} \tag{2.14}$$

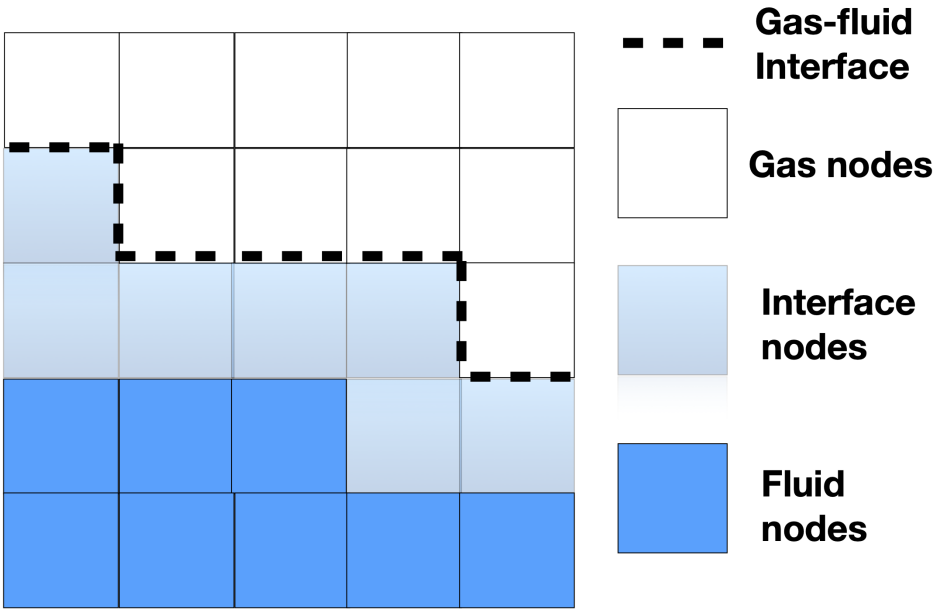

Fig. 2.3 An illustration of the division of the lattice nodes into fluid, interface, and gas nodes [88].

where $m_f = \lambda \rho_f$. The evolution of the m_f is determined by the balance between the populations streaming into the node $f_{\boldsymbol{q}'}(\boldsymbol{r}+\boldsymbol{c}_{\boldsymbol{q}'}\Delta t,t)$ ($\boldsymbol{q}' = -\boldsymbol{q}$) and out of the node $f_{\boldsymbol{q}}(\boldsymbol{r},t)$

$$m_f(t+\Delta t) = \sum_{\boldsymbol{q}} \alpha_{\boldsymbol{q}} (f_{\boldsymbol{q}'}(\boldsymbol{r}+\boldsymbol{c}_{\boldsymbol{q}'}\Delta t,t) - f_{\boldsymbol{q}}(\boldsymbol{r},t)) + m_f(t), \tag{2.15}$$

where $\alpha_{\boldsymbol{q}}$ is a function of λ of the neighboring node (located at $\boldsymbol{r}+\boldsymbol{c}_{\boldsymbol{q}'}\Delta t$).

$$\alpha_{\boldsymbol{q}} = \begin{cases} \frac{1}{2}[\lambda(\boldsymbol{r},t) + \lambda(\boldsymbol{r}+\boldsymbol{c}_{\boldsymbol{q}'}\Delta t,t)] & \text{if } f_{\boldsymbol{q}'}(\boldsymbol{r}+\boldsymbol{c}_{\boldsymbol{q}'}\Delta t,t) \text{ streams from an interface node,} \\ 1 & \text{if } f_{\boldsymbol{q}'}(\boldsymbol{r}+\boldsymbol{c}_{\boldsymbol{q}'}\Delta t,t) \text{ streams from a fluid node,} \\ 0 & \text{if } f_{\boldsymbol{q}'}(\boldsymbol{r}+\boldsymbol{c}_{\boldsymbol{q}'}\Delta t,t) \text{ streams from a gas node.} \end{cases} \tag{2.16}$$

When an interface node turns into a fluid node, the neighboring gas nodes turn into interface nodes. When an interface node turns into a gas node, the neighboring fluid nodes turn into interface nodes. Although the density in a continuum model must be conserved, the discrete model contains a small loss or gain of m_f. The surplus (or shortfall) of m_f is then computed at every time step and is corrected to satisfy the conservation among all interface nodes.

As stated before, LBM equations are solved only in the liquid and interface nodes. This creates a problem in the implementation of the population streaming to the interface nodes from gas nodes, which is necessary for Eq. (2.8) is not well-defined. Assuming that the gas node is always in equlibrium and has the identical velocity to that of the interface node $\boldsymbol{v}^{\text{in}}$ and a constant atmospheric density $\rho_a < \rho_f$, the incoming distribution function (first term on the right hand side of Eq. (2.8)) is replaced by the equilibrium distribution function with $\boldsymbol{v}^{\text{in}}$ and ρ_a [63],

$$f_{\boldsymbol{q}}(\boldsymbol{r},t) \rightarrow f_{\boldsymbol{q}}^{\text{eq}}(\boldsymbol{v}^{\text{in}},\rho_a). \tag{2.17}$$

This is analogous to applying a fixed-pressure boundary condition at the interface and local symmetry conditions for the velocity.

2.2.4 Coupling with particles

2.2.4.1 Overview

In this section, we explain how to calculate the hydrodynamic force and torque on particle i i.e $\boldsymbol{F}_i^h$ and $\boldsymbol{T}_i^h$ including the lubrication terms $\boldsymbol{F}_i^{\text{lub}}$ and $\boldsymbol{T}_i^{\text{lub}}$ in Eqs. (2.1) and (2.2). We use two different approaches to calculate the hydrodynamic forces from the LBM. For suspended particles, we combine the LBM with the immersed boundary method. This approach has been proven to be stable and accurate [106, 65, 63]. However, the immersed boundary method requires all parts of the particle to be immersed in the fluid, and thus cannot be used for an impactor or an intruder that is initially outside the suspensions. Therefore, for the impactor, we use an alternative approach called the bounce-back method. The discrete nature of the LBM has the consequence that it cannot capture the hydrodynamic force at a small gap between particles. Such lubrication force is indeed important for dense suspensions, meaning other correction terms ($\boldsymbol{F}_i^{\text{lub}}$ and $\boldsymbol{T}_i^{\text{lub}}$) must be added. Details of such corrections and the comparison between our approach and the full solution of the two-body hydrodynamic interactions are also discussed in the section.

2.2.4.2 Immersed boundary method

The immersed boundary method is originally developed by Peskin in 1972 for the simulation of blood flow and cardiac mechanics coupling [85]. In immersed boundary method, the structure (particles) is represented on a Lagrangian coordinate $\boldsymbol{r}^L$ that moves freely without being constrained. The force exerted by the particle on the fluid is then treated as a source term in the momentum equation. This method has been widely used and combined with

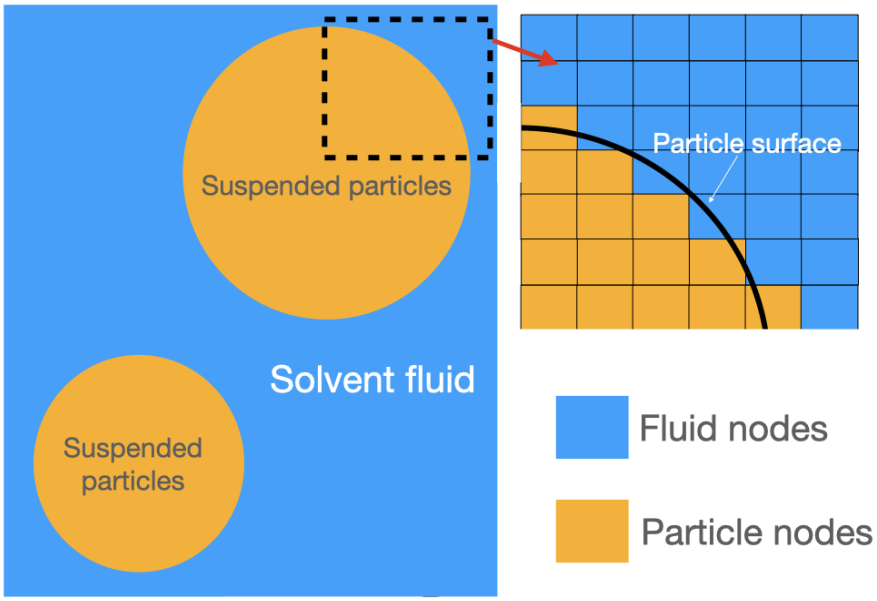

Fig. 2.4 The discretization of the spherical particles into particle nodes.

many computational fluid dynamics methods to simulate complicated structures immersed in fluid [76].

In this thesis, the Lagrangian coordinates represent the particles corresponding to the lattice nodes of the LBM, thus $\boldsymbol{r}^L = \boldsymbol{r}$ [65, 63] (See Fig. 2.4). Then, the hydrodynamic force on each particle node $\widetilde{\boldsymbol{F}}^h(\boldsymbol{r})$ can be computed directly from the differences between fluid and particle velocities

$$\widetilde{\boldsymbol{F}}^h(\boldsymbol{r}) = \frac{\Delta x^3}{\Delta t}\rho_f(\boldsymbol{r})[\boldsymbol{v}(\boldsymbol{r}) - \boldsymbol{u}_{\text{cell}}(\boldsymbol{r})], \tag{2.18}$$

where $\boldsymbol{u}_{\text{cell}}$ is the velocity of the particle node and it is calculate in the similar manner as Eq. (2.5),

$$\boldsymbol{u}_{\text{cell}}(\boldsymbol{r}) = \boldsymbol{u}_i + \boldsymbol{\omega}_i \times (\boldsymbol{r} - \boldsymbol{R}_i). \tag{2.19}$$

The resultant hydrodynamic force on suspended particle i, $\boldsymbol{F}_i^h$ is the sum of all forces on the nodes inside the particle l as

$$\boldsymbol{F}_i^h = \sum_{\boldsymbol{r}\in l} \widetilde{\boldsymbol{F}}^h(\boldsymbol{r}). \tag{2.20}$$

Similarly, the hydrodynamic torque is given by

$$\boldsymbol{T}_i^h = \sum_{\boldsymbol{r}\in l} (\boldsymbol{r} - \boldsymbol{R}_i) \times \widetilde{\boldsymbol{F}}^h(\boldsymbol{r}). \tag{2.21}$$

Thus, if suspended particles exist, the body force density of the fluid ($\widetilde{\boldsymbol{f}}$ in Eqs. (2.13) and (2.12)) becomes

$$\widetilde{\boldsymbol{f}}(\boldsymbol{r}) = -\rho_f g\hat{\boldsymbol{z}} - \frac{\widetilde{\boldsymbol{F}}^h(\boldsymbol{r})}{\Delta x^3}. \tag{2.22}$$

The first term on the right-hand side of Eq. (2.22) expresses the gravity force. Note that this scheme requires the whole particle to be inside the solvent fluid.

2.2.4.3 Bounce-back method

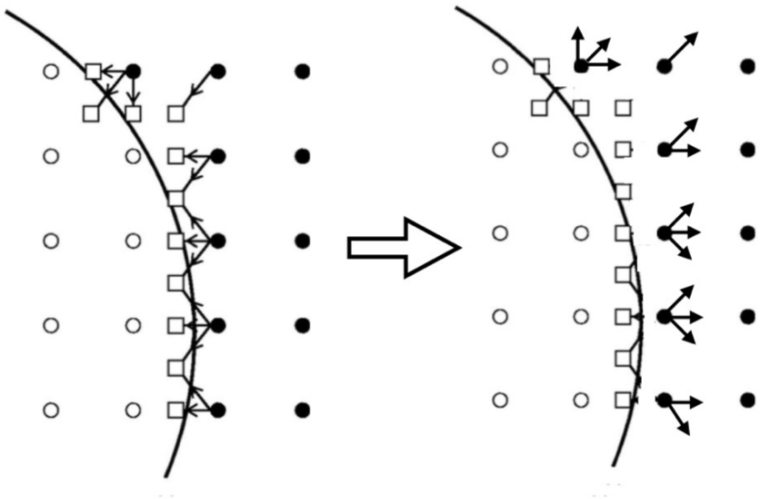

Fig. 2.5 An illustration of the bounce-rule in LBM simulation [89]. Filled circles represent fluid nodes, open circles represent solid nodes, open squares represent boundary nodes, and arrows represent the streaming discrete distribution functions.

We use the bounce-back rules for no-slip boundary conditions on walls and the surface of the impactor. At every time step, the nodes on container walls and the surface of the impactor are treated as boundary nodes *bn*. The bounce-back rule simply states that whenever discrete distribution function $f_{\boldsymbol{q}}$ is streaming towards the boundary, this distribution function is reflected and bounced back in the opposite direction $\boldsymbol{q}'$ (See Fig. 2.5). Then, this rule can be expressed as

$$f_{\boldsymbol{q}'}(\boldsymbol{r}, t+\Delta t) = f_{\boldsymbol{q}}(\boldsymbol{r}, t). \tag{2.23}$$

If the wall is moving, the reflection has to take into account the momentum transfer by an addititonal term [58, 59]

$$f_{\boldsymbol{q}}(\boldsymbol{r},t) - f_{\boldsymbol{q}'}(\boldsymbol{r},t+\Delta t) = \left(\frac{2w_{\boldsymbol{q}}\rho_f \boldsymbol{u}_{bn}\cdot\boldsymbol{c}_{\boldsymbol{q}}}{c_s^2}\right), \tag{2.24}$$

where $\boldsymbol{u}_{bn}$ is the velocity of the boundary nodes. Here, $\boldsymbol{u}_{bn}$ is calculated as

$$\boldsymbol{u}_{bn}(\boldsymbol{r}) = \boldsymbol{u}^I + (\boldsymbol{r}-\boldsymbol{R}^I)\times\boldsymbol{\omega}^I, \tag{2.25}$$

where $\boldsymbol{u}^I$ and $\boldsymbol{\omega}^I$ are the translational velocity and the angular velocity of the impactor, respectively. $\boldsymbol{R}^I$ denotes the center of mass of the impactor. The momentum exchange described in Eq. (2.24) results in a force on each node on the impactor surface $\widetilde{\boldsymbol{F}}^{bn}(\boldsymbol{r})$ as

$$\widetilde{\boldsymbol{F}}^{bn}(\boldsymbol{r}) = \frac{\Delta x^3}{\Delta t}\left(2f_{\boldsymbol{q}}(\boldsymbol{r},t) - \frac{2w_{\boldsymbol{q}}\rho_f \boldsymbol{u}_{bn}\cdot\boldsymbol{c}_{\boldsymbol{q}}}{c_s^2}\right)\boldsymbol{c}_{\boldsymbol{q}}. \tag{2.26}$$

The hydrodynamic force on the impactor $\boldsymbol{F}_I^h$ is the sum of the forces for all boundary nodes in the surface as

$$\boldsymbol{F}^{I,h} = \sum_{\boldsymbol{r}\in bn}\widetilde{\boldsymbol{F}}^{bn}(\boldsymbol{r}). \tag{2.27}$$

Similarly, the hydrodynamic torque on the impactor can be expressed as

$$\boldsymbol{T}^{I,h} = \sum_{\boldsymbol{r}\in bn}(\boldsymbol{r}-\boldsymbol{R}^I)\times\widetilde{\boldsymbol{F}}^{bn}(\boldsymbol{r}). \tag{2.28}$$

2.2.4.4 Lubrication corrections

This thesis mainly deals with suspensions on high volume fractions. For dense suspensions, the lubrication interaction between particles at a small inter-particle gap becomes highly important. As is shown in Fig. 2.4, the surface of the spherical particles in the LBM is not smooth, and its smoothness depends on the lattice size Δx. Indeed, the accuracy of the hydrodynamic interactions that can be captured through the LBM also depends on Δx. So the hydrodynamic interactions that arise from a small gap ($h_{ij} \ll \Delta x$) between suspended particles cannot be captured correctly. Therefore, we need to incorporate the lubrication correction when the gap between particles is small. This correction is calculated by the

grand-resistance matrix formulation of pairwise lubrication interaction [81]

$$\begin{pmatrix} \boldsymbol{F}_i^{\text{lub}} \\ \boldsymbol{F}_j^{\text{lub}} \\ \boldsymbol{T}_i^{\text{lub}} \\ \boldsymbol{T}_j^{\text{lub}} \\ \overleftrightarrow{\sigma}_i^{\text{lub}} \\ \overleftrightarrow{\sigma}_j^{\text{lub}} \end{pmatrix} = - \begin{pmatrix} \overleftrightarrow{A}_{ii} & \overleftrightarrow{A}_{ij} & \overleftrightarrow{B}_{ii} & \overleftrightarrow{B}_{ij} \\ \overleftrightarrow{A}_{ji} & \overleftrightarrow{A}_{jj} & -\overleftrightarrow{B}_{ji} & -\overleftrightarrow{B}_{jj} \\ \overleftrightarrow{B}_{ii} & \overleftrightarrow{B}_{ij} & \overleftrightarrow{C}_{ii} & \overleftrightarrow{C}_{ij} \\ -\overleftrightarrow{B}_{ji} & -\overleftrightarrow{B}_{jj} & \overleftrightarrow{C}_{ji} & \overleftrightarrow{C}_{jj} \\ \overleftrightarrow{G}_{ii} & \overleftrightarrow{G}_{ij} & \overleftrightarrow{H}_{ii} & \overleftrightarrow{H}_{ij} \\ -\overleftrightarrow{G}_{ji} & -\overleftrightarrow{G}_{jj} & \overleftrightarrow{H}_{ji} & \overleftrightarrow{H}_{jj} \end{pmatrix} \begin{pmatrix} \boldsymbol{U}_{ij} \\ \boldsymbol{U}_{ji} \\ \boldsymbol{\Omega}_i \\ \boldsymbol{\Omega}_j \end{pmatrix} \tag{26}$$

where $\boldsymbol{F}_i^{\text{lub}}$ is the lubrication force on particle i. While for particle j, $\boldsymbol{F}_j^{\text{lub}} = -\boldsymbol{F}_i^{\text{lub}}$. $\boldsymbol{U}_{ij} = \boldsymbol{U}_i - \boldsymbol{U}_j$ is the relative velocity. Here, we adopt the notation in Ref. [48, 46] such as $\overleftrightarrow{A}_{ij} = (A_{\alpha\beta}^{(ij)})$. Due to the Lorentz reciprocal theorem, one has got the symmetry relations such as

$$A_{\alpha\beta}^{(ij)} = A_{\beta\alpha}^{(ji)}. \tag{2.29}$$

For axisymmetric geometries, the coefficients can be expressed in terms of scalar functions as

$$A_{\alpha\beta}^{(ij)} = X_{ij}^A n_\alpha^{(ij)} n_\beta^{(ij)} + Y_{ij}^A (\delta_{\alpha\beta} - n_\alpha^{(ij)} n_\beta^{(ij)}), \tag{2.30}$$

$$B_{\alpha\beta}^{(ij)} = Y_{ij}^B \varepsilon_{\alpha\beta\gamma} n_\gamma^{(ij)}, \tag{2.31}$$

$$C_{\alpha\beta}^{(ij)} = X_{ij}^C n_\alpha^{(ij)} n_\beta^{(ij)} + Y_{ij}^C (\delta_{\alpha\beta} - n_\alpha^{(ij)} n_\beta^{(ij)}), \tag{2.32}$$

$$\begin{aligned} G_{\alpha\beta\gamma}^{(ij)} = {} & X_{ij}^G (n_\alpha^{(ij)} n_\beta^{(ij)} - \frac{1}{3}\delta_{\alpha\beta}) n_\gamma^{(ij)} \\ & + Y_{ij}^G (n_\alpha^{(ij)} \delta_{\beta\gamma} + n_\beta^{(ij)} \delta_{\alpha\gamma} - 2 n_\alpha^{(ij)} n_\beta^{(ij)} n_\gamma^{(ij)}), \end{aligned} \tag{2.33}$$

$$H_{\alpha\beta\gamma}^{(ij)} = Y_{ij}^H (\varepsilon_{\alpha\gamma\kappa} n_\alpha^{(ij)} n_\beta^{(ij)} \varepsilon_{\beta\gamma\kappa} n_\kappa^{(ij)} n_\alpha^{(ij)}), \tag{2.34}$$

where $n_\alpha^{(ij)}$ is the normal unit vector between particles i and j in the α direction and $\varepsilon_{\alpha\gamma\kappa}$ is the Levi-Civita symbol. The scalar functions X and Y are functions of interparticle gap h_{ij}. For two spheres of arbitrary size with the leading order only, the scalar functions are written

as

$$X_{ij}^{A} = 6\pi a_i \left[\frac{2\beta^2}{(1+\beta)^3} \frac{1}{h_{ij}+\delta} \right], \tag{2.35}$$

$$X_{ij}^{G} = 4\pi a_i^2 \left[\frac{3\beta^2}{(1+\beta)^3} \frac{1}{h_{ij}+\delta} \right], \tag{2.36}$$

$$Y_{ij}^{A} = 6\pi a_i \left[\frac{4\beta(2+\beta+2\beta^2)}{15(1+\beta)^3} \ln \frac{1}{h_{ij}+\delta} \right], \tag{2.37}$$

$$Y_{ij}^{B} = 4\pi a_i^2 \left[\frac{\beta(4+\beta)}{5(1+\beta)^2} \ln \frac{1}{h_{ij}+\delta} \right], \tag{2.38}$$

$$Y_{ij}^{G} = 4\pi a_i^2 \left[\frac{\beta(4-\beta+7\beta^2)}{10(1+\beta)^3} \ln \frac{1}{h_{ij}+\delta} \right], \tag{2.39}$$

$$Y_{ij}^{C} = 8\pi a_i^3 \left[\frac{\beta^2}{10(1+\beta)} \ln \frac{1}{h_{ij}+\delta} \right], \tag{2.40}$$

$$Y_{ij}^{H} = 8\pi a_i^3 \left[\frac{\beta^2(1+7\beta)}{20(1+\beta)^2} \ln \frac{1}{h_{ij}+\delta} \right], \tag{2.41}$$

where β is the ratio of the particles' radius defined as $\beta = a_i/a_j$ and δ is the roughness length playing the role of the cutoff length for the lubrication force [101, 72, 87]. Note that perfect spherical hard particles in the Stokes flow do not allow any contact between particles since the lubrication force diverges if the gap between particles reaches zero [48, 46, 45, 41]. All simulations in this thesis adopt $\delta/a_{\min} = 1 \times 10^{-2}$.

It is noteworthy that the resistance matrix in Eq. (26) slightly differs from the full two-body resistance matrix of hydrodynamic interactions [46, 45, 41], where the full solutions contain some terms from the background flow that depends on the rate of strain of the imposed flow tensor $\overleftrightarrow{E}^{\infty}$. As a benchmark, we validate our simulation by simulating two particles under simple shear i. e. $E^{\infty}_{\alpha\beta} = \dot{\gamma}\delta_{\alpha x}\delta_{\beta y}$ (see Fig. 2.6(a)). We then compare the simulation results with the exact solution of two body hydrodynamic interactions [46, 45, 41]. As one can see in Fig. 2.6(b), the LBM with lubrication corrections (Eq. (26)) is sufficient to recover the exact solution for two-body problem, while the deviation becomes larger if we include the $\overleftrightarrow{E}^{\infty}$ terms in the lubrication correction [91].

2.3 Discrete Element Method and Electrostatic interactions

We adopt the linear spring dashpot model for the contact between particles, which involves both the normal and the tangential parts of the contact force [70]. Note that we omit

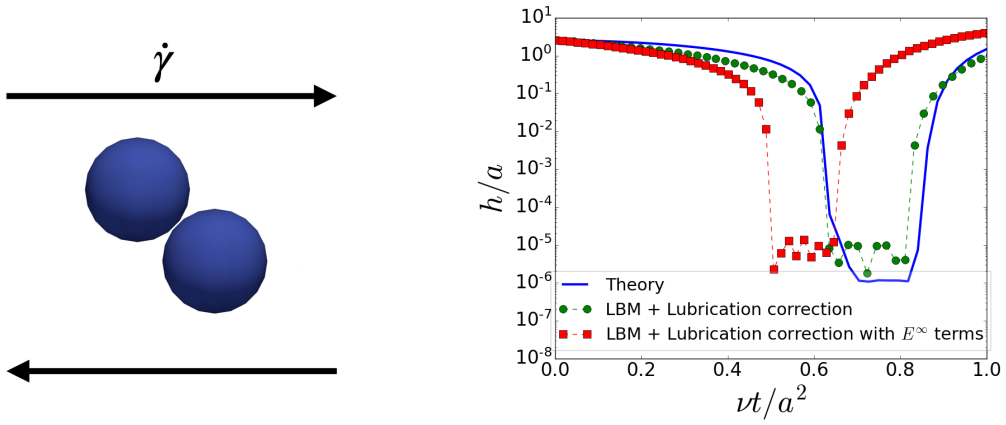

(a) (b)

Fig. 2.6 (a) Two particles under simple shear with shear rate $\dot{\gamma}$. (b) Plots of the time evolution of the interparticle gap h between two particles under simple shear, where green filled circles and red squares express the results by the LBM with lubrication correction in Eq. (26), and the LBM with lubrication correction including E^∞ terms, respectively [91]. The blue solid line is the exact solution of two spheres under the simple shear from Refs.[46, 45, 41].

the dissipative part for the tangential contact force as in Refs. [101, 72] for numerical stability. For the particle i, the contact force $\boldsymbol{F}_i^c$ and torque $\boldsymbol{T}_i^c$ are, respectively, written as $\boldsymbol{F}_i^c = \sum_{i\neq j}(\boldsymbol{F}_{ij}^{\rm nor} + \boldsymbol{F}_{ij}^{\rm tan})$ and $\boldsymbol{T}_i^c = \sum_{i\neq j} a_i \boldsymbol{n}_{ij} \times \boldsymbol{F}_{ij}^{\rm tan}$, where a_i is the radius of particle i. The normal force is explicitly expressed as

$$\boldsymbol{F}_{ij}^{\rm nor} = (k_n \delta_{ij}^n - \zeta^{(n)} u_{ij}^{(n)}) \boldsymbol{n}_{ij}, \tag{2.42}$$

where k_n is the spring constant, δ_{ij}^n is the normal overlap, $\boldsymbol{n}_{ij}$ is the normal unit vector between particles, $u_{ij}^{(n)}$ is the normal velocity difference of the contact point $u_{ij}^{(n)} = u_i^{(n)} - u_j^{(n)}$, and $\zeta^{(n)} = \sqrt{m_0 k_n}$ is the damping constant, where m_0 is the average mass of the suspended particles. If the tangential contact force is smaller than the slip criterion, tangential contact force is represented as

$$\widetilde{\boldsymbol{F}}_{ij}^{\rm tan} = k_t \delta_{ij}^t \boldsymbol{t}_{ij}, \tag{2.43}$$

where k_t, assumed to be $0.2k_n$, is the tangential spring constant, δ_{ij}^t is the tangential compression and $\boldsymbol{t}_{ij}$ is the tangential unit vector at the contact point between particles i and j. We adopt the Coulomb friction rules as

$$|\boldsymbol{F}_{ij}^{\rm tan}| = \mu |\boldsymbol{F}_{ij}^{\rm nor}| \quad \text{if } |\widetilde{\boldsymbol{F}}_{ij}^{\rm tan}| \geq \mu |\boldsymbol{F}_{ij}^{\rm nor}| \quad \text{(slip)}, \tag{2.44}$$

$$|\boldsymbol{F}_{ij}^{\rm tan}| = |\widetilde{\boldsymbol{F}}_{ij}^{\rm tan}| \quad \text{if } |\widetilde{\boldsymbol{F}}_{ij}^{\rm tan}| \leq \mu |\boldsymbol{F}_{ij}^{\rm nor}| \quad \text{(stick)}, \tag{2.45}$$

whereas δ_{ij}^t is updated each time with relative tangential velocity [70].

We also adopt electrostatic repulsive force $\boldsymbol{F}_i^r$ between suspended particles. Such electrostatic forces are also expressed by pairwise interactions as $\boldsymbol{F}_i^{\mathrm{r}} = \sum_{j \neq i} \boldsymbol{F}_{ij}^r$. The explicit expression of $\boldsymbol{F}_{ij}^r$ is expressed by the Derjaguin-Landau-Verwey-Overbeek (DLVO) theory[25, 112, 44] for the double layer electostatic force as

$$\boldsymbol{F}_{ij}^r = F_0 \exp(-h/\lambda)\boldsymbol{n}_{ij}, \tag{2.46}$$

where $F_0 = k_B T \lambda_B \hat{Z}^2 (e^{a_{\min}/\lambda}/(1 + a_{\min}/\lambda))^2/h^2$ with the charge number $\hat{Z}$, the Bjerrum length λ_B and the Debye-Hückel length λ. Here, we adopt the Debye-Hückel length $\lambda = 0.02 a_{\min}$. Our simulation ignores the Brownian force. Thus, the electrostatic repulsion force is important to prevent the suspended particles from clustering [87, 72].

Chapter 3

The impact-induced hardening in dense suspensions

3.1 Introduction

Under an impact, the suspension becomes rigid-like so that the impactor rebounds [26]. Some people use the discontinuous shear thickening (DST) to explain such impact-induced hardening [62, 2, 79], while the connection between these two processes is unclear [16]. Actually, there are some differences between these two processes. First, DST is observed in the dense suspensions undergoing steady shear, while the impact-induced hardening is a transient process undergoing normal compression. Second, the flow field of dense suspensions under impact is inhomogeneous [34]. This is contrary to the common DST which is anisotropic but still homogeneous [87]. Therefore, to make a further distinction between the impact-induced hardening and the DST, we need a detailed study of impact-induced hardening. Some papers also suggested some similarities between the shear jamming and the impact-induced hardening [34, 86], but the connection between the two processes is also unclear.

Previous experiments have already visualized the displacement and flow fields [114, 34], and measured the stress exerted on the impactor [71], but any experimental measurement of the shear and normal stresses fields of dense suspensions under impact has not been reported yet. On the other hand, the local distribution of the stress can be calculated and visualized through particle-based suspensions simulations [101, 72, 87]. Moreover, numerical simulation is an important tool to understand the microscopic mechanism behind several phenomena in suspensions since the forces acting on the suspended particles is not visible in three-dimensional experiments, unlike in 2-dimensional dry granular materials where the

force acting on each grain can be visualized with the photoelastic disks [20]. However, a particle-based simulation of a free-falling impactor hitting a suspension has not been reported so far because of the difficulty of simulating suspension with a free surface. As far as we know, the first fluid-based simulation of suspensions under impact has been conducted recently in Ref. [5], where the authors successfully reproduced various transient processes in dense suspensions. Since, however, their fluid simulations with a constitutive equation with some fitting parameters cannot capture the particle dynamics, the mechanism behind impact-induced hardening on the microscopic level remains elusive. In this chapter, we use the simulation method explained in the previous chapter to simulate the impact of a free-falling impactor into dense suspensions.

This chapter corresponds to Ref. [88], though some parts of it have been omitted and written in the Appendix for clarity. The outline of this chapter is as follows. The simulation setup for this chapter is explained in Sec. 3.2. In Sec. 3.3, we focus on the rebound motion of the impactor and investigate its parameter dependencies, namely the volume fraction of the suspensions, impact velocity, and the frictional interactions between suspended particles. Then, to get a better understanding of the mechanism behind the impact-induced hardening, we also visualize several local quantities inside the suspensions after the impact in Sec. 3.4. We analyze the topological structure of the contact network between suspended particles using persistent homology in Sec. 3.5. Finally, we summarize this chapter in Sec. 3.6.

3.2 Simulation setup in this chapter

Let us explain the setup of the simulations used in this chapter. Suspended particles (with bidispersity ratio $a_{\max} = 1.2a_{\min}$, where the radii of the large and small particles are $a_{\max}$ and $a_{\min}$, respectively) are confined into a rectangular box ($W \times D \times H$) with smooth walls. Details of the particle simulations can be seen in Chapter 2. We use two system sizes: (i) system with $N = 2000$ particles for in-depth analysis of the rebound motion, including the visualization of the local quantities and force network analysis and (ii) system with $N = 1200$ particles for analyzing the parameter dependences and drawing the phase diagrams. We discuss the finite-size effects in our simulation in Sec. 3.3.3.

At each simulation, a spherical impactor is dropped to the suspensions. The force and torque acting on the impactor are, respectively, given by

$$\boldsymbol{F}^I = \boldsymbol{F}^{I,h} + \boldsymbol{F}^{I,\mathrm{lub}} + \boldsymbol{F}^{I,c} + \boldsymbol{F}^{I,g}, \tag{3.1}$$

$$\boldsymbol{T}^I = \boldsymbol{T}^{I,h} + \boldsymbol{T}^{I,c} + \boldsymbol{T}^{I,\mathrm{lub}}, \tag{3.2}$$

where $\boldsymbol{F}^{I,h}$ and $\boldsymbol{T}^{I,h}$ are the hydrodynamic force and torque from the LBM, $\boldsymbol{F}^{I,\mathrm{lub}}$ and $\boldsymbol{T}^{I,\mathrm{lub}}$ are the force and torque from the lubrication corrections, $\boldsymbol{F}^{I,c}$ and $\boldsymbol{T}^{I,c}$ are the contact force and torque, and $\boldsymbol{F}^{I,g} = -m_I g\hat{\boldsymbol{z}}$ is the gravitational force acting on the impactor with mass m_I. Details on how to calculate such forces can be seen in Chapter 2. The radius of the impactor a_I is chosen to be $a_I = 4.5a_{\min}$ for $N = 2000$ and $a_I = 3.75a_{\min}$ for $N = 1200$ so that the ratios $W/a_I = 8$, $D/a_I = 8$, and $H/a_I = 4$ are fixed. The impactor is released from various heights H_0 that corresponds to the impact velocity as $u_0 = \sqrt{2gH_0}$, which also specifies the units of time in our simulation $t_g = \sqrt{a_{\min}/2g}$, units of velocity $u^* = \sqrt{2ga_{\min}}$, units of force $F_0 = \frac{4}{3}\pi\rho_f a_{\min}^3 g$, and units of stress $\sigma_0 = F_0/a_{\min}^2$. The illustration of the free-falling impactor simulation can be seen in Figs. 3.1(a) and 3.1(b).

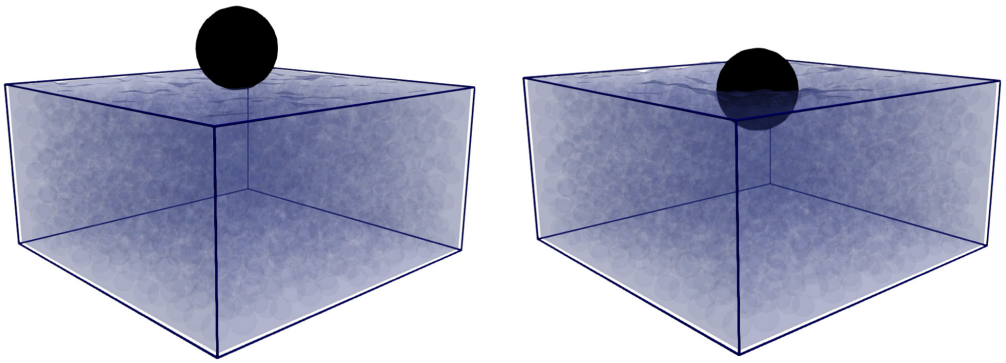

(a) (b)

Fig. 3.1 Snapshots of our simulation for $\phi = 0.54$, $\mu = 1$, and $u_0/u^* = 4.26$ at (a) $t/t_g = 0$. (b) $t/t_g = 0.1$.

3.3 Rebound motion of the impactor

3.3.1 Impactor motion and the force response

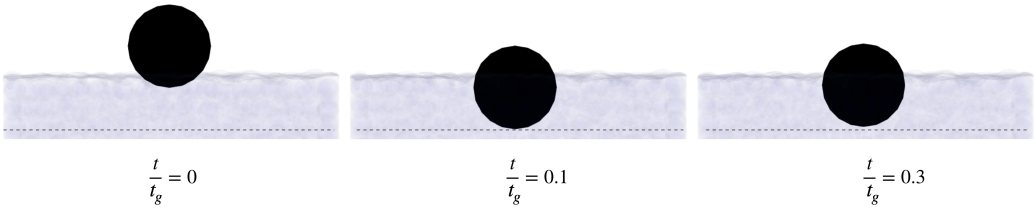

Fig. 3.2 Successive snapshots of the impactor in a quasi-two-dimensional slice of container, where the dashed lines mark the maximum penetration.

In this section, we discuss the motion of the impactor shortly after the impact. By looking at the successive motions of the impactor from Fig. 3.2, where we set time $t = 0$ and height $z = 0$ at the moment of impact, one can confirm that initially, the impactor penetrates and then slightly rebounds after reaching the maximum penetration. We plot the impactor speeds $u_z^I(t)/u^*$ against time for various volume fractions of suspended particles ϕ in Fig. 3.3(a). The vertical position of the impactor $z(t)/a_{\min}$ for various volume fractions ϕ can be seen in Fig. 3.3(b). Both results are obtained by using 2000 frictional particles with $\mu = 1.0$. One can observe the rebound of the impactor ($u_z^I(t)/u^* < 0$) for $\phi \geq 0.54$, which agrees semi-quantitatively with the free-falling impactor experiment [26]. This rebound is the instance of the impact-induced hardening of the suspension shortly after the impact. After the rebound, the suspension relaxes, and the impactor starts to sink. Note that ϕ for rebounds might be a little higher than that in the experiment [26].

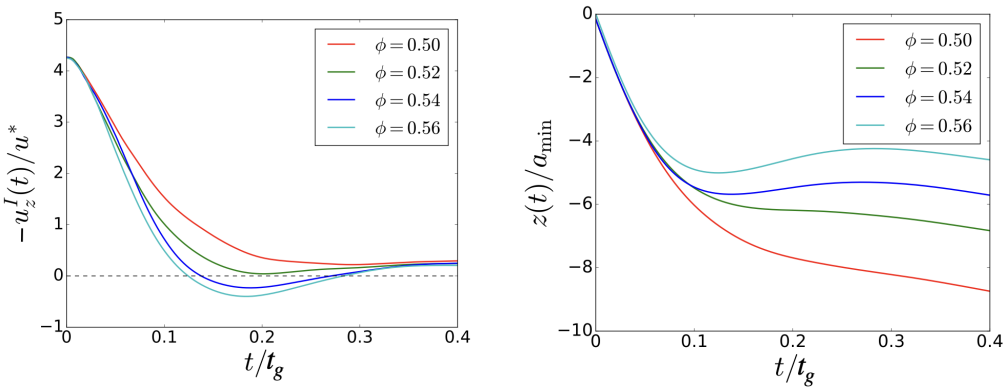

(a) (b)

Fig. 3.3 (a) Plots of impactor speeds in the z-direction, $u_z^I(t)/u^*$, against time for various volume fractions ϕ. (b) Plots of the heights of the impactor against time for various volume fractions ϕ. Both results are obtained by using 2000 frictional particles whose friction constant is $\mu = 1$.

In Fig. 3.4(a), we plot the time evolution of total forces exerted on the impactors for both rebound and no-rebound cases for $\mu = 1.0$ and $N = 2000$. One can see that the maximum exerted force for the rebound case is larger than that for the no-rebound case. We find that the peak of the contact force is located slightly after the peak of the total force, which follows the weaker peak from the hydrodynamic contribution. The time difference between these two peaks is not large so they merge into a single peak in the total force. In an experiment with a rod impactor, two peaks in the acceleration of the impactor are observed for deep suspensions while for shallower suspensions, in which rebound takes place, the separation between peaks is not detectable [114]. Thus, we confirm that the second peak in Ref. [114] originated from the contact between suspended particles. Moreover, they also observed the

second peak when the impact force is transmitted to the boundary. To clarify this, we plot the force exerted on the bottom wall in Fig. 3.4(b). Compared to the force exerted on the impactor, one can see a clearer distinction between the rebound and no-rebound cases, where the force exerted on the bottom wall in the rebound case is about three times larger than in the no-rebound case. This indicates that the rebound takes place when the contact force network percolates from the impactor to the boundaries, which is consistent with the picture in Ref. [71].

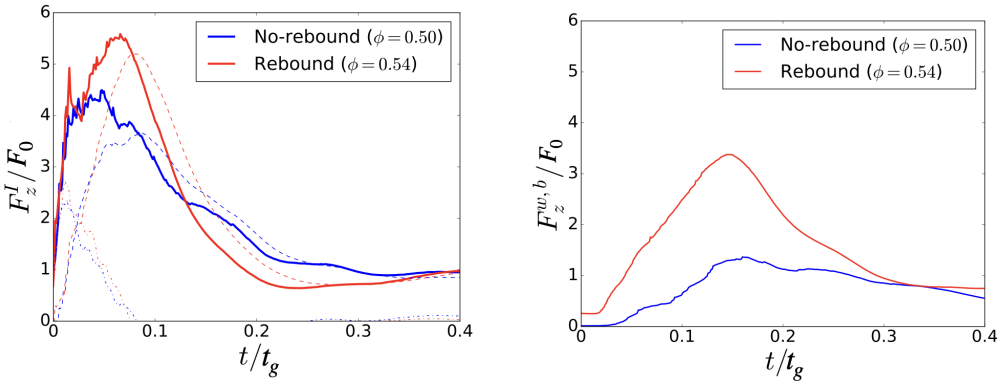

(a) (b)

Fig. 3.4 Plots of the force for both rebound ($\phi = 0.54$) and no-rebound ($\phi = 0.50$) cases with $N = 2000$. (a) Force exerted on the impactor, where the solid lines are the total force, dashed lines represent the contact contributions, dot-dashed lines represent the hydrodynamic contributions, and (b) the total force exerted on the bottom wall. All results are obtained for $\mu = 1$ and $u_0/u^* = 4.26$.

3.3.2 Parameter dependences of the rebound motion

Now let us discuss the parameters that determine the existence of the rebound motion of the impactor. First, we fixed the friction coefficient at $\mu = 1$ and vary the impact speed u_0 and volume fraction ϕ and check whether rebound takes place or not. Due to the limitation of our computational resources, the data for this phase diagram are obtained with $N = 1200$ particles. The phase diagram of the rebound process in the plane of control parameters u_0 and ϕ is plotted in Fig. 3.5(a). We observe that the impact-induced hardening depends both on the impact speed u_0 and the volume fraction ϕ, where one can see that the tendency for a rebound is higher at high u_0 and ϕ. Some papers reported that impact-induced hardening depends on impact speed [71, 5]. Note that the highest rebound volume fraction ($\phi = 0.56$) in our simulation is still below the frictional ($\mu = 1$) jamming fraction $\phi_j^{\mu=1} \approx 0.585$ [102]. Rebound takes place on $0.50 \leq \phi \leq 0.56$. This range is similar to the observed volume

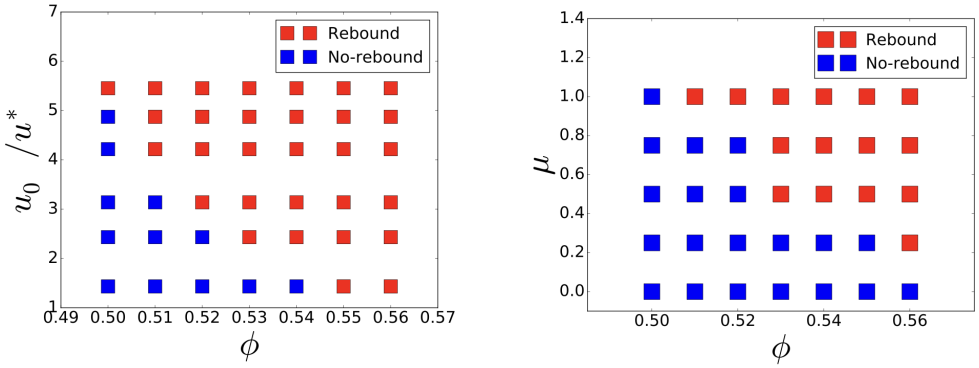

(a) (b)

Fig. 3.5 (a)Phase diagram showing whether the impactor rebounds before sinking as a function of the volume fraction ϕ and the impact speed u_0. (b) Phase diagram showing whether the impactor rebounds before sinking on a plane of volume fraction ϕ and friction coefficient μ.

fractions for the DST under simple shear in numerical simulations [101, 72, 87]. However, one should recognize that the two processes are different since impact-induced hardening is a heterogeneous and transient process, while shear thickening is a homogenous steady-state process.

We then clarify the roles of mutual friction between particles and plot the rebound phase diagram on a plane of the friction coefficient μ and volume fraction ϕ in Fig. 3.5(b). Due to the limitation of our computational resources, the data for this phase diagram are obtained by simulations of $N = 1200$ particles. One can verify that the impact-induced hardening is enhanced as μ increases, as the tendency to rebound is higher for high μ. This μ-dependence is analogous to that for DST in dense suspensions under steady shear [83, 101, 72, 110, 87] and for impact in dry granular materials [51].

To investigate how frictional interactions between suspended particles affect the dynamics of the impactor, we plot the time evolution of the forces exerted on the impactor for both the frictional and frictionless cases both for $\phi = 0.54$ in Fig. 3.6(a). Here, one can verify that the force in the frictional case persists longer than that in the frictionless case. To quantify such tendency, we plot the impulse J defined by $J = \int_{t=0}^{t=0.1} F_z^I(t)dt$ in Fig. 3.6(b). One can confirm that the impulse for the frictional case monotonically increases as the friction coefficient μ increases for all volume fractions ϕ. Here, one can see that friction between particles plays an important role in impact-induced hardening, where the role of the frictions is to stabilize the contact between suspended particles, which are essential for the strong hardening of the suspensions that leads to the rebound of the impactor.

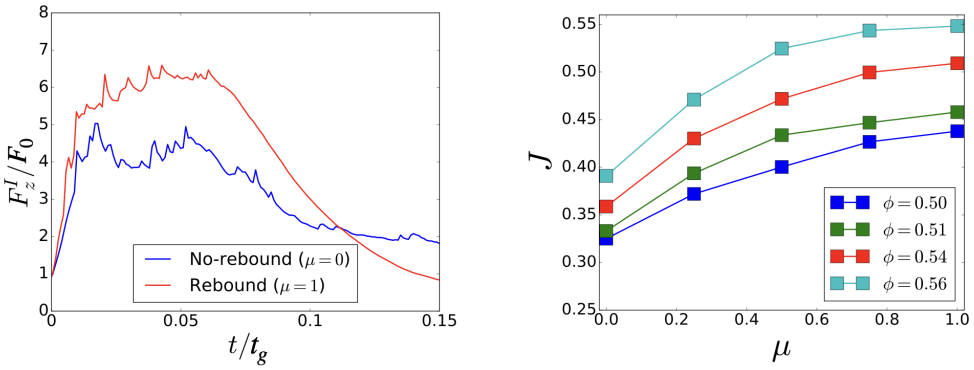

(a) (b)

Fig. 3.6 (a) Plots of the forces exerted on the impactors for $\phi = 0.54$, $u_0/u^* = 4.26$ for $\mu = 0$ (no-rebound) and $\mu = 1$ (rebound). (b) Impulses on the impactor J as functions of the friction coefficient μ for various ϕ.

3.3.3 Finite size effects

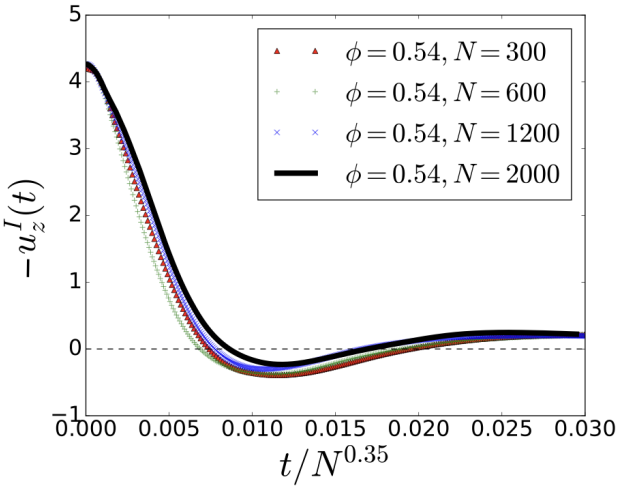

Fig. 3.7 Plots of impactor speeds in the z-direction, $u_z^I(t)/u^*$, against time for several numbers of particles N for $\phi = 0.54$. The time scale t is scaled by the particle numbers N^κ with $\kappa = 0.35$

In this subsection, we examine how the impactor motion depends on the number of particles in our system. We plot the time evolution of the impactor velocity for several numbers of particles N for $\phi = 0.54$ and $u_0/u^* = 4.26$ in Fig. 3.7. We keep the ratios of the impactor radius to the width and depth of the box as $W/a_I = 8$, $D/a_I = 8$, and $H/a_I = 4$. Therefore, varying the numbers of particles N also changes the ratio of impactor radius

a_I to the smallest suspended particles radius $a_{\min}$ as $a_I/a_{\min} = 2.25, 3, 3.75$, and 4.5 for $N = 300, 600, 1200$, and 2000, respectively.

We found that the system size mainly scales the time of the impact processes. Although the impactor velocity depends a little on the system size (and as a result, the phase diagrams also depend a little on the system size), such system size dependences are not significant. For instance, if we scale the time by N^{κ} with exponent $\kappa = 0.35$ for the data of $\phi = 0.54$, we can obtain an approximate universal curve of the impact speed. Thus, one can guess the behavior in the thermodynamic limit from the simulations with small systems. However, the value of κ might depend on ϕ thus a systematic study in finite-size scaling for simulations of dense suspensions under impact is necessary.

3.4 Inside the hardening suspensions

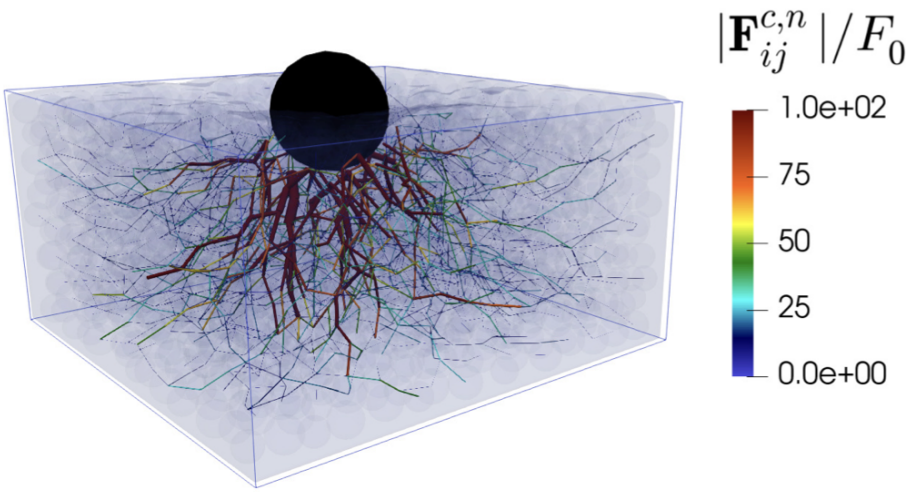

Fig. 3.8 Force chains of the normal contact forces scaled by the gravitational force $|\boldsymbol{F}_{ij}^{c,n}|/F_0$.

To understand the microscopic mechanism behind the impact-induced hardening, we visualize the suspension shortly after the impact. First, we visualize the force chains generated by the impactor by plotting the ratio of the normal contact force to the gravitational force $|\boldsymbol{F}_{ij}^{c,n}|/F_0$ in Fig. 3.8. One can observe the percolating force chains span from the impactor

to the boundary without any loops. This spanned region of force chains from the impactor to the boundaries can be regarded as the dynamically jammed region.

Let us proceed to visualize the quantities of the suspended particles. For this purpose, we slice the region in the middle of the simulation box as in Fig. 3.9(a). First, we compute the local volume fraction ϕ_i on each particle with the aid of radical Voronoi tesselation [92]. We use an open-source c++ library Voro++ to construct the radical Voronoi tesselation in our simulation domain [96]. Then, the local volume fraction ϕ_i is calculated as $\phi_i = v_i/V_i$, where $v_i = 4\pi a_i^3/3$ is the volume of particle i and V_i is the volume of its corresponding Voronoi cell. In Fig. 3.9(b), we visualize ϕ_i in the sliced region. One can observe that the local volume fraction is almost homogeneous and not largely affected by the impact. This corresponds to the experimental observation where no detectable increase of packing fraction in the suspension is observed when impact-induced hardening takes place [34].

We visualize the normal stress on each suspended particle σ_{zz}^i in the sliced region in Fig. 3.9(c). Here we observe a localized region with a distinctively high value of σ_{zz}^i corresponding to force chains in Fig. 3.8, which extends from the impactor to the boundary. In Fig. 3.9(d), we visualize each particle displacement in normal (z-) direction Δz^i, also sliced in the middle of the simulation box. One can observe the existence of a localized region of high normal displacements, which corresponds to the regions in Figs. 3.9(c) and 3.8. The visualization of Δz^i within our simulation reminisces the experimentally observed one in Refs. [114, 34]. The regions of large σ_{zz}^i (Fig. 3.9(c)), Δz^i (Fig. 3.9(d)), and the force chains (Fig. 3.8) correspond to the dynamically jammed region in Refs. [114, 34]. As indicated in Refs. [114, 34, 71, 5], the propagation speed of the jamming front depends on the impact speed. After the impactor stops, one can imagine that the vanishing of the stress exerted on the suspension by the impactor allows the suspension to relax and to become soft, which in turn the impactor subsequently sinks after the impact. On the other hand, we observe a uniformly weaker magnitude of the shear stress σ_{xz}^i compared to the normal stress σ_{zz}^i as we plot the ratio $\sigma_{xz}^i/\sigma_{zz}^i$ of each particle in the sliced region in Fig. 3.9(e). Thus, the local shear stress is unrelated to the dynamically jammed region. This observation distinguishes the impact-induced hardening and the DST.

3.5 Topology of the force network: Persistent homology analysis

In this section, we elaborate the role of the network formed by contacting particles (force) chains in impact-induced hardening. One can analyze the topological structure of force

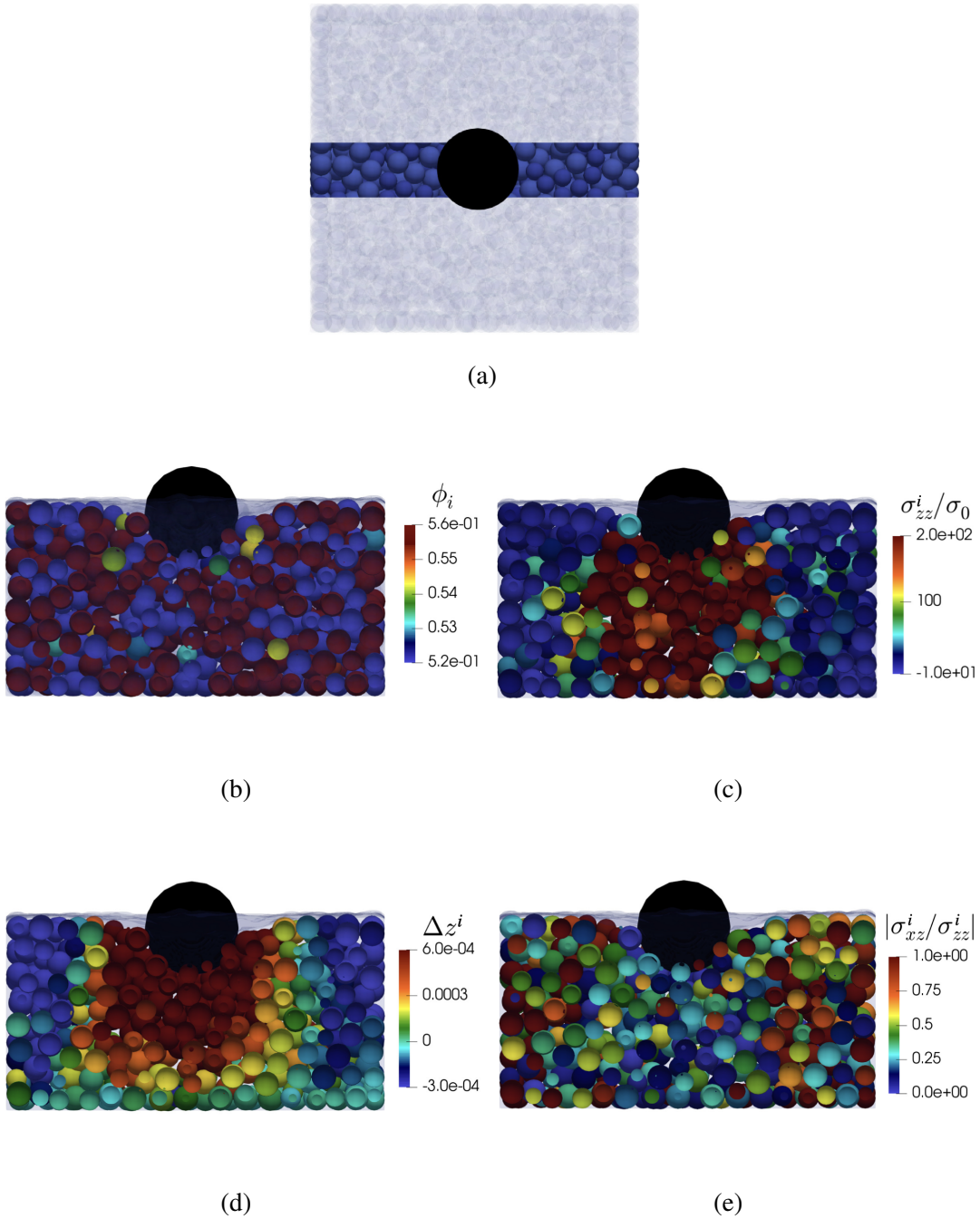

Fig. 3.9 Visualizations of local quantities for $\phi = 0.54$ and $u_0/u^* = 4.26$ shortly after the impact ($t/t_g = 0.1$): (a) A top view of the sliced region. (b) Local volume fraction ϕ_i. (c) Magnitude of the dimensionless normal stress σ^i_{zz}/σ_0. (d) Normal displacement Δz^i. (e) Absolute ratio between the shear and normal stress.

chains using persistent homology analysis [18]. In addition to successfully distinguishing the liquid, amorphous, and crystalline states of, e.g. silicon dioxide [39], persistent homology allows us to quantify the structure of the force chains in granular materials [53, 109] and in dense suspensions under simple shear [29].

Since no persistent loops or higher dimensional structures are observed in the force network in Fig. 3.8, the relevant topological structure is only the *connected component* represented by the zeroth Betti number β_0. One can perform persistent homology analysis for connected component by filtering the force chains by increasing threshold θ_f, where a link in a force chain appears when $|\boldsymbol{F}_{ij}^{c,n}|/F_0 \leq \theta_f$. We regard this as the birth of a connected component. As the threshold further increases, the structure grows in size as additional contacts are added. When connected components merge, the structure that is born later in the filtration (which has higher birth θ_f) dies. We record the birth θ_f as $\theta_{f,b}$ and the death θ_f as $\theta_{f,d}$. This rule ensures that $\theta_{f,d} \geq \theta_{f,b}$. The algorithm for filtering chains is available in public domains [75]. Note that in Refs. [53, 109, 29], $\theta_{f,b}$ is not always smaller than $\theta_{f,d}$, since they adopt filtration by reducing the threshold. We plot these quantities in the persistence diagram. Details on how to transform the force networks into a persistence diagram are written in Appendix A.

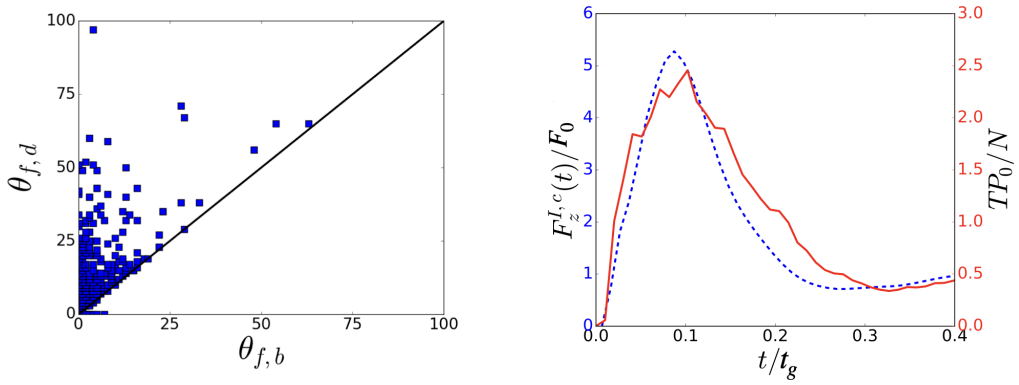

(a) (b)

Fig. 3.10 (a) Persistence diagram of the connected components of force network for $\phi = 0.54$, $u_0/u^* = 4.26$, and $\mu = 1$ shortly after the impact ($t/t_g = 0.1$). (b) Plots of the total persistence of the connected components TP_0, scaled by the number of suspended particles N, against time for $\phi = 0.54$ and $u_0/u^* = 4.26$ (red lines), and the corresponding contact force on the impactor in the $z-$direction $F_z^{I,c}$ (dashed blue lines).

We plot $\theta_{f,d}$ against $\theta_{f,b}$ for all connected components appearing in Fig. 3.8 in the persistence diagram (Fig. 3.10(a)). Shortly after the impact, we observe more points far from the diagonal, representing the connected components which persist through the increments of the force threshold with the life span $(\theta_{f,d} - \theta_{f,b})$. The mechanism for the occurrence of

a long lifespan for some connected components is by forming a long chain. Thus, persistent homology emphasizes the length of the chain instead of its magnitude. This argument shows that percolated force chains exist. One point to note is that a component with $\theta_{f,d} = -1$ has infinite persistence, i.e. it does not die until the filtration ends. The components with infinite persistence represent the contact forces links that do not form any connection with other links. Persistent homology ignores the effect of such contact forces since we are only interested in extracting the structural information.

The total persistence of the connected components TP_0 is the sum of all life spans in the persistence diagram

$$TP_0 = \sum_{(\theta_{f,d},\theta_{f,b})} (\theta_{f,d} - \theta_{f,b}). \tag{3.3}$$

This allows us to describe the persistence diagram by a single number. Higher TP_0 means more merging of force chains takes place, while $TP_0 = 0$ means that no connected components are merged. We plot TP_0 scaled by the number of suspended particles N against time in Fig. 3.10(b). It is remarkable that TP_0 reaches its peak at the same time as the corresponding contact force and that the shape of TP_0 is similar to that of the contact force. Thus, the peak of the contact force inducing the hardening of the suspension originates from the existence of long and sustained force chains. This can only take place when the force chains are percolated to the boundaries. Our results provide quantitative proof for the argument in Refs. [114, 71, 26] in which the impact-induced hardening takes place when the dynamically jammed region spans from the impactor to the boundary.

To conclude this section, let us re-state the implications of our persistent homology analysis. First, the magnitude of the force chains is not as important as its topological structure. Second, persistent homology provides quantitative proof that the dynamically jammed region that spans from the impactor to the boundary exists. Third, there are no persistent loops of force chains in our simulations. Meanwhile, loops are more significant for sheared suspensions where DST is observed since the total persistence of β_1 can capture the behavior of the viscosity [29]. This distinction exists because the force chains in sheared suspensions are more structured and uniformly distributed than that in suspensions undergoing impact. Thus, this gives us another distinction between the impact-induced hardening and the DST.

3.6 Summary of this chapter

We have simulated the impact-induced hardening of suspensions by the LBM simulation with a free surface, where the free-falling impactor rebounds for high impact speed with the suspension of high volume fraction involving frictional particles. By visualizing each

suspended particle, we observed the emergence of the dynamically jammed region with a distinctively huge value of particle normal stress σ^i_{zz}, formed by force chains of contacting particles. Meanwhile, the particle shear stress σ^i_{xz} of the suspension is not significantly affected by the impact. We also found that frictional interaction between suspended particles is necessary for the impact-induced hardening to maintain the dynamically jammed region. The fact that the jammed region is characterized by the normal stress instead of shear stress is important since it distinguishes the impact-induced hardening from shear-induced phenomena such as DST and shear jamming. Finally, with the aid of persistent homology, (i) we provided the quantitative proof of the existence of a system-spanning dynamically jammed region, and (ii) we found that only the topological structure of the force chains is important for the contact force acting on the impactor, and (iii) we did not observe any persistent loops formed by the force networks, which distinguish the impact-induced hardening and the DST.

Chapter 4

Viscoelastic response of the impact process in dense suspensions

4.1 Introduction

Previously in Chapter 3, we have discussed the elastic response of the suspensions, characterized by the rebound process of the free falling impactor. In this chapter, we discuss the relation between the impact speed u_0 and the maximum force acting on the impactor $F_{\max}$ or the elapsed time $t_{\max}$ to reach $F_{\max}$ in impact processes. Previous studies [114, 79, 13] showed the existence of power-law relations such as

$$F_{\max} \propto u_0^{\alpha}, \qquad t_{\max} \propto u_0^{\beta}. \tag{4.1}$$

It is noteworthy that similar relations are also found in impact processes for dry granular materials [55]. To explain the motion of the impactor after the impact, Ref. [114] proposed the added-mass model. The numerical solution of the added-mass model suggests $\alpha = 2$ and $\beta = -1$ [79], though the exponents in their experiment are $\alpha = 1.5$ and $\beta = -1/2$. Moreover, a closer look at the data in Ref. [114] suggested that u_0-independent exponents α and β are not appropriate to fit the data in all ranges of the impact speed since such power-law only exists at high impact speed. A recent experiment [13] also suggested $\alpha = 1.5$ and $\beta = -1/2$. These values of the exponents are obtained as the solution of the viscous force model [13], which is inspired by the existence of a growing dynamically jammed region below the impactor [114, 34]. Nevertheless, the viscous force model [13] has two defects in which (i) the model cannot explain the behavior for low u_0 regime observed in Ref. [114], and (ii) the model cannot explain the mechanism of the rebound process since any elastic term is absent. Therefore, the connection between the rebound of the impactor and

the relationships among u_0, $F_{\max}$, and $t_{\max}$ should be clarified to understand the viscoelastic response of an impactor on dense suspensions.

In this chapter, we try to clarify the connection between the relations among u_0, $F_{\max}$, and $t_{\max}$ and the rebound process. In addition, we propose a phenomenology to explain these processes, including the elastic force as a result of percolated force chains between the impactor and bottom plate to describe the rebound phenomenon. This model is essentially reduced to the viscous force model if percolated force chains are absent. This chapter corresponds to Ref. [89]. The structure of this chapter is as follows. In Sec. 4.2, we briefly describe the simulation setup and the parameter selections. In Sec. 4.3, we present the phenomenological floating + force chains model. In Sec. 4.4, the floating + force chains model is validated with the simulation results. In Sec. 4.5, we summarize the results of this chapter.

4.2 Simulation setup and parameter selections

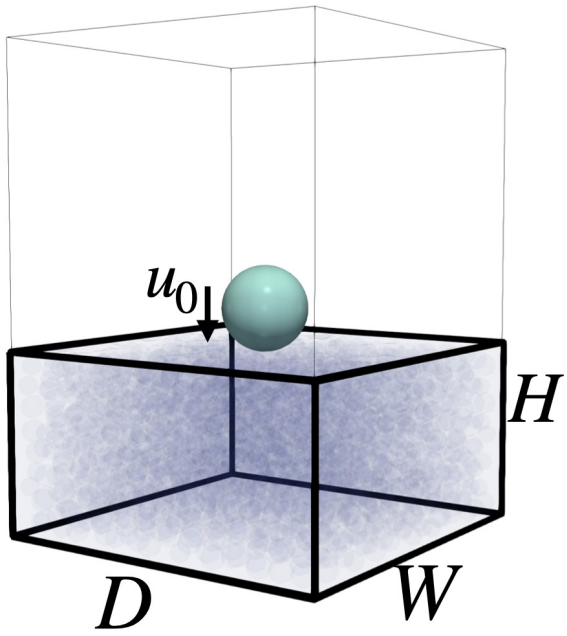

Fig. 4.1 An illustration of an initial setup of our simulation.

We simulate a binary mixture of suspension consisting of equal number of large and small particles with bidispersity ratio $a_{\max} = 1.2a_{\min}$, where the radii of the large and small particles are $a_{\max}$ and $a_{\min}$, respectively. We use such a mixture to avoid the crystallization of suspended particles. These suspended particles have the identical density ρ_p which is equal

to the density ρ_f of the solvent. The suspension is confined in a rectangular box surrounded by smooth sidewalls and a smooth bottom plate. Since we simulate the free falling processes of an impactor, there is no lid above the container. The volume V of the suspension at rest is expressed as $V = W \times D \times H$, where H is the depth of the suspension and $W = D$ is the width of the container as shown in Fig. 4.1. The volume fraction ϕ of the suspension at rest without the impactor is defined as $\phi = 2N\pi(a_{\max}^3 + a_{\min}^3)/3V$, where N is the number of suspended particles used in the simulation. The hydrodynamic interaction among particles is simulated using the LBM. The contact force between suspended particles is modeled by the DEM with spring constant k_n between contacting particles [70]. In this paper, we adopt the friction coefficient $\mu = 1$ for all cases. Details of our simulation method can be seen in Chapter 2.

A spherical impactor with diameter D_I and density ρ_I is released from the height H_0 which corresponds to the impact speed $u_0 = \sqrt{2gH_0}$ with the gravitational acceleration g. In our simulation ρ_I and D_I satisfy $\rho_I = 4\rho_f$ and $D_I = 6a_{\min}$, respectively. The mass of the impactor m_I is expressed as $m_I = \pi\rho_I D_I^3/6$. We also introduce the time scale $t_g = \sqrt{a_{\min}/2g}$, speed scale $u^* = \sqrt{2ga_{\min}}$, and force scale $F_g = \frac{4}{3}\pi\rho_f(D_I/2)^3 g$. All variations of simulated volume fractions ϕ and box sizes are summarized in Table. 4.1. Note that we use three ensembles for these sets of parameters: (i) $\phi = 0.53$, $W = D = 6D_I$, $H = 3D_I$ and (ii) $\phi = 0.53$, $W = D = 6D_I$, $H = 2D_I$. We only simulate one ensemble for the other cases.

Volume fraction ϕ	Depth H	Width W	No. of particles N
0.00	$3D_I$	$6D_I$	0
0.10	$3D_I$	$6D_I$	409
0.25	$3D_I$	$6D_I$	1021
0.40	$3D_I$	$6D_I$	1634
0.48	$3D_I$	$6D_I$	1960
0.51	$2D_I$	$4D_I$	617
	$3D_I$	$6D_I$	2083
	$6D_I$	$5D_I$	2893
	$7D_I$	$4D_I$	2160
0.53	$2D_I$	$4D_I$	642
	$2D_I$	$6D_I$	1443
	$3D_I$	$6D_I$	2164
	$7D_I$	$4D_I$	2245
0.56	$2D_I$	$4D_I$	677
	$7D_I$	$4D_I$	2371

Table 4.1 All variations of simulated volume fractions ϕ and box sizes with the corresponding numbers of suspended particles N.

4.3 Phenomenology: Floating + force chains model

4.3.1 Overview

We propose the following simple phenomenology to describe the vertical motion of an impactor:

$$m_I \frac{d^2 z_I}{dt^2} = -m_I \tilde{g} + F_D^I, \tag{4.2}$$

where $z_I(t)$ is the vertical position of the center of mass of the impactor, $\tilde{g}$ is the effective gravitational acceleration defined as $\tilde{g} = g(\rho_I - \rho_f)/\rho_f$, and F_D^I is the drag force acting on the impactor. It should be noted that we previously adopted the dynamical Hertzian contact model (DHCM) in Ref. [88] but the predictions of the DHCM, $6/5 < \alpha < 4/3$ and $-1/3 < \beta < -1/5$, disagree with the simulation and experimental results. DHCM has also another drawback in which it cannot recover the u_0 independent regime observed in our simulation. Details on DHCM can be seen in Appendix B.

Brassard et al. [13] proposed the viscous force model with a drag term that is proportional to the depth of the impactor, though their model ignores the gravity term $m_I\tilde{g}$ and the elastic force to reproduce the rebound process. Although their model cannot explain u_0 independent regime and the rebound process, the analytic solution of the model yields $\alpha = 1.5$ and $\beta = -0.5$. Of course, we should take into account the elastic force in the later stage of the impact if there are percolated force chains from the impactor to the bottom plate (Sec. 4.3.3). The model used in Sec. 4.3.3 reduces to the model in Sec. 4.3.2 when the number of percolated force chains $n(t)$ vanishes. Thus, our proposed model in Sec. 4.3.2 is essentially the same as that in Ref. [13] with keeping the gravity term. Nevertheless, explain the floating model with $n(t) = 0$ in Sec. 4.3.2, and introduce the floating + force chain model with $n(t) \neq 0$ in Sec. 4.3.3 separately.

4.3.2 Floating model

Let us propose a simple phenomenology which we call the floating model to explain the behavior of the impactor for both $F_{\max}$ and $t_{\max}$. To model the motion of the impactor, we assume that the impactor is only influenced by the gravity and viscous drag force from the surrounding suspension in the early stage. This assumption is based on the observation that the dynamically jammed region is floating without touching the bottom plate in the early stage of the impact [114, 34]. We also assume that the drag force is proportional to the impactor velocity because the fluid drag should be determined by the Stokes flow. Thus, in order to extract the coefficient, we plot the drag exerted on the impactor F_D^I divided by the

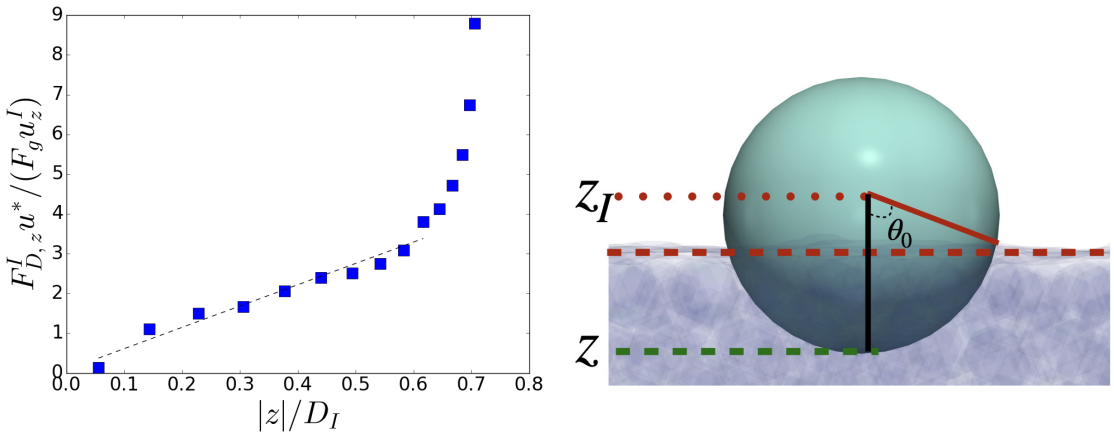

(a) (b)

Fig. 4.2 (a) Plot of the drag exerted on the impactor $F^I_{D,z}$ scaled by F_g and impactor velocity u^I_z/u^* against impactor depth scaled by the diameter of the impactor z_I/D_I. Black dashed line represents the linear fit of $F^I_{D,z}/F_g$ for $z_I/D_I \leq 0.7$. (b) An illustration of an impactor in the suspension liquid to explain z, z_I, and θ_0 (the black solid line connects the deepest position of the impactor at z with the center of mass at z_I, the red solid line is the line between the surface of the suspension and the center of mass, the green dashed line represents the deepest point z, the red dashed line is the surface of the suspension ($z = 0$), and θ_0 is the angle between the black and red solid lines.

velocity against $|z|$ in Fig. 4.2(a), where z is the deepest position of the impactor ($z = 0$ is the instance of the impactor touches the surface of the liquid). Here, we confirm that the drag is proportional to the impactor depth when $|z|/D_I \leq 0.7$. It should be noted that the center of mass of the impactor z_I is related to z as $z_I = z + a_I$.

The linear relationship between $|z|$ and the drag force in Fig. 4.2(a) may be understood by the following simple model. For $|z| < D_I$, the surface of the impactor is partially surrounded by the liquid. Here, we assume that Stokes drag law can be used for the region surrounded by the liquid. Stokes' drag force consists of two parts, the pressure drag $F^I_{D,p}$ and friction drag $F^I_{D,f}$ as $F^I_D = F^I_{D,p} + F^I_{D,f}$ [4],

$$F^I_{D,p} = -3\pi\eta_{\text{eff}} a_I \dot{z}_I \int_0^{\theta_0} \cos^2\theta \sin\theta d\theta, \tag{4.3}$$

$$\begin{aligned} F^I_{D,f} &= -3\pi\eta_{\text{eff}} a_I \dot{z}_I \int_0^{\theta_0} \sin^3\theta d\theta \\ &= -3\pi\eta_{\text{eff}} a_I \dot{z}_I (1 - \cos\theta_0) + F^I_{D,p}, \end{aligned} \tag{4.4}$$

where a_I is the radius of the impactor satisfying $a_I = D_I/2$, η_{eff} is the effective viscosity of the surrounding suspensions, and θ_0 is the separation angle between moving direction

($\theta = 0$) and the line from the impactor center to the surface of the liquid (see Fig. 4.2(b)). Note that the deepest position of the impactor satisfies the relation $|z| = a(1-\cos\theta_0)$. Thus, one can reach

$$F_D^I = -3\pi\eta_{\text{eff}}\dot{z}_I|z|. \tag{4.5}$$

Then, we can write the equation of motion of the impactor as

$$m_I\frac{d^2z_I}{dt^2} = -m_I\tilde{g} - 3\pi\eta_{\text{eff}}\dot{z}_I|z|. \tag{4.6}$$

Equation (4.6) can be solved exactly with the aid of the Airy functions (see Appendix C). The solution of Eq. (4.6) yields

$$\alpha = \frac{3}{2}, \quad \beta = -\frac{1}{2} \tag{4.7}$$

for high u_0. $F_{\max}$ should be independent of u_0 for low u_0 because the second term on the right-hand side (r.h.s.) of Eq. (4.6) is much smaller than the first term for low u_0.

4.3.3 Floating + force chains model

Unfortunately, Eq. (4.6) cannot explain the rebound of the impactor because of the absence of elastic force which is the origin of the rebound. This indicates the drawback of the viscous force model which cannot explain the rebound process. Since the force can be transmitted via contacts of suspended particles along the chains, we can calculate the elastic force along the chains (see Chapter 3 and Appendix D for definition and visualizations of the force chains). Then, we include an elastic term to Eq. (4.6) from the connected force chains between the impactor and bottom plate as

$$m_I\frac{d^2z_I}{dt^2} = -m_I\tilde{g} - 3\pi\eta_{\text{eff}}\dot{z}_I|z| + n(t)k_n|z|, \tag{4.8}$$

where $n(t)$ is the number of connected chains from the impactor to the bottom plate, and k_n is the spring constant between suspended particles in the DEM. In other words, the elastic force (the third term on the r.h.s. of Eq. (4.8)) is originated from the contacting elastic force along the force chains of contacting suspended particles between the impactor and bottom plate. Details of the algorithm to determine $n(t)$ is written in Appendix D. It is obvious that Eq. (4.8) is reduced to Eq. (4.6) if the percolated force chains do not exist, i. e. $n(t) = 0$ in the early stage of the impact. In this sense, the model in Eq. (4.8) is more general than the floating model described by Eq. (4.6).

4.4 Simulation results

4.4.1 Impactor motion: Revisit the rebound motion

In Fig. 4.3, we plot the time evolutions of the velocity and vertical position of the impactor, the force acting on the impactor, and the force acting on the bottom plate obtained from our simulation. From Fig. 4.3(a), one can see the existence of a rebound process i.e. the region with $-u_z^I < 0$. From Fig. 4.3(c), one can define $F_{\max}$ as its peak value and $t_{\max}$ as the time to reach $F_{\max}$. Note that $t_{\max}$ coincides with the onset time of the force exerted on the bottom plate $F_z^{w,b}$, while the rebound takes place around and after the peak of $F_z^{w,b}$ (see Fig. 4.3(d)). This indicates that the rebound of the impactor takes place when the force from the impactor is transmitted through the force chains to the bottom plate.

The solutions for $z_I(t)$, $u_z^I(t) = dz_I(t)/dt$, and $F_z^I(t) = m_I d^2 z_I(t)/dt^2$ from Eq. (4.8) and Eq. (4.6) are plotted alongside the simulation results in Fig. 4.3. We use the value of the effective viscosity $\eta_{\text{eff}} = 4.9 \times 10^4 m_0/(a_{\min} t_g)$ as a fitting parameter. This value is about a hundred times larger than the viscosity of the solvent η_0 and five times larger than the observed viscosity for DST under simple shear using LBM simulation [87]. Such enhancement of viscosity will be explained in detail in the next chapter.

We also find that $t_{\max}$ is located much earlier than the time of the rebound region ($u_z^I < 0$). This suggests that $F_{\max}$ and $t_{\max}$ are not related to the rebound motion. This is consistent with the following observation in which $F_{\max}$ and $t_{\max}$ are independent of system size [13] but the rebound motion strongly depends on the system size. Indeed, as can be seen in Fig. 4.4(a), the rebound takes place only for the suspension in a shallow vessel as in the case of $H = 2D_I$, while the rebound cannot be observed for the suspension in a deep vessel ($H = 3D_I$). At the early stage for $t/t_g < 0.05$, such depth dependence does not exist.

In Fig. 4.4(b), we plot time evolutions of the impactor velocity from our simulation alongside with the corresponding results of Eqs. (4.6) and (4.8) with $\eta_{\text{eff}} = 4.9 \times 10^4 m_0/(a_{\min} t_g)$ and $k_n = 2.5 \times 10^4 m_0/(a_{\min} t_g^2)$. Here, one can see that the rebound of the impactor can be recovered by the introduction of the third term on the r.h.s. of Eq. (4.8) for the shallow vessel case ($H = 2D_I$) (see Fig. 4.4(b)). On the other hand, the floating model (Eq. (4.6)) is sufficient to recover the impactor velocity correctly for the deep vessel case ($H = 3D_I$) where rebound does not take place. Thus, the phenomenology described by Eq. (4.8) can describe the quantitative behavior of the impactor by the introduction of two fitting parameters η_{eff} and $n(t)$, though $n(t)$ is determined by the observation as shown in Appendix D. Thus, our phenomenology is more accurate than the linear model in Ref. [26] and the DHCM in Ref. [88].

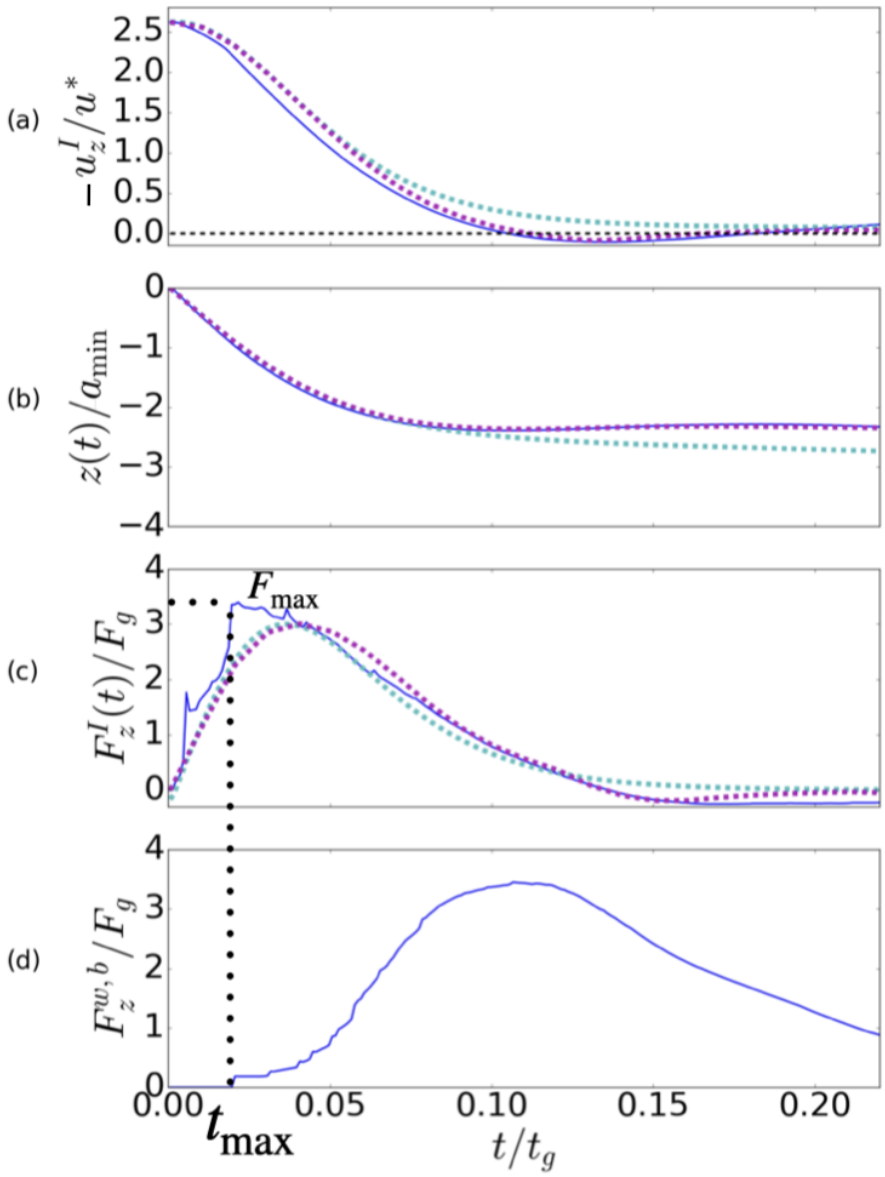

Fig. 4.3 Plots of the time evolutions of the impactor motion (blue solid lines) for $\phi = 0.53$, $W = D = 6D_I$, and $H = 2D_I$ for (a) the velocity u_z^I/u^* (black dashed line represents $u_z^I/u^* = 0$), (b) the position of the deepest point of the impactor $z(t)/a_{\min}$, (c) the force exerted on the impactor F_z^I/F_g, and (d) the force exerted on the bottom plate $F_z^{w,b}/F_g$, respectively. Dashed purple lines in (a), (b), and (c) represent the solution of Eq. (4.8) and dashed light blue lines in (a), (b), and (c) represent the solution of Eq. (4.6). Black dotted lines highlight $F_{\max}$ and $t_{\max}$.

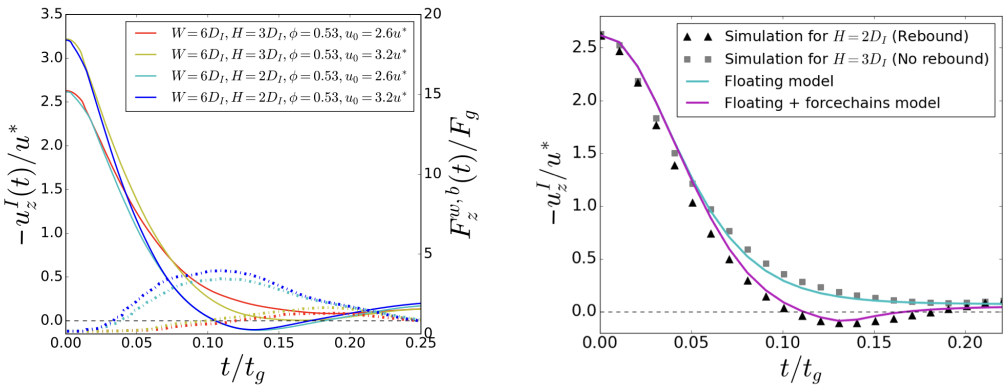

(a) (b)

Fig. 4.4 (a) Plots of the time evolutions of the impactor velocities u_z^I/u^* for $\phi = 0.53$ and $W = D = 6D_I$ (left vertical axis) for various u_0 and H. Blue and cyan solid lines represent the results for $H = 2D_I$ with $u_0/u^* = 3.2$, and $H = 2D_I$ with $u_0/u^* = 2.6$, respectively. Red and yellow solid lines represent the results for $H = 3D_I$ with $u_0/u^* = 3.2$, and $H = 2D_I$ with $u_0/u^* = 2.6$, respectively. Black dashed line represents $u_z^I/u^* = 0$. The dot-dashed lines represent the corresponding forces exerted on the bottom plate $F_z^{w,b}/F_g$ (right vertical axis). (b) Plots of time evolutions of velocities of the impactors for a rebound case with $H = 2D_I$ and a no-rebound case with $H = 3D_I$. Filled triangles represent the simulation results of $\phi = 0.53$, $W = D = 6D_I$, and $H = 2D_I$. The green solid line represents the solution of Eq. (4.6), and the purple solid line represents the solution of Eq. (4.8) (the black dashed line represents $u_z^I/u^* = 0$). Here, we also plot the simulation results for $\phi = 0.53$, $W = D = 6D_I$, and $H = 3D_I$ (black squares), where rebound does not take place.

4.4.2 Relationships among u_0, $F_{\max}$, and $t_{\max}$

In Fig. 4.5, we plot $F_{\max}$ exerted on the impactor scaled by the gravitational force F_g against u_0 for $\phi \geq 0.48$ (see Appendix E for the results of $\phi \leq 0.40$). Here, the results of our simulation for $F_{\max}$ and $t_{\max}$ show the existence of power-law regimes satisfying

$$F_{\max} \propto u_0^{\alpha}, \quad t_{\max} \propto u_0^{\beta} \tag{4.9}$$

with $\alpha = 1.432 \pm 0.003$ and $\beta = -0.523 \pm 0.042$ for $u_0 > u^*$. One can find that the data for all volume fractions and system sizes are collapsed on a universal curve for $F_{\max}$, while $t_{\max}$ does not have such data collapse. The observed exponents from our simulations agree with those in the experiments [114, 13] and is smaller than the solution of the added-mass model [79]. The values of α and β also are very close to those obtained by the viscous force model [13].

Our simulation illustrates that a single power-law is insufficient for $F_{\max}$ versus u_0 to fit the data in all ranges of the impact speed. Instead, we find a crossover of the relation between $F_{\max}$ and u_0 from u_0 independent regime for low u_0 to the power-law region for high u_0 regime (see Fig. 4.5(a)). The corresponding u_0 independent regime of $t_{\max}$ for low u_0 is also visible in Fig. 4.5(b), though it is not as obvious as in the $F_{\max}$ case. Even though the authors of Ref. [114] did not mention such a crossover in their paper, their data suggest the existence of a subtle crossover in the relation between u_0 and $F_{\max}$, similar to what we observe. Furthermore, it is obvious that a set of single values of α and β is no longer valid if the acceleration due to gravity plays some role. This might be the reason why the viscous force model in Ref. [13] cannot explain the existence of u_0 independent regime.

The numerical solutions for $F_{\max}$ and $t_{\max}$ (the blue solid lines) are presented in Figs. 4.5(a) and 4.5(b), respectively. We use the value of the effective viscosity $\eta_{\text{eff}} = 4.9 \times 10^4 m_0/(a_{\min} t_g)$ as a fitting parameter. One can see that Eq. (4.6) can recover the crossover from u_0 independent regime for low u_0 to the power-law regime for high u_0 observed in our simulations. This is understandable since the peak of the force exists in the early stage where the elastic force to produce the rebound does not play any role. Thus, one does not need to take into account the elastic force to explain the relations among u_0, $F_{\max}$, and $t_{\max}$. Moreover, we have simulated variations of widths and depths in Fig. 4.5 to confirm that the relations among u_0, $F_{\max}$, and $t_{\max}$ are independent of the system size. This is in contrast to the rebound phenomenon which strongly depends on the width and depth of the simulation box (see Fig. 4.4). This observation is another evidence that the relations among u_0, $F_{\max}$, and $t_{\max}$ are not related to the rebound phenomenon.

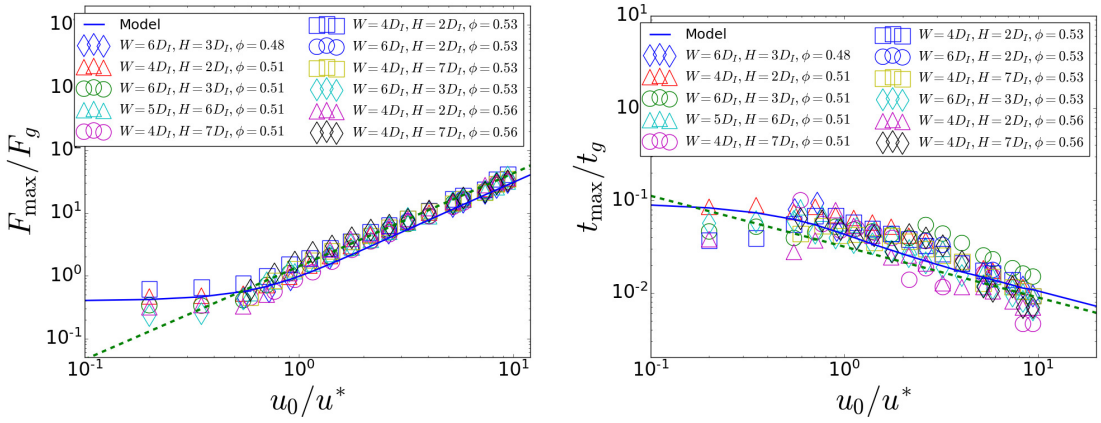

(a) (b)

Fig. 4.5 (a) Plots of maximum forces exerted on the impactor $F_{\max}$ scaled by the gravitational force F_g against u_0/u^* for various container sizes, where the green dashed line represents $1.58(u_0/u^*)^{1.432}$. (b) Plots of time $t_{\max}$ to reach $F_{\max}$ scaled by t_g against u_0/u^*, where the green dashed line represents $0.03(u_0/u^*)^{-0.523}$. The blue solid lines in both figures represent the solution of the floating model (Eq. (4.6)).

4.5 Summary of this chapter

We have numerically studied the impact processes on dense suspensions using a coupled model of LBM and DEM to elucidate the connection between the elastic rebound of the impactor and the relations among u_0, $F_{\max}$, and $t_{\max}$. Then, we have also proposed a simple phenomenology called the floating + force chain model to explain our simulation results. This model reduces to the floating model if there are no percolated force chains from the impactor to the bottom plate. We numerically find the existence of a power-law regime satisfying $F_{\max} \propto u_0^{\alpha}$, with $\alpha = 1.432 \pm 0.003$ and $t_{\max} \propto u_0^{\beta}$, with $\beta = -0.523 \pm 0.042$, while the analytic solution of the floating model indicates $\alpha = 3/2$ and $\beta = -1/2$. We have also confirmed the existence of u_0-independent regimes of $F_{\max}$ and $t_{\max}$ for low u_0. The crossovers of $F_{\max}$ and $t_{\max}$ from u_0-independent regimes to the power-law regimes can be reproduced by the floating model correctly. We conclude that the relations among u_0, $F_{\max}$, and $t_{\max}$ are not related to the rebound process based on three observations: (i) We found that $F_{\max}$ emerges in the early stage of the impact, while the rebound of the impactor takes place in the later stage. (ii) We have confirmed that the relations among u_0, $F_{\max}$, and $t_{\max}$ are independent of the system size, while the rebound strongly depends on the size of the container. (iii) One can recover the exponents for $F_{\max}$ and $t_{\max}$ with a drag term that is proportional to the impactor depth without considering any elastic force, which agrees with Ref. [13]. In contrast, rebound requires an elastic term from the percolated force chains.

Chapter 5

Effective viscosity and elasticity of dynamically jammed region and their role for the hopping motion on dense suspensions

5.1 Introduction

People being able to run on top of dense suspension has attracted the interest of scientists as well as the general public [16, 80]. Most physical studies for impact-induced hardening use a free-falling impactor (as we have discussed in Chapter 3 and Chapter 4) or a constant speed penetrating intruder. We have also mentioned that using a free-falling impactor, Ref. [114] reported the existence of a localized rigid region beneath the impactor called the dynamically jammed region (DJR). In Chapter 3, we observed that such a region corresponds to the force chains formed by contacting suspended particles. Since such a DJR grows in size, Ref. [114] proposed the added-mass model, which treats the impact as an inelastic collision between the impactor and the DJR that evolves with time. Then, Ref. [34] visualized the flow field inside dense suspensions around penetrating intruder and found that the strain rate peaked on the boundary of the DJR. Inspired by this observation, Ref. [13] proposed a model based on the viscous force acting on the boundary of the DJR. Yet, none of the above models can explain the existence of elastic response of dense suspensions under impacts such as fractures [95], high stress near boundary [71], and rebound of the impactor [26]. Reference [71] proposed a constitutive model and measured the elastic modulus once the DJR spans from the impactor to the boundary. In Chapter 4, the viscoelastic response of dense suspensions

under the impact is captured using the floating + force chains model [89], where percolated force chains of contacting suspended particles are necessary to recover the elastic motion. However, such a picture neglects the fact that even if the force chains are not touching the boundary, the DJR itself might have effective elasticity. Therefore, the rigidity of such a DJR needs to be thoroughly investigated.

The motion of a running or walking person is more complicated than the free-falling impactor or penetrating intruder. One particular approach to directly investigate the running motion on the suspensions has been carried out in Ref. [79]. They discussed the maximum penetration depth of a foot for various impact velocities corresponding to walking, jogging, and running, and fit the data using a constitutive model with the aid of the elastic modulus obtained in Ref. [71]. They also showed that the added mass model is not sufficient to recover the response of the suspensions under running motion. Nevertheless, little is still known about the dynamics of multiple impacts on dense suspensions, which are important for running and walking motions. Some studies have tried to reproduce mechanical models for legged animal locomotions. One of the simplest and most celebrated models is the spring-mass model inspired by biomechanical observations [9]. Such a model has been realized as a one-legged hopping robot [93]. In the spring-mass model, the human leg is represented by a spring and the human body is simply represented by a point mass. Inspired by such a model, we study a foot-spring-body system in dense suspensions in this chapter.

This chapter corresponds to Ref. [90]. The structure of this chapter is as follows. In Sec. 5.2, we describe the coarse-graining method to characterize the elasticity and viscosity of the DJR. We compare the result of the model including the effective elasticity and that of the floating model without elasticity [89] to clarify the role of elasticity of the DJR when force chains are not connected with the bottom boundaries. We then extend the previous floating + force chains model to include the effective elasticity. In Sec. 5.3, we describe the simulation setup for the foot-spring-body model. By using the coarse-graining method, we discuss the hopping motion of such a system to clarify the criterion for the hopping motion. Finally in Sec. 5.4, we conclude our findings.

5.2 Dynamical jammed region model with effective viscosity and elasticity

5.2.1 Setup for a free-falling impactor simulation

We adopt the coupled LBM-DEM simulation as in Chapters 3 and 4. Details of the simulation method can be seen in Chapter 2. The simulation setup for this section is as follows. A

suspension with N particles and volume fraction ϕ is contained in a box sized $W \times H \times D$. We have adopted the perfect density matching between the solvent and suspended particles, where the densities of particles and solvent satisfy the relation $\rho_p = \rho_f$, where ρ_p and ρ_f are the densities of a suspended particle and solvent fluid, respectively. In this section, a spherical impactor with the diameter D_I and density ρ_I, is released from the height H_0 which corresponds to the impact speed $u_0 = \sqrt{2gH_0}$ with the gravitational acceleration g. In our simulation ρ_I and D_I satisfy $\rho_I = 4\rho_f$ and $D_I = 6a_{\min}$, respectively, where $a_{\min}$ is the radius of smallest suspended particle. We also introduce the time scale $t_g = \sqrt{a_{\min}/2g}$, speed scale $u^* = \sqrt{2ga_{\min}}$, and force scale $F_g = \frac{4}{3}\pi\rho_f(D_I/2)^3 g$. We evaluate the impactor motions in deep and shallow containers. Here we use $\phi = 0.53$, $H = 3D_I$, $W = D = 4D_I$, and $N = 960$ for the deep container case and $\phi = 0.53$, $H = 2D_I$, $W = D = 4D_I$, and $N = 670$ for the shallow case.

5.2.2 Coarse-graining method and delineating the dynamically jammed region

The DJR can be defined once we obtain the strain rate, strain, and stress field inside the suspensions. The approximate description of such fields from discrete particle data can be carried out using the coarse-graining method that has been used in granular materials [119, 99]. As an example, the discrete particle data for microscopic mass density ρ^{dis} at position $\boldsymbol{r}$ and time t can be expressed as

$$\rho^{\mathrm{dis}}(\boldsymbol{r},t) = \sum_i m_i \delta(\boldsymbol{r} - \boldsymbol{r}_i(t)), \tag{5.1}$$

where $\boldsymbol{r}_i$ and m_i are the position and mass of particle i, respectively. For smoothed and coarse-grained density ρ, the delta function in Eq. (5.1) is replaced with a coarse-graining function $\Phi(\boldsymbol{r})$ as

$$\rho(\boldsymbol{r},t) = \sum_i m_i \Phi(\boldsymbol{r} - \boldsymbol{r}_i(t)). \tag{5.2}$$

Here, we adopt a Gaussian with width w

$$\Phi(\boldsymbol{r} - \boldsymbol{r}_i) = \frac{1}{(w\sqrt{2\pi})^3} \exp\left[-\frac{(\boldsymbol{r} - \boldsymbol{r}_i)^2}{2w^2}\right], \tag{5.3}$$

where $\boldsymbol{r} = (x, y, z)$ and $\boldsymbol{r}_i = (x_i, y_i, z_i)$ are the field position and particle position, respectively. Similarly, the coarse-grained momentum density $\boldsymbol{p}(\boldsymbol{r}, t)$ can be introduced as

$$\boldsymbol{p}(\boldsymbol{r}, t) = \sum_i m_i \boldsymbol{u}_i(t) \Phi(\boldsymbol{r} - \boldsymbol{r}_i(t)), \tag{5.4}$$

where $\boldsymbol{u}_i$ is the velocity of particle i. The velocity field $\boldsymbol{u}(\boldsymbol{r}, t)$ is defined by $\boldsymbol{u}(\boldsymbol{r}, t) = \boldsymbol{p}(\boldsymbol{r}, t)/\rho(\boldsymbol{r}, t)$. The stress tensor $\overleftrightarrow{\sigma}$ contains the contributions from the contact $\overleftrightarrow{\sigma}^c$ and hydrodynamics $\overleftrightarrow{\sigma}^h$

$$\overleftrightarrow{\sigma} = \overleftrightarrow{\sigma}^h + \overleftrightarrow{\sigma}^c. \tag{5.5}$$

The contact contribution is calculated from the pairwise contact force

$$\overleftrightarrow{\sigma}^c(\boldsymbol{r}) = -\frac{1}{2} \sum_{i,j} \boldsymbol{F}^c_{ij} \otimes \boldsymbol{r}_{ij} \Phi(\boldsymbol{r} - \boldsymbol{r}_i) \tag{5.6}$$

where $\boldsymbol{F}^c_{ij}$ and $\boldsymbol{r}_{ij}$ are the pairwise contact force and the interparticle distance between particles i and j, respectively. Here $\otimes$ denotes the tensor product. Meanwhile, the hydrodynamic contribution is given as

$$\overleftrightarrow{\sigma}^h(\boldsymbol{r}) = \sum_i \overleftrightarrow{\sigma}^h_i \Phi(\boldsymbol{r} - \boldsymbol{r}_i), \tag{5.7}$$

where $\overleftrightarrow{\sigma}^h_i$ is the hydrodynamic stress tensor on each particle, obtained from the LBM and lubrication stresslet (See Chapter 2 for details). The vector field of particle overlaps $\boldsymbol{\delta}_n$ (which represents the deformation) can be obtained from the contact overlap on each particle $\boldsymbol{\delta}^i_n$

$$\boldsymbol{\delta}_n = \sum_i \boldsymbol{\delta}^i_n \Phi(\boldsymbol{r} - \boldsymbol{r}_i). \tag{5.8}$$

Note that we ignore the contributions from rattlers.

Once the flow field is obtained, one can get the symmetric part of the strain rate tensor $\overleftrightarrow{D}$

$$\overleftrightarrow{D} = \frac{1}{2}(\nabla \boldsymbol{u} + \nabla \boldsymbol{u}^T). \tag{5.9}$$

Meanwhile, the strain tensor $\overleftrightarrow{L}$ is defined as

$$\overleftrightarrow{L} = \frac{1}{2}(\nabla \boldsymbol{\delta}_n + \nabla \boldsymbol{\delta}_n^T). \tag{5.10}$$

Let us introduce the scalar viscosity η defined as [31, 32],

$$\eta = \frac{1}{2} \frac{\overleftrightarrow{\sigma} : \overleftrightarrow{D}}{\overleftrightarrow{D} : \overleftrightarrow{D}}, \tag{5.11}$$

where : denotes the scalar or double inner product. The strain rate $\dot{\varepsilon}$ is defined as

$$\dot{\varepsilon} = \sqrt{2\overleftrightarrow{D} : \overleftrightarrow{D}}. \tag{5.12}$$

The field of $\dot{\varepsilon}$ can be seen in Fig. 5.1(a). Then, the effective viscous stress $\sigma^{(\mathrm{vis})}$ is simply given by [31, 32]

$$\sigma^{(\mathrm{vis})} = \eta\dot{\varepsilon}. \tag{5.13}$$

Note that $\sigma^{(\mathrm{vis})}$ contains both the contributions from the normal and shear parts, though, as shown in Ref. [88], it is dominated by the normal part. Finally, similar to the strain rate, the scalar strain field ε is defined as

$$\varepsilon = \sqrt{2\overleftrightarrow{L} : \overleftrightarrow{L}}. \tag{5.14}$$

Similar to Eq. (5.11) one can introduce the rigidity as

$$G = \frac{1}{2}\frac{\overleftrightarrow{\sigma} : \overleftrightarrow{L}}{\overleftrightarrow{L} : \overleftrightarrow{L}}. \tag{5.15}$$

Thus, the effective elastic stress is given by

$$\sigma^{(\mathrm{el})} = G\varepsilon. \tag{5.16}$$

5.2.3 The dynamically jammed region

The DJR can be defined in the following two ways. First, it can be delineated from the strain rate field since the front of the DJR corresponds to the peak in the strain rate field [34]. As shown in Fig. 5.1(a), the $z-$position of the peak of $\dot{\varepsilon}$ is denoted as z_{front}. The height of the DJR H_{djr} is defined as the distance between the front and the deepest point of the impactor. Thus, one can approximate the DJR as a hemisphere with radius H_{djr} (the red shaded region in Fig. 5.1(b)). We denote this approach the $\dot{\varepsilon}-$based delineation of the DJR. Alternatively, we can also define the DJR as the region that has non-zero rigidity G (yellow shaded region in Fig. 5.1(b)). We denote this approach as the $G-$based delineation of the DJR. Such $G-$based delineation of the DJR essentially represents the region formed by contacting suspended particles. As one can see in Fig. 5.1(b), both delineations yield qualitatively similar regions.

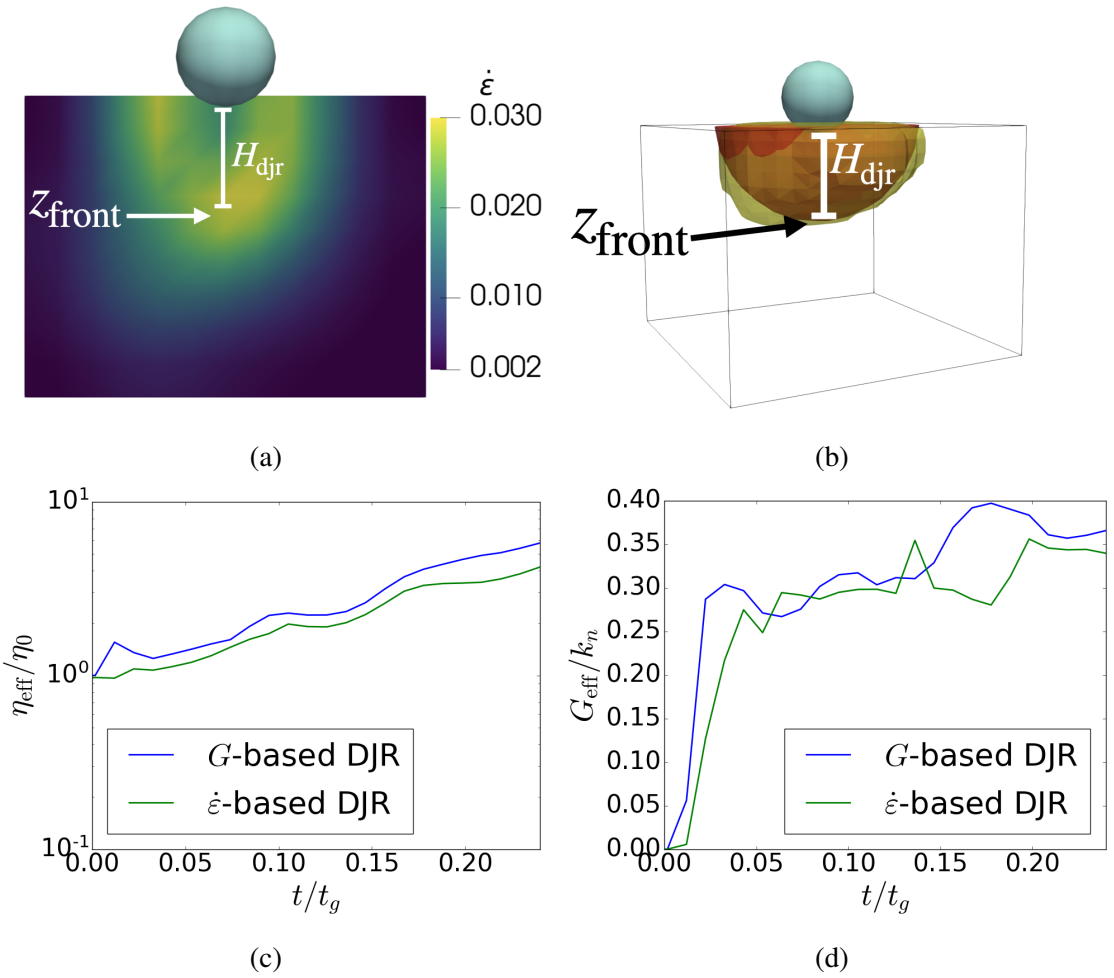

Fig. 5.1 (a) Strain rate $\dot{\varepsilon}$ field with its peak annotated as the front of the DJR z_{front} and H_{djr} is the distance between z_{front} and the deepest point of the impactor. (b) The delineated DJR, the red region represents the $\dot{\varepsilon}-$based delineation and the yellow region represents the $G-$based delineation. The z_{front} and H_{djr} in (a) are also annotated here. (c) Time evolutions of the effective viscosity $\eta_{\mathrm{eff}}/\eta_0$ based on $\dot{\varepsilon}$-based DJR and $G-$based DJR. (d) Time evolutions of the effective rigidity G_{eff}/k_n based on $\dot{\varepsilon}-$based DJR and $G-$based DJR.

Once the DJR is delineated, one can obtain the effective quantities by integrating the viscosity η and rigidity G fields over the region shown in Fig. 5.1(b) as

$$\eta_{\text{eff}} = \eta_0 + \frac{1}{V_{\text{djr}}}\int_d \eta dV, \qquad G_{\text{eff}} = \frac{1}{V_{\text{djr}}}\int_d G dV, \tag{5.17}$$

where d represents the region enclosed by the yellow or red surface in Fig. 5.1(b), and V_{djr} is its volume. Here, η_0 is the apparent viscosity of the suspensions, multiplied by the solvent viscosity before the impact. In Figs. 5.1(c) and 5.1(d), we plot the time evolutions of the effective viscosity η_{eff} and rigidity G_{eff} obtained from the $\dot{\varepsilon}-$based delination of the DJR as well as the $G-$based delination of the DJR. For the viscosity, one can see that η_{eff} increases with time. This confirms the enhancement of the effective viscosity as the result of the impact, as indicated in the previous chapter. We also observe non-zero rigidity even when the DJR does not touch the bottom boundary. One can see that the $\dot{\varepsilon}-$based and the $G-$based delineations yield a qualitatively similar effective viscosity η_{eff} and rigidity G_{eff}. However, quantitative differences exist since the $\dot{\varepsilon}-$based delineations approximate the region as a hemisphere. From the next subsection onwards, we solely use the $G-$based delineation of the DJR to obtain the effective quantities.

5.2.4 Updated viscoelastic model with effective viscosity and elasticity

In the floating + force chains model in Chapter 4, the elastic response only exists when the force chains percolate. Now, we include the effect of elastic response through the elastic modulus of the DJR even if the force chains are not percolated in the present chapter. Thus, we propose the dynamically-jammed-region (DJR) model as

$$m_I \ddot{z}_I = -m_I g - 3\pi\eta_{\text{eff}}(t)|z|\dot{z}_I + Ck_{\text{eff}}(t)|z|, \tag{5.18}$$

where m_I is the mass of impactor, z is the deepest point of the impactor, z_I is the vertical position of the impactor, $\ddot{z}_I := d^2 z_I/dt^2$, k_{eff} is the effective spring constant defined as $k_{\text{eff}} = G_{\text{eff}}(t)A_D/H_D$, with A_D and H_D are the top surface area and height of the dynamically jammed region, respectively. We also introduce a fitting parameter C which is the order of unity.

First, we check the validity of the DJR model for the case without rebound and percolating force chains (impact velocity $u_0 = 1.8u^*$, deep container with $H = 3D_I$). In Fig. 5.2(a), we plot the solution of Eq. (5.18) for both the solution of the DJR model with $C = 1.0$ and the solution from the floating model with a fitting parameter η'_{eff}. One can see that both solutions agree well with the results of the simulation while they have subtle differences.

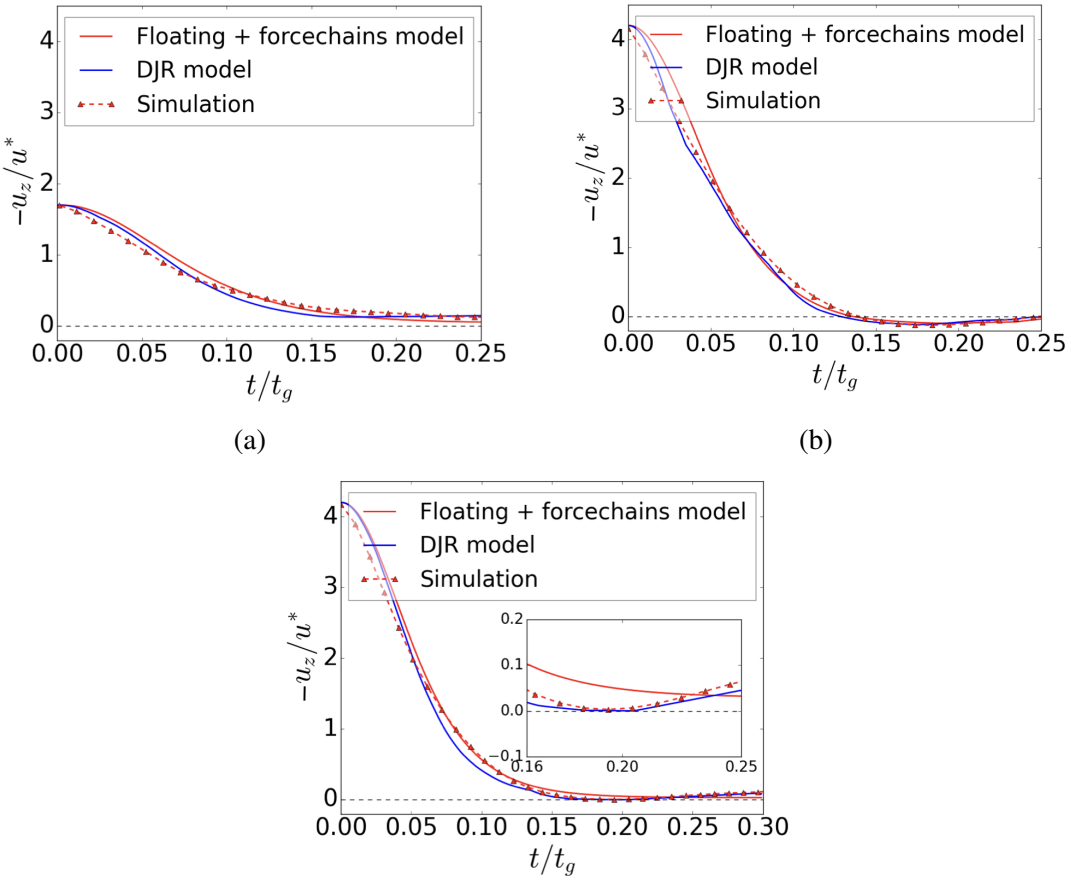

Fig. 5.2 Time evolutions of the impactor velocity u_z/u^* under various situations: (a) Solution of Eq. (5.18) is plotted alongside simulation results and the floating model [89] without rebound and percolating force chains (impact velocity $u_0 = 1.8u^*$, deep container with $H = 3D_I$). (b) Solution of Eq. (5.18) is plotted alongside simulation results and the floating + force chains model[89] for the case with rebound and percolating force chains (impact velocity $u_0 = 4.2u^*$, shallow container with $H = 2D_I$). (c) Solution of Eq. (5.18) is plotted alongside simulation results and the floating model [89]] for the case without percolating force chains but with a small elastic response (impact velocity $u_0 = 4.2u^*$, deep container with $H = 3D_I$). The inset of (c) shows the magnified impactor velocity around the elastic response.

Then, we check Eq. (5.18) for the case of rebound and percolating force chains (impact velocity $u_0 = 4.2u^*$, shallow container with $H = 2D_I$). In Fig. 5.2(b), we plot the solution of Eq. (5.18) for the DJR model with $C = 0.9$ alongside with the solution from the floating + force chains model with fitting parameters η'_{eff}, and $n(t)$ as in Ref. [89]. In this case, the DJR percolates and is spanned throughout the system, thus enhancing the elastic response. Although the floating+force chains model reproduces the result of the simulation almost perfectly, while the results of the DJR model seem to have slight deviations for a relatively short time regime. Finally, we examine Eq. (5.18) for the case without percolating force chains but with a small elastic response (impact velocity $u_0 = 4.2u^*$, deep container with $H = 3D_I$). In Fig. 5.2(c), we plot the solution of Eq. (5.18) for the DJR model with $C = 0.8$, alongside with the solution from the floating model with a fitting parameter η'_{eff}. The floating model cannot capture the elastic rebound, while the DJR model can (see the inset of Fig. 5.2(c)), though the solution of the DJR model slightly deviate from the result of the simulation around $t/t_g = 0.1$. Thus, the ability to describe the elastic response without non-percolating force chains is the advantage of the DJR model.

5.3 Foot-spring-body dynamics in dense suspensions

Now let us introduce the foot-spring-body model as a toy model to express a bouncing motion on suspension liquids. The foot in the foot-spring-body model is expressed as a rectangular plate impactor with volume $V_p = W_p \times H_p \times D_p$ and mass $m_p = V_p\rho_p$, where ρ_p is the density of the foot plate and we adopt $\rho_p = 1.2\rho_f$. The body is represented by a sphere with diameter D_b and mass m_b. We adopt the density of the body ρ_b as $\rho_b = 2\rho_p = 2.4\rho_f$. The body and the foot are then connected with a massless spring with the stiffness k_s and natural length L_0. Here we use $\phi = 0.51$, $H = 2D_b$, $W = D = 4D_b$, and $N = 618$. Note that we are only interested in the vertical (z direction) motion of the system. We then modify Eq. (5.18) to be the set of equations

$$\begin{aligned} m_b\ddot{z}_b &= -m_bg - k_s(z_b - z_p - L_0) - \zeta_s\dot{z}_b \\ m_p\ddot{z}_p &= -m_pg - 3\pi\eta_{\text{eff}}(t)z\dot{z}_p + Ck_{\text{eff}}(t)|z| \\ &\quad + k_s(z_b - z_p - L_0) - \zeta_s\dot{z}_p, \end{aligned} \tag{5.19}$$

where m_b and z_b are the mass and the vertical position of the body, respectively, z_p is the vertical position of the plate impactor, ζ_s is the damping constant, $\zeta_s = \sqrt{k_s(m_p + m_b)/2}$. With the parallel procedure to the free-falling case, one can draw the DJR induced by the impact between the foot and the suspensions. The illustration of this setup and the DJR

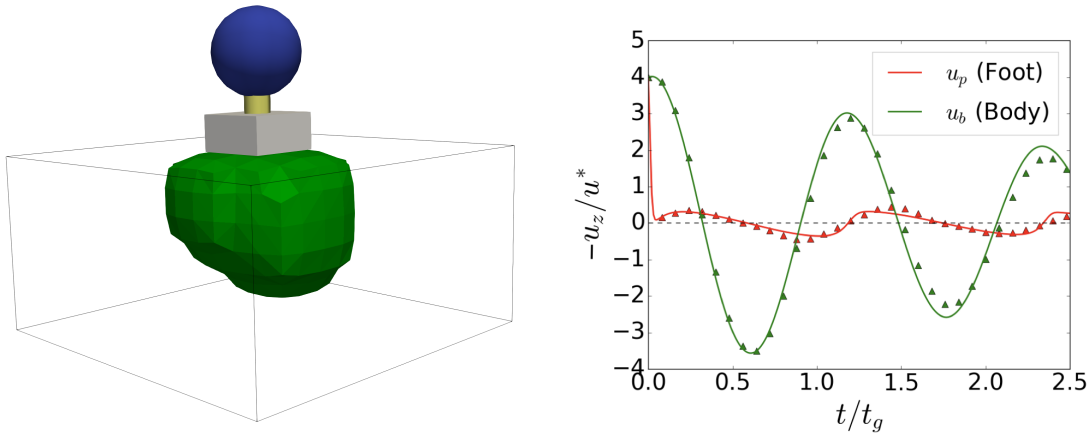

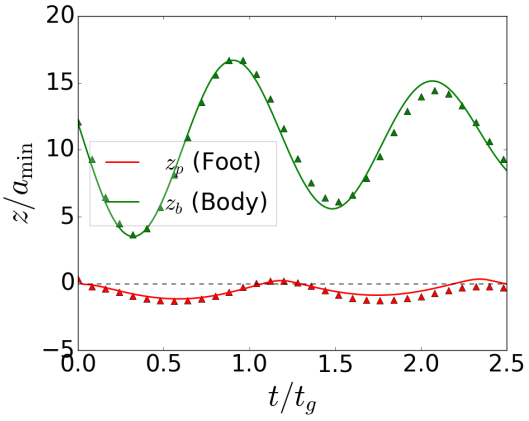

Fig. 5.3 (a) A snapshot of the simulation of the foot-spring-body system. The body (blue sphere) is connected with the foot (grey plate) by a massless spring (yellow tube). The green region expresses the surface of the DJR. (b) Time evolutions of the velocities of the foot (reds) and body (greens) in $z-$coordinate, where the black dashed line expresses $u_z = 0$, the solid lines express the solutions of Eq. (5.19), and the triangles express the results of the simulations. (c) Time evolutions of the positions of the foot (reds) and body (greens) in $z-$coordinate, where the black dashed line expresses the suspension surface, the solid lines express the solutions of Eq. (5.19), and the triangles express the results of the simulations. All results here are obtained with $k_s = 100m_0/(a_{\min}t_g^2)$ and $u_0 = 4u^*$.

induced by the impact can be seen in Fig. 5.3(a). A typical motion of the foot-spring-body system can be seen in Figs. 5.3(b) and 5.3(c). Here, we adopt $C = 0.9$. One can see that the solution of Eq. (5.19) agrees well with the results of the simulation. Initially, the foot experiences a strong deceleration as in the free-falling impactor due to the interaction between the foot and suspensions. Meanwhile, the body still accelerates due to gravity. Then, the system exhibits a damped oscillation. Thanks to the spring force and the rigidity of the suspensions, the foot undergoes multiple rebounds ($u_p < 0$), and also hops ($z_p > 0$) multiple times. This result suggests that composite materials including elastic springs inside the body can maintain their position for a while. This is the first step to realizing the running process on a suspension.

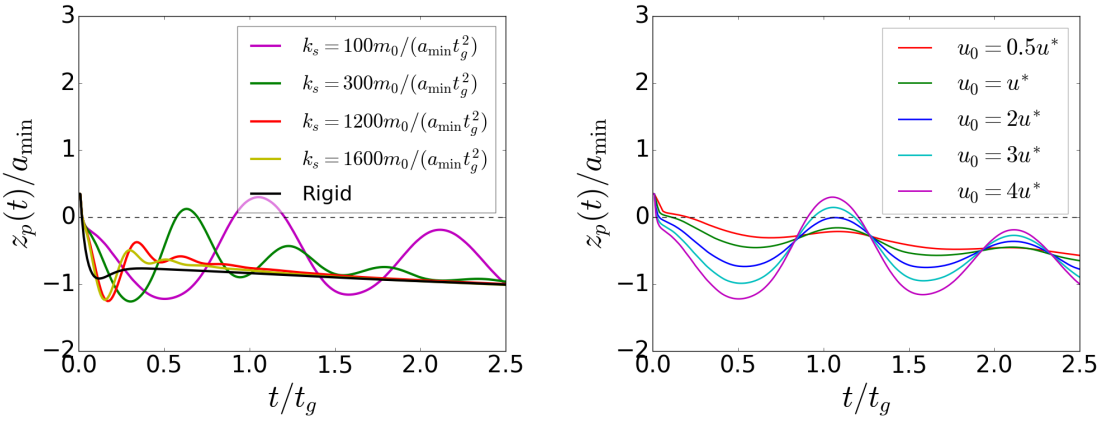

(a) (b)

Fig. 5.4 Time evolutions of the foot position in $z-$direction z_p with (a) various spring stiffness k_s at $u_0 = 4u^*$ and (b) various initial velocity u_0 at $k_s = 100m_0/(a_{\min}t_g^2)$.

We then evaluate the multiple rebound motion of the foot in detail. First, we check how the motion of the foot depends on the stiffness of the spring k_s. The simulation results for various k_s are presented in Fig. 5.4(a). Here one can see a lower tendency to have multiple rebounds or hops for higher k_s. Moreover, for a rigid system ($k_s \to \infty$), the foot only rebound once and then sink afterwards. This is similar to the prediction by the added-mass model in Ref. [79], where they suggested that running on top of suspensions is impossible for a perfectly stiff leg. Then, we check the initial velocity (u_0) dependences in Fig. 5.4(b). As one might expect, the foot sinks and does not hop for low u_0 since the impact-induced hardening is stronger for high u_0 [114, 26, 13, 88].

5.4 Summary of this chapter

With the aid of a coarse-graining method of the simulation results, we quantified the DJR induced by the impact on dense suspensions and measured its effective viscosity and elasticity. As a benchmark, we used the obtained viscosity and modulus and extend the floating + force chains model in Chapter 4, so that such a model can capture the elastic motion even when the DJR does not touch the bottom plate. We found good agreements between the simulation results and the DJR model. To mimic the hopping motion, we discussed the impact of the foot-spring-body system on the top of dense suspensions. We found that the foot undergoes multiple rebounds and also hops multiple times due to the spring force and the rigidity of the suspensions. The DJR model also agrees well with the simulation results for the foot-spring-body system. Finally, we found a lower tendency for hopping and multiple rebounds in higher spring stiffness k_s and low initial velocity u_0.

Chapter 6

Conclusions and outlook

6.1 Conclusions

In this thesis, we numerically and theoretically studied the transient response of dense non-Brownian suspensions under impacts. We used the coupled lattice Boltzmann method and discrete element method (LBM-DEM) simulations. Here, the hydrodynamic interactions were solved using LBM and lubrication corrections. Within the LBM framework, the free surface of suspensions was also simulated. Then, the contact between suspended particles was simulated using DEM.

In Chapter 3, we investigated the case of free-falling impactor into dense suspensions. We observed a rebound of the impactor at high impact speed and high volume fraction. We also found stronger rebounds for stronger frictional contact between suspended particles. By visualizing each suspended particle, we observed the emergence of the dynamically jammed region (DJR) with a distinctively huge value of particle normal stress σ^i_{zz}, formed by force chains of contacting particles. However, the particle shear stress σ^i_{xz} of the suspension is not significantly affected by the impact. This distinguishes the impact-induced hardening from shear-induced phenomena such as discontinuous shear thickening (DST) and shear jamming. Finally, using persistent homology, we could (i) provide quantitative proof of the existence of a system-spanning dynamically jammed region, (ii) determine that only the topological structure of the force chains is important for the contact force acting on the impactor, and (iii) find that the force networks do not form persistent loops, in contrast to DST.

In Chapter 4, we focused on the connection between the elastic rebound of the free-falling impactor and the relations among the impact speed u_0, the maximum force exerted on the impactor $F_{\max}$, and the time to reach it $t_{\max}$. We also proposed a simple phenomenology called the floating+force chain model to explain the motion of the impactor. We numerically found the existence of a power-law regime satisfying $F_{\max} \propto u_0^{\alpha}$, with $\alpha = 1.432 \pm 0.003$ and

$t_{\max} \propto u_0^{\beta}$, with $\beta = -0.523 \pm 0.042$, while the analytic solution of the floating model yields $\alpha = 3/2$ and $\beta = -1/2$. We also observed crossovers of $F_{\max}$ and $t_{\max}$ from u_0-independent regimes to the power-law regimes and such crossovers can be correctly reproduced by the floating model. We concluded that the relations among u_0, $F_{\max}$, and $t_{\max}$ are not related to the rebound process based on: (i) We confirmed that the relations among u_0, $F_{\max}$, and $t_{\max}$ are independent of the system size, while the rebound strongly depends on the size of the container. (ii) We found that $F_{\max}$ emerges in the early stage of the impact, while the rebound of the impactor takes place in the later stage. (iii) The exponents for $F_{\max}$ and $t_{\max}$ can be recovered without considering any elastic force, In contrast, the rebound needs an elastic term caused by the percolated force chains from the impactor to the bottom plate.

In Chapter 5, we delineated the DJR induced by the impact on dense suspensions and quantified its effective viscosity and elasticity. The delineation of the DJR was performed by coarse-graining our simulation data. We used the obtained viscosity and elastic modulus and extended the floating + force chains model in Chapter 4 to capture the elastic motion even when the DJR does not touch the bottom plate. The simulation results and the DJR model were found to be in good agreement. The impact of the foot-spring-body system on the top of dense suspensions was discussed to mimic the hopping motion. The foot undergoes multiple rebounds and also hops multiple times due to the spring force and the rigidity of the suspensions. The DJR model matches the simulation results closely, and we discovered that higher spring stiffness k_s and low initial velocity u_0 have a lower tendency for hopping and multiple rebounds.

6.2 Outlook

This thesis has elucidated the role of the particle-level interactions in the transient macroscopic behavior of dense suspensions through numerical simulations. Such particle-level interactions have not been confirmed experimentally. In particular, one can reproduce our finding in Chapter 3 that the response to the impact is affected by the friction coefficient between suspended particles through experiments. For steady-state experiments, it has been demonstrated that the shape and the asperity of the suspended particles can be controlled [40]. We also have discussed the role of force chains in dense suspensions under impact. Not only in dense suspensions, but such force chains also have important roles in the macroscopic behavior of dry granular materials. In fact, similar force networks are observed in a variety of other aggregates of athermal particles, such as emulsions, foams, and living cells. This makes the force chains deserve studies on their own. Through studying the spatial correlation of the contact network in dry granular materials, Ref. [47] suggested that the force chains arise from

the topological constraint of the contact network rather than the details of the interaction force and the balance of force and torque on each particle. This is analogous to the conclusions drawn by persistent homology analysis of the contact network of dense suspensions under impact in Chapter 3. Indeed, studies within this line appear to be a worthwhile pursuit.

In Chapter 5, we have delineated the dynamically jammed region induced by the impact on dense suspensions and quantified its effective viscosity and rigidity from simulation data. Indeed, it is necessary to construct the equation of motion of the DJR itself. The model for the growth of z_{front} with a constant penetrating intruder has been proposed [34, 35]. However, little is known about the relaxation process of the DJR, which is necessary to reproduce the time evolution of the DJR in the cases of the free-falling impactor, hopping foot-spring-body system, as well for the sinking process. Thus, it is important to investigate how the DJR relaxes. Moreover, the usage of particle-based simulation in the DJR studies allows future research to study the microscopic properties of the DJR in more detail. In addition to the DST under simple shear and the impact-induced hardening, the motion of a sinking intruder in dense suspensions also exhibits interesting behavior. Ref. [113] reported oscillations and stick-slip motions of such a sinking intruder. One could hypothesize that the origin of such stick-slip motions is the emergence and cessation of the DJR. It would be interesting to investigate such behavior with the method explained in Chapter 5. We have discussed the foot-spring-body system in Chapter 5 and our results indicate that hopping on top of dense suspensions will not be possible for a perfectly stiff leg. However, our analysis still ignores the horizontal motion of the system, whereas the actual one-legged robot can also hop horizontally [93]. Thus, it might be of interest for future research to simulate or experimentally investigate the motion of a more realistic hopper on top of dense suspensions. Efforts in this line of research will be useful to understand the ability of people to run on top of dense suspensions and to create a robot that can actually hop or run on top of dense suspensions.

In Chapter 4, We have discussed the viscoelastic response of dense suspensions under impact. Such viscoelastic materials are ubiquitous in nature and have a wide range of applications. Human and animal tissues can also be regarded as viscoelastic materials. Thus, understanding the penetration dynamics on viscoelastic materials can elucidate the response of tissues under disturbance such as drug injections [107]. A recent approach using photoelastic measurement has shed a light on distinct spatiotemporal stress distributions in gelatin under different types of injection, including needle-free injection with up to $200\mathrm{m/s}$ penetration speed [77]. The spatial stress distributions exhibit a high-stress region with a sharp interface, reminiscent of what we have observed and discussed in Chapter 3 and Chapter 5. However, for dense suspension cases, the high stress region is localized in the

normal direction of the penetration, while for gelatin, the stress is localized in the lateral directions. It is then natural to ask whether such difference arises from different microscopic interactions of the viscoelastic materials or if there are other underlying mechanisms beneath this phenomenon. Thus, more detailed and comprehensive studies regarding the penetration dynamics of the human and animal tissues will be necessary.

In contrast to the passive suspensions system discussed in this thesis, active suspensions contains constituent elements that consume energy to move. Active matter can be classified further as dry (no momentum conservation) and wet (momentum conserved through coupling with solvent fluid). Wet active suspensions are less studied compared to their dry counterparts. The most common model to describe motile particles in solvent is the squirmer model, which is based on the polynomial expansion of slip velocity on the particles' surface [66, 8]. Effort on resolving the hydrodynamic interactions on such swimmers is still an ongoing subject. The far-field approximation of hydrodynamic interactions is often used in the squirmer model, in which the swimmers are represented as point dipoles and quadrupoles. Indeed, such far-field approximations are only relevant for dilute suspensions. The near-field and far-field approximation of two-body hydrodynamic interactions have been derived for squirmers [43, 118]. However, these approximations currently neglect the effect of intermediate-ranged hydrodynamic interactions. A recent alternative approach combines the two-body near-field analytical solutions with numerical computational fluid dynamics methods such as the boundary element method (BEM) [42]. Yet, the BEM is computationally expensive thus the method might not be scalable to discuss the collective behavior of squirmers. So for non-dilute active suspensions, there is a need for a computational model which takes the hydrodynamics into account accurately that can also deal with a large number of particles. Therefore, one may extend the LBM and lubrication correction method used in this thesis for active suspensions, whereas the bare LBM without lubrication corrections has been used to simulate squirmers in the dilute limit [69].

Appendix A

Details of persistent homology

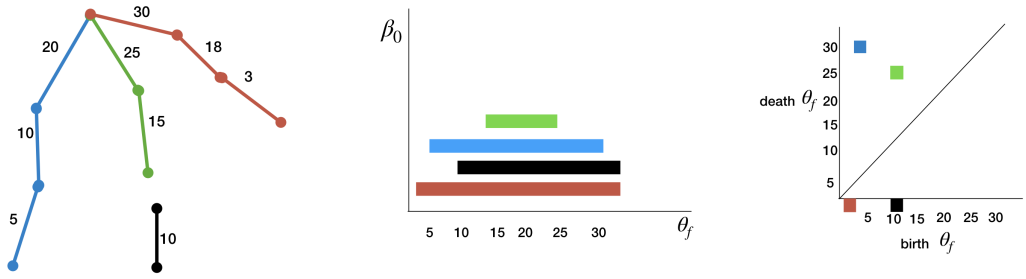

(a) (b) (c)

Fig. A.1 (a) An illustration of a force network configuration, where the numbers represent the force magnitude and the colors represent each connected component. (b) The corresponding barcode and (c) the corresponding persistence diagram.

In this Appendix, we briefly explain the procedure to plot a persistence diagram from a network configuration [29, 75]. First, let us consider a force network configuration as in Fig. A.1(a), where the numbers represent the force magnitude and the colors represent each connected component. Now, let us filter the force chains by increasing threshold θ_f, where a link in a network appears when the magnitude is greater than or equal to θ_f. Once a connected component appears during the filtration, we start to record its appearance in the barcode (Fig. A.1(b)). Note that when $\theta_f = 3$, first component (brown) appear, followed by the second component (blue) at $\theta_f = 5$. These are the birth θ_f for each connected component. As θ_f increases, more chains appear and the connected components grow. At $\theta_f = 25$, two connected components (blue and green) merge with each other. When merging of the connected component takes place, we adopt a rule such that a component that is born later in the filtration (which has higher birth θ_f) dies. In other words, at $\theta_f = 25$, component green (birth $\theta_f = 15$) dies since it merges with the component blue (birth $\theta_f = 5$). Then, at

$\theta_f = 30$, blue component merges with the brown component. Since $\theta_f = 30$ is the maximum value of the filtration, component brown will never die. Thus, we consider that it has infinite persistence. In addition, component black also never die since it does not merge with any other components until the end of the filtration. Finally, we plot the death and birth θ_f of each connected component in the persistence diagram (Fig. A.1(c)), where we assign death $\theta_f = -1$ for the connected components with infinite persistence. From this example, we demonstrate that persistent homology emphasizes more on the structure of each component rather than its total magnitude since: (i) Green component has higher total magnitude than the blue component, but the blue component has bigger life span (death $\theta_f -$ birth θ_f) and (ii) we ignore single link (black component) that is not merged with another component.

Appendix B

The dynamical Hertzian contact model

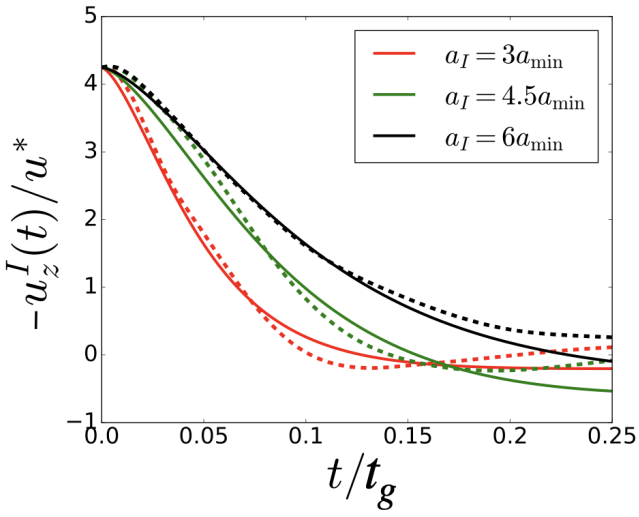

Fig. B.1 Plots of the speeds of impactors in the z-direction $u_z^I(t)/u^*$ against time (dashed lines) and the solution of Eq. (B.1) (solid lines) for $\phi = 0.54$ and $N = 2000$ with fitting parameters $A = 1.64 \times 10^5 m_0/(a_{\min} t_g^2)$ and $B = 6.48 \times 10^4 m_0/(a_{\min} t_g)$ for various a_I and $m_0 = 4\pi a_{\min}^3 \rho_f/3$.

In this Appendix, we explain the dynamical Hertzian contact model (DHCM) to explain the motion of the impactor [57, 14]. The equation motion for the deformation h of the Hertzian contact is written as

$$m_I \frac{d^2h}{dt^2} = -A\sqrt{a_I}h^{\frac{3}{2}} - B\sqrt{a_I}h^{\frac{1}{2}}\frac{dh}{dt}, \tag{B.1}$$

where A and B are fitting parameters which correspond to the elastic modulus and viscosity, respectively. In Fig. B.1, we plot the results of the simulation alongside with the solutions of Eq. (B.1). One can see that the results of the simulation agree with the model shortly after

the impact. We also clarified that the impact speed $u_z^I(t)$ clearly depends on the radius of impactor, which cannot be explained in the linear spring model used in Ref. [26].

We also evaluated the power-law relationships among u_0, $F_{\max}$, and $t_{\max}$ as in Eq. (4.9). However, Eq. (B.1) yields $6/5 < \alpha < 4/3$ and $-1/3 < \beta < -1/5$, which disagree with the simulation results in Chapter 4. Such disagreements are caused by the assumptions of the DHCM that are violated in our system. First, Hertzian theory essentially assumes that the liquid surface behaves as an elastic sheet when the penetration of the impactor is small. Yet, surface of the suspensions is different than an elastic sheet. As shown in Chapter 4, the elastic response takes place in the later stage after the impact when the impactor has penetrated much deeper than the surface of the suspensions. In addition, Hertzian theory also assumes that the surfaces are frictionless, which indeed violated in our cases since we consider the friction between the impactor and the suspended particles.

Appendix C

Analytical solution of the floating model

In this Appendix, we present the analytical solution of Eq. (4.6). The dimensionless form of Eq. (4.6) with the aid of a_I and $t_I = \sqrt{a_I/\tilde{g}}$ is written as

$$\ddot{z}_I^* = -1 - \eta^* \dot{z}_I^* |z_I^* - 1|, \tag{C.1}$$

where $z_I^* = z_I/a_I$, $t^* = t/t_I$, $\dot{z_I}^* = dz_I^*(t)/dt^* = -u_z^I/u^*$, $\ddot{z_I}^* = d^2 z_I^*(t)/dt^{*2}$, and $\eta^* = 3\pi\eta_{\text{eff}} a_I \sqrt{a_I/\tilde{g}}/m_I$. Then, Eq. (C.1) can be solved exactly in terms of the Airy functions as

$$z_I^*(t) = -\frac{\kappa[\text{Ai}'(\Phi)\text{Bi}'(\Theta) - \text{Ai}'(\Theta)\text{Bi}'(\Phi)]}{\gamma[\text{Bi}(\Phi)\text{Ai}'(\Theta) - \text{Ai}(\Phi)\text{Bi}'(\Theta)]}, \tag{C.2}$$

where $\gamma = (\eta^*)^{2/3}$, $\kappa = 2^{2/3}$, $\Theta = u_0^* \sqrt[3]{\eta^*/2}$, and $\Phi = (u_0^* + t^*)\sqrt[3]{\eta^*/2}$, where $u_0^* = u_0 t_I/a_I$. Here, $\text{Ai}(x)$ is the Airy function of the first kind, which is defined as $\text{Ai}(x) = \int_0^\infty \cos(t^3/3 + xt)dt/\pi$, and $\text{Ai}'(x)$ is its derivative. $\text{Bi}(x)$ is the Airy function of the second kind, which is defined as $\text{Bi}(x) = \int_0^\infty [\exp(-t^3/3 + xt) + \sin(-t^3/3 + xt)]dt/\pi$, and $\text{Bi}'(x)$ is its derivative. One can differentiate Eq. (C.2) two times to get the expression for $\ddot{z}_I$ as

$$\ddot{z}_I^* = -\frac{\left[\kappa\gamma^{\frac{3}{2}}\left(t^* - u_0^*\right)\left(\text{Ai}'(\Theta)\text{Bi}(\Phi) - \text{Ai}(\Phi)\text{Bi}'(\Theta)\right)^2\left(\text{Ai}'(\Theta)\text{Bi}'(\Phi) - \text{Ai}'(\Phi)\text{Bi}'(\Theta)\right) - \gamma\Lambda\right]}{\left(\text{Ai}'(\Theta)\text{Bi}(\Phi) - \text{Ai}(\Phi)\text{Bi}'(\Theta)\right)^3},$$

$$\begin{aligned}\Lambda =& \text{Ai}'(\Theta)^3\text{Bi}(\Phi)^3 + 2\text{Ai}'(\Theta)^3\text{Bi}'(\Phi)^3 \\ &- 3\text{Ai}(\Phi)\text{Ai}'(\Theta)^2\text{Bi}'(\Phi)^2\text{Bi}'(\Theta) - 6\text{Ai}'(\Phi)\text{Ai}'(\Theta)^2\text{Bi}'(\Phi)^2\text{Bi}'(\Theta) \\ &+ 3\text{Ai}(\Phi)^2\text{Ai}'(\Theta)\text{Bi}(\Phi)\text{Bi}'(\Theta)^2 + 6\text{Ai}'(\Phi)^2\text{Ai}'(\Theta)\text{Bi}'(\Phi)\text{Bi}'(\Theta)^2 \\ &+ \text{Ai}(\Phi)^3\text{Bi}'(\Theta)^3 - 2\text{Ai}'(\Phi)^3\text{Bi}'(\Theta)^3. \end{aligned} \tag{C.3}$$

To obtain the expression of $F_{\max}$ and $t_{\max}$, we adopt the short time expansion for Eq. (C.3) since $F_{\max}$ appears in the region $t/t_g \ll 1$, Thus, up to third order, one can obtain

$$\begin{aligned}\ddot{z}_I^* = &-1+\eta^* u_0^{*2} t^* + \frac{3\eta^* u_0^* t^{*2}}{2} \\ &- \left(\frac{2u_0^{*3}(\eta^*)^2}{3} - \frac{\eta^*}{2}\right) t^{*3} + \mathscr{O}\left(\left[\frac{t^*}{u_0^*}\right]^4\right).\end{aligned} \tag{C.4}$$

Then, we differentiate Eq. (C.4) to obtain $\dddot{z}_I^*$ as

$$\begin{aligned}\dddot{z}_I^* = &\eta^* u_0^{*2} + 3\eta^* u_0^* t^* \\ &- \left(\frac{2u_0^{*3}(\eta^*)^2}{3} - \frac{\eta^*}{2}\right) t^{*2} + \mathscr{O}\left(\left[\frac{t^*}{u_0^*}\right]^3\right).\end{aligned} \tag{C.5}$$

Then, for $\dddot{z}_I^* = 0$, one can solve the quadratic equation in Eq. (C.5) for $t_{\max}$ as

$$\frac{t_{\max}}{t_I} = \frac{3u_0^* + \sqrt{3u_0^{*2} + 8\eta^* u_0^{*5}}}{4\eta^* u_0^{*3} - 3}. \tag{C.6}$$

For $\eta^* u_0^* \gg 1$, Eq. (C.6) reduces to

$$\frac{t_{\max}}{t_I} \approx \frac{u_0^{*-\frac{1}{2}}}{\sqrt{2}}. \tag{C.7}$$

Thus, we confirm the exponent $\beta = -1/2$. To obtain $F_{\max}$, we plug Eq. (C.7) into Eq. (C.4) and take the limit $\eta^* u_0^* \gg 1$. Thus, for $F_{\max} = -m_I(\ddot{z}_I(t_{\max}))$ we obtain

$$\frac{F_{\max}}{m_I \tilde{g}} = u_0^{*\frac{3}{2}} \sqrt{\frac{2\eta^*}{9}}. \tag{C.8}$$

Thus, we confirm the exponent $\alpha = 3/2$ for large u_0. From Eq. (C.6), $t_{\max}$ diverges at $u_{0,c} = \sqrt[3]{3/4\eta^*}$. This result suggests the limitation of the short time approximation.

Appendix D

Determining the number of percolating force chains in the floating+force chains model

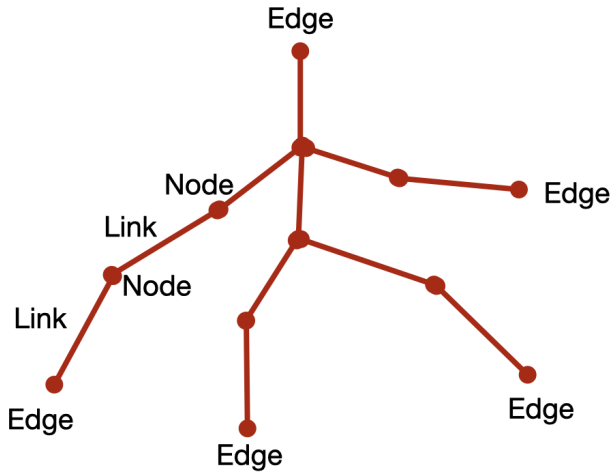

Fig. D.1 An illustration of the terminology in force chains. Lines represent the links, circles represent the nodes.

In this Appendix, we explain the algorithm to determine the connected force chains from the impactor to the bottom plate used in the floating + force chain model in Sec. 4.3.3. First of all, let us explain how we draw the force chains. Note that force chains are defined as a collection of nodes and links representing the contacting suspended particles (see Fig. D.1). Thus, for each pair of contacting suspended particles, we draw a network in which a node

represents the center of a contacting pair of particles and a link is a straight line connecting a pair of adjacent nodes. The initial force chains can be seen in Fig. D.2(a).

(a) (b) (c) (d)

Fig. D.2 Illustrations of the algorithm to determine $n(t)$ from force chains network. (a) An initial network of force chains. (b) The remaining chains after the lateral chains are removed. (c) All connected components after removing all edges that do not touch the impactor or bottom plate, where blue and red lines represent the corresponding connected components that self-loops and chains between the impactor and bottom plate, respectively. (d) Percolated force chains from the impactor to the bottom plate.

The algorithm to determine $n(t)$ is as follows. Since we are only interested in the force propagation in the vertical direction, we remove links that expand in the lateral directions (dangling chains). For this purpose, we remove all links in which the height difference $|z_i - z_j|$ for a contacting pair of particles i and j is less than the smallest radius of the suspended particles $a_{\min}$. The corresponding network after the removal of lateral chains can be seen in Fig. D.2(b).

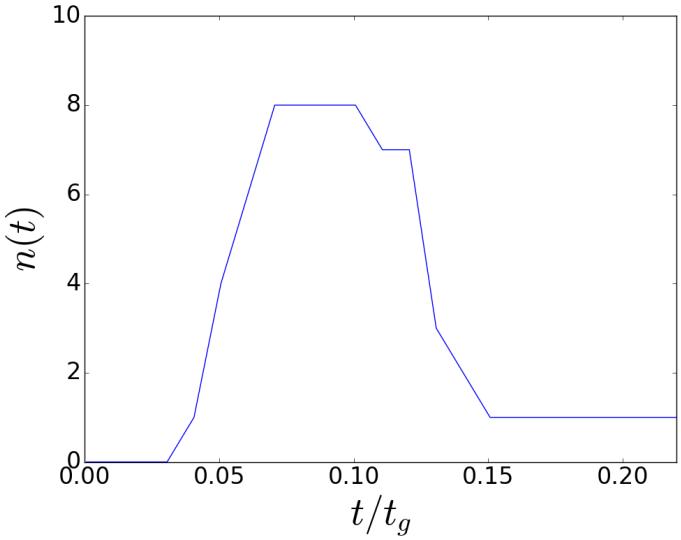

Fig. D.3 A plot of the number of connected force chains from the impactor to the bottom plate $n(t)$ against time for $\phi = 0.53$, $W = D = 6D_I$, and $H = 2D_I$ with $u_0 = 2.6u^*$.

Our goal is to determine connected networks from the impactor to the bottom plate. Thus, we remove all links to reach the edges of the force chains which do not touch the bottom plate nor the impactor. Once such links are removed, the leftover chains create new links at the edges of the force chain. We repeat these labeling and removal processes until there are no edges of dangling chains except for the edges which touch the bottom plate or the impactor. Then, we label each connected component (the blue and red connected components in Fig. D.2(c)).

Note that the connected components do not need to be percolated from the impactor to the bottom plate to survive in our algorithm at this stage due to the existence of connected edges which form a self-loop (blue connected components in Fig. D.2(c)). Therefore, we need to examine whether each connected component is percolated or not. Then, we remove non-percolated connected components (blue component) while keeping the percolated connected component (red component) as shown in Fig. D.2(d). Finally, we evaluate $n(t)$ by the number of links that touch the bottom plate. The above processes are illustrated in Fig. D.2 . The obtained $n(t)$ for $\phi = 0.53$, $W = D = 6D_I$, and $H = 2D_I$ with $u_0 = 2.6u^*$ against time is plotted in Fig. D.3.

Appendix E

Dependence of the existence of the power-law relations on volume fraction of the suspensions

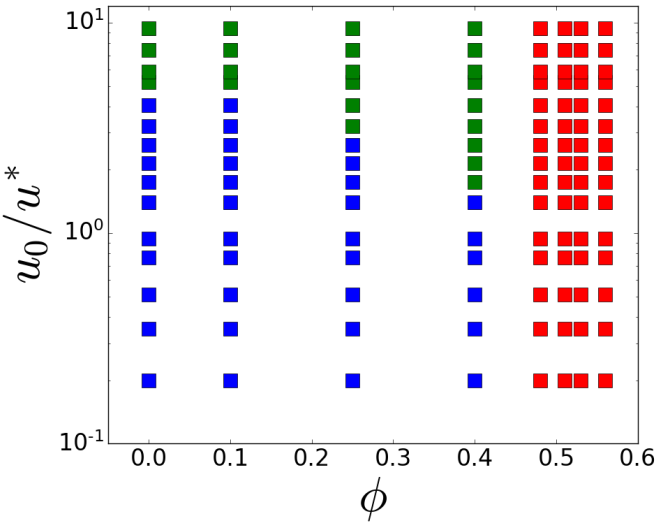

Fig. E.1 A phase diagram showing whether the impactor has $F_{\max}$ as a function of the volume fraction ϕ and the impact speed u_0 for $W = D = 6D_I$ and $H = 3D_I$. Red squares represent set of parameters where the relations among u_0, $F_{\max}$, and $t_{\max}$ can be explained by Eq. (4.6). Green squares are points where $F_{\max}$ exist but Eq. (4.6) fails. Blue squares are where $F_{\max}$ does not even exist.

In this Appendix, we have examined whether the relations among u_0, $F_{\max}$, and $t_{\max}$ only exist in the impact process in dense suspensions, though the rebound only exists in dense suspensions. We summarize the dependence on the volume fraction in the phase diagram in

Fig. E.1. Our simulation indicates that $F_{\max}$ only exists in all range of u_0 when $\phi \geq 0.48$, while $F_{\max}$ does not exist for dilute suspensions except for very high u_0. This result clarifies the role of suspensions in which our analysis in Chapter 4 is only valid for dense suspensions.

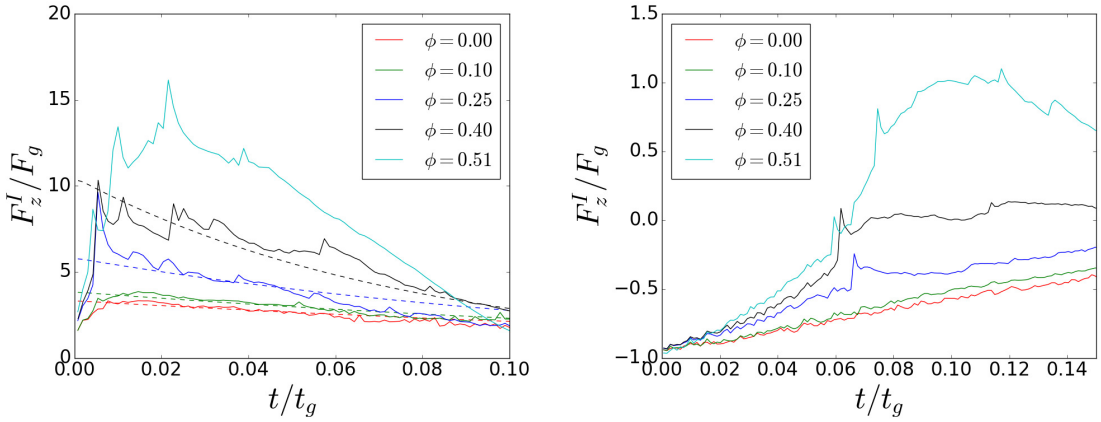

Fig. E.2 Plots of forces exerted on the impactor against time for various volume fractions for $W = D = 6D_I$ and $H = 3D_I$ for (a) $u_0/u^* = 5.84$ (Dashed lines represent the solutions of Eq. (E.1)) and (b) $u_0/u^* = 0.93$.

In Fig. E.2, we plot the force exerted on the impactor against time to clarify the difference between dense and dilute cases. For high u_0 (Fig. E.2(a)), $t_{\max}$ for the dilute case emerges earlier than that in the denser case. In addition, dilute cases have smaller $F_{\max}$. Such differences occur since the origin of $F_{\max}$ in a dilute case is different from that in the dense case. In dense situations, the dominant contribution is from the contact force between the impactor and the suspended particles, while for the dilute situations, the dominant contribution is from the hydrodynamic force exerted on the impactor [88]. For low u_0 (Fig. E.2(b)), one can see that $F_{\max}$ only exists in dense situation. Since the acceleration due to the gravity is dominant for low u_0, the sufficient drag resistance to compete with the gravity forces only exists for dense suspensions.

In Fig. E.3, we plot the deepest point of the impactor $|z|$ scaled by the impactor diameter D_I against time. Here, one can see that the impactor sinks right after the impact in dilute suspensions, while the impactor can keep its position near the surface for dense suspensions. The behavior in which the impactor stays for a while near the surface of the suspension is a characteristic of dense suspensions under impact. Thus, the floating model (Eq. (4.6)) cannot be used for dilute situations since the floating model assumes that the impactor is partially surrounded by fluid. We also summarize the region where Eq. (4.6) is applicable in Fig. E.1. When the impactor is completely sunk, the second term on the r.h.s. of Eq. (4.6) should be

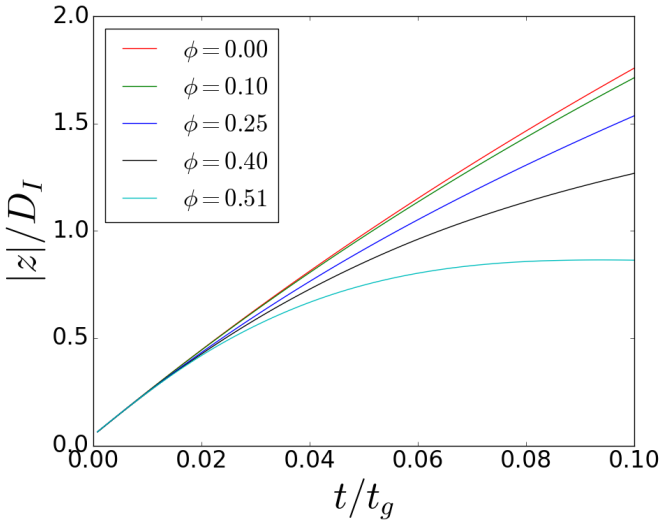

Fig. E.3 Plots of the deepest points of the impactor scaled by the diameter of the impactor for $u_0/u^* = 5.84$ for $W = D = 6D_I$ and $H = 3D_I$.

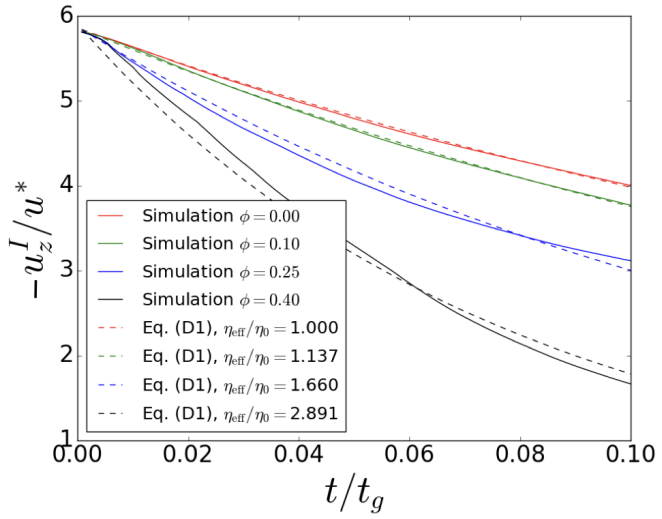

Fig. E.4 Plots of the velocities of the impactor for low volume fractions and for $W = D = 6D_I$ and $H = 3D_I$ alongside with the solutions of Eq. (E.1).

replaced by the Stokesian drag as

$$m_I \frac{d^2 z_I}{dt^2} = -m_I \tilde{g} - 3\pi \eta_{\text{eff}} a_I \dot{z}_I. \tag{E.1}$$

In Fig. E.4, we plot the impactor velocity against time alongside the solutions of Eq. (E.1) for the dilute cases. Note that Eq. (4.6) cannot describe even the behavior of the impactor velocity in dilute cases.

As expected, the apparent viscosity η_{eff}/η_0, where η_0 is the solvent viscosity, becomes larger as the volume fraction increases. Although the agreement between the solution of Eq. (E.1) and our simulation is remarkable for u_z^I (see Fig. E.4), Eq. (E.1) cannot capture $F_{\max}$ in dilute suspensions (see the dashed lines in Fig. E.2(a)). This is because there is no competition between time increasing and time decreasing contributions in Eq. (E.1). Although one may extend the studies on the impact process on water (without suspended particles) alone to dilute suspensions [78], such a problem is beyond the scope of this thesis.

References

[1] M. Alam, S. Saha, and R. Gupta. Unified theory for a sheared gas–solid suspension: from rapid granular suspension to its small-stokes-number limit. *J. Fluid Mech.*, **870**, pp. 1175–1193, 2019. URL http://dx.doi.org/10.1017/jfm.2019.304.

[2] B. Allen, B. Sokol, S. Mukhopadhyay, R. Maharjan, and E. Brown. System-spanning dynamically jammed region in response to impact of cornstarch and water suspensions. *Phys. Rev. E*, **97**:052603, pp. 1–9, 2018. URL https://doi.org/10.1103/PhysRevE.97.052603.

[3] H.A Barnes. Shear thickening ("dilatancy") in suspensions of nonaggregating solid particles dispersed in Newtonian liquids. *J. Rheol.*, **33**, pp. 329–366, 1989. URL https://doi.org/10.1122/1.550017.

[4] G. K. Batchelor. *An Introduction to Fluid Dynamics*. Cambridge University Press, 2000.

[5] A. S. Baumgarten and K. Kamrin. A general constitutive model for dense, fine-particle suspensions validated in many geometries. *Proc. Natl. Acad. Sci. U. S. A.*, **116**:42, pp. 20828–20836, 2019. URL https://doi.org/10.1073/pnas.1908065116.

[6] P. L. Bhatnagar, E. P. Gross, and M. Krook. A model for collision processes in gases. i. small amplitude processes in charged and neutral one component systems. *Phys. Rev.*, **94**:3, pp. 511–525, 1954. URL https://doi.org/10.1103/PhysRev.94.511.

[7] D. Bi, J. Zhang, B. Chakraborty, and R. P. Behringer. Jamming by shear. *Nature*, **480**, pp. 355–358, 2011. URL https://doi.org/10.1038/nature10667.

[8] J. R. Blake. A spherical envelope approach to ciliary propulsion. *J. Fluid. Mech.*, **46**:1, pp. 199–208, 1971. URL https://doi.org/10.1017/S002211207100048X.

[9] R. Blickhan. The spring-mass model for running and hopping. *J. Biomech.*, **22**:11, pp. 1217–1227, 1989. URL https://doi.org/10.1016/0021-9290(89)90224-8.

[10] L. Bocquet, J. Piasecki, and J.-P. Hansen. On the Brownian motion of a massive sphere suspended in a hard sphere fluid. 1. multiple-time-scale analysis and microscopic expression for the friction coefficient. *J. Stat. Phys.*, **76**, pp. 505–526, 1994. URL https://doi.org/10.1007/BF02188673.

[11] J. E. Brady and F. Senese. *Chemistry: Matter and Its Change (4th Edition)*. Wiley, 2004.

[12] J. F. Brady and G. Bossis. Stokesian dynamics. *Annu. Rev. Fluid Mech.*, **20**, pp. 111–157, 1988. URL https://doi.org/10.1146/annurev.fl.20.010188.000551.

[13] M. Brassard, N. Causley, N. Krizou, J. A. Dijksman, and A. H. Clark. Viscous-like forces control the impact response of shear-thickening dense suspensions. *J. Fluid. Mech.*, **923**:A38, pp. 1–17, 2021. URL https://doi.org/10.1017/jfm.2021.611.

[14] N. V. Brilliantov, F. Spahn, J-M. Hertzsch, and T. Poschel. Model for collisions in granular gases. *Phys. Rev. E*, **53**:5, pp. 5382–5392, 1996. URL https://doi.org/10.1103/PhysRevE.53.5382.

[15] E. Brown and H. M. Jaeger. The role of dilation and confining stresses in shear thickening of dense suspensions. *J. Rheol.*, **56**, pp. 875–923, 2012. URL https://doi.org/10.1122/1.4709423.

[16] E. Brown and H. M. Jaeger. Shear thickening in concentrated suspensions: phenomenology, mechanisms and relations to jamming. *Rep. Prog. Phys.*, **77**:4, pp. 046602–046625, 2014. URL https://doi.org/10.1088/0034-4885/77/4/046602.

[17] E. Brown, H. Zhang, N. A. Forman, B. W. Maynor, D. E. Betts, J. M. DeSimone, and H. M. Jaeger. Shear thickening and jamming in densely packed suspensions of different particle shapes. *Phys. Rev. E*, **84**:031408, pp. 1–11, 2011. URL https://doi.org/10.1103/PhysRevE.84.031408.

[18] G. Carlsson. Topology and data. *Bull. Am. Math. Soc.*, **46**, pp. 255–308, 2009. URL https://doi.org/10.1090/S0273-0979-09-01249-X.

[19] S. Chapman and T. G. Cowling. *The Mathematical Theory of Non-Uniform Gases*. Cambridge University Press, 1960.

[20] A. H. Clark, A. J. Petersen, L. Kondic, and R. P. Behringer. Nonlinear force propagation during granular impact. *Phys. Rev. Lett.*, **114**:144502, pp. 1–5, 2015. URL https://doi.org/10.1103/PhysRevLett.114.144502.

[21] R. I. Cukier, R. Kapral, and J. R. Mehaffey. Kinetic theory of the hydrodynamic interaction between 2 particles. *J. Chem. Phys*, **74**, pp. 2494–2504, 1981. URL https://doi.org/10.1063/1.441318.

[22] P. A. Cundall and O. D. L. Strack. A discrete numerical model for granular assemblies. *Geotechnique*, **29**, pp. 47–65, 1979. URL https://doi.org/10.1680/geot.1979.29.1.47.

[23] C. D. Cwalina, K. J. Harrison, and N. J. Wagner. Rheology of cubic particles suspended in a Newtonian fluid. *Soft Matter*, **12**, pp. 4654–4665, 2016. URL https://doi.org/10.1039/C6SM00205F.

[24] M. M. Denn, J. F. Morris, and D. Bonn. Shear thickening in concentrated suspensions of smooth spheres in Newtonian suspending fluids. *Soft Matter*, **14**, pp. 170–184, 2018. URL https://doi.org/10.1039/C7SM00761B.

[25] B. Derjaguin and L. D. Landau. Theory of the stability of strongly charged lyophobic sols and of the adhesion of strongly charged particles in solutions of electrolytes. *Acta Physicochim. U.R.S.S*, **14**, pp. 633–662, 1941. URL https://doi.org/10.1016/0079-6816(93)90013-L.

[26] K. Egawa and H. Katsuragi. Bouncing of a projectile impacting a dense potato-starch suspension layer. *Phys. Fluids*, **31**:053304, pp. 1–8, 2019. URL https://doi.org/10.1063/1.5095678.

[27] R. G. Egres and N. J. Wagner. The rheology and microstructure of acicular precipitated calcium carbonate colloidal suspensions through the shear thickening transition. *J. Rheol.*, **49**:3, pp. 719–746, 2005. URL https://doi.org/10.1122/1.1895800.

[28] A. Einstein. On the motion of small particles suspended in liquids at rest required by the molecular-kinetic theory of heat. *Ann. Phys. (Leipzig)*, **17**, pp. 549–560, 1905. URL https://doi.org/10.1002/andp.19053220806.

[29] M. Gameiro, A. Singh, L. Kondic, K. Mischaikow, and J. F. Morris. Interaction network analysis in shear thickening suspensions. *Phys. Rev. Fluids*, **5**:034307, pp. 1–21, 2020. URL https://doi.org/10.1103/PhysRevFluids.5.034307.

[30] V. Garzó, S. Tenneti, S. Subramaniam, and C. M. Hrenya. Enskog kinetic theory for monodisperse gas–solid flows. *J. Fluid Mech.*, **712**, pp. 129–168, 2012. URL http://dx.doi.org/10.1017/jfm.2012.404.

[31] G. Giusteri and R. Seto. A theoretical framework for steady-state rheometry in generic flow conditions. *J. Rheol.*, **623**, pp. 713–723, 2018. URL https://doi.org/10.1122/1.4986840.

[32] G. Giusteri and R. Seto. Shear jamming and fragility of suspensions in a continuum model with elastic constraints. *Phys. Rev. Lett.*, **127**:138001, pp. 1–5, 2021. URL https://link.aps.org/doi/10.1103/PhysRevLett.127.138001.

[33] Z. Guo, C. Zheng, and B. Shi. Discrete lattice effects on the forcing term in the lattice Boltzmann method. *Phys. Rev. E*, **65**:046308, pp. 1–6, 2002. URL https://doi.org/10.1103/PhysRevE.65.046308.

[34] E. Han, I. R. Peters, and H. M. Jaeger. High-speed ultrasound imaging in dense suspensions reveals impact-activated solidification due to dynamic shear jamming. *Nat. Commun.*, **7**:12243, pp. 1–8, 2016. URL https://doi.org/10.1038/ncomms12243.

[35] E. Han, M. Wyart, I. R. Peters, and H. M. Jaeger. Shear fronts in shear-thickening suspensions. *Phys. Rev. Fluids*, **3**:073301, pp. 1–20, 2018. URL https://doi.org/10.1103/PhysRevFluids.3.073301.

[36] E. Han, N. M. James, and H. M. Jaeger. Stress controlled rheology of dense suspensions using transient flows. *Phys. Rev. Lett.*, **123**:248002, pp. 1–6, 2019. URL https://link.aps.org/doi/10.1103/PhysRevLett.123.248002.

[37] H. Hayakawa and S. Takada. Kinetic theory of discontinuous rheological phase transition for a dilute inertial suspension. *Prog. Theor. Exp. Phys.*, **2019**:083J01, pp. 1–37, 2019. URL http://dx.doi.org/10.1093/ptep/ptz075.

[38] H. Hayakawa, S. Takada, and V. Garzó. Kinetic theory of shear thickening for a moderately dense gas-solid suspension: From discontinuous thickening to continuous thickening. *Phys. Rev. E*, **96**:042903, pp. 1–24, 2017. URL http://dx.doi.org/10.1103/physreve.96.042903.

[39] Y. Hiraoka, T. Nakamura, A. Hirata, E. G. Escolar, K. Matsue, and Y. Nishiura. Hierarchical structures of amorphous solids characterized by persistent homology. *Proc. Natl. Acad. Sci. U. S. A.*, **113**:26, pp. 7035–7040, 2016. URL https://doi.org/10.1073/pnas.1520877113.

[40] L. C. Hsiao, S. Jamali, E. Glynos, P. F. Green, R. G. Larson, and M. J. Solomon. Rheological state diagrams for rough colloids in shear flow. *Phys. Rev. Lett.*, **119** :1158001, pp. 1–6, 2017. URL https://doi.org/10.1103/PhysRevLett.119.158001.

[41] K. Ichiki, A. E. Kobryn, and A. Kovalenko. Resistance functions for two unequal spheres in linear flow at low Reynolds number with the navier slip boundary condition. arXiv:1302.0461, 2013. URL https://arxiv.org/abs/1302.0461.

[42] T. Ishikawa. Lubrication theory and boundary element hybrid method for calculating hydrodynamic forces between particles in near contact. *J. Comput. Phys.*, **452**:110913, pp. 1–18, 2022. URL https://doi.org/10.1016/j.jcp.2021.110913.

[43] T. Ishikawa, M. P. Simmonds, and T. J. Pedley. Hydrodynamic interaction of two swimming model micro-organisms. *J. Fluid. Mech*, **568**, pp. 119–160, 2006. URL https://doi.org/10.1017/S0022112006002631.

[44] J. Israelachvili. *Intermolecular and Surface Forces*. Academic Press, 3 edition, 2011.

[45] D. J. Jeffrey. The calculation of the low Reynolds number resistance functions for two unequal spheres. *Phys. Fluids A: Fluid Dynamics*, **4**:1, pp. 16–29, 1992. URL https://doi.org/10.1063/1.858494.

[46] D. J. Jeffrey and Y. Onishi. Calculation of the resistance and mobility functions for two unequal rigid spheres in low-Reynolds-numberflow. *J. Fluid Mech*, **139**, pp. 261–290, 1984. URL https://doi.org/10.1017/S0022112084000355.

[47] K. P. Khrisnaraj and P. R. Nott. Coherent force chains in disordered granular materials emerge from a percolation of quasilinear clusters. *Phys. Rev. Lett.*, **124**:198002, pp. 1–6, 2020. URL https://doi.org/10.1103/PhysRevLett.124.198002.

[48] S. Kim and S. J. Karrila. *Microhydrodynamics: Principles and Selected Applications*. Butterworth-Heinemann, 1991.

[49] D. L. Koch and R. J. Hill. Inertial effects in suspension and porous media flows. *Annu. Rev. Fluid Mech.*, **33**:1, pp. 619–647, 2001. URL http://dx.doi.org/10.1146/annurev.fluid.33.1.619.

[50] D. L. Koch and A. S. Sangani. Particle pressure and marginal stability limits for a homogeneous monodisperse gas-fluidized bed: kinetic theory and numerical simulations. *J. Fluid Mech.*, **400**, pp. 229–263, 1999. URL http://dx.doi.org/10.1017/s0022112099006485.

[51] L. Kondic, X. Fang, W. Losert, C. S. O'Hern, and R. P. Behringer. Microstructure evolution during impact on granular matter. *Phys. Rev. E*, **85**:011305, pp. 1–17, 2012. URL https://doi.org/10.1103/PhysRevE.85.011305.

[52] C. Korner, M. Thies, T. Hofmann, N. Thurey, and U. Rude. Lattice Boltzmann model for free surface flow for modeling foaming. *J. Stat. Phys.*, **121**, pp. 179–196, 2005. URL https://doi.org/10.1007/s10955-005-8879-8.

[53] M. Kramar, A. Goullet, L. Kondic, and K. Mischaikow. Evolution of force networks in dense particulate media. *Phys. Rev. E*, **90**:052203, pp. 1–12, 2014. URL https://doi.org/10.1103/PhysRevE.90.052203.

[54] I. M. Krieger. Rheology of monodisperse latices. *Adv. Colloid Interface Sci.*, **3**, pp. 111–136, 1972. URL https://doi.org/10.1016/0001-8686(72)80001-0.

[55] N. Krizou and A. H. Clark. Power-law scaling of early-stage forces during granular impact. *Phys. Rev. Lett.*, **124**:178002, pp. 1–5, 2020. URL https://doi.org/10.1103/PhysRevLett.124.178002.

[56] P. M. Kulkarni and J. F. Morris. Suspension properties at finite Reynolds number from simulated shear flow. *Phys. Fluids*, **20**:040602, pp. 1–13, 2008. URL https://doi.org/10.1063/1.2911017.

[57] G. Kuwabara and K. Kono. Restitution coefficient in a collision between two spheres. *Jpn. J. Appl. Phys.*, **26**, pp. 1230–1233, 1987. URL https://doi.org/10.1143/JJAP.26.1230.

[58] A. J. C. Ladd. Numerical simulations of particulate suspensions via a discretized Boltzmann equation. part 1. theoretical foundation. *J. Fluid Mech*, **271**, pp. 285–309, 1994. URL https://doi.org/10.1017/S0022112094001771.

[59] A. J. C. Ladd. Numerical simulations of particulate suspensions via a discretized Boltzmann equation. part 2. numerical simulations. *J. Fluid Mech*, **271**, pp. 311–339, 1994. URL https://doi.org/10.1017/S0022112094001783.

[60] Y. K. Lee, K. H. Ahn, and S. J. Lee. Local shear stress and its correlation with local volume fraction in concentrated non-Brownian suspensions: Lattice Boltzmann simulation. *Phys. Rev. E*, **90**:062317, pp. 1–6, 2014. URL https://doi.org/10.1103/PhysRevE.90.062317.

[61] Y. K. Lee, J. Nam, K. Hyun, K. H. Ahn, and S. J. Lee. Rheology and microstructure of non-Brownian suspensions in the liquid and crystal coexistence region: strain stiffening in large amplitude oscillatory shear. *Soft Matter*, **11**, pp. 4061–4074, 2015. URL https://doi.org/10.1039/C5SM00180C.

[62] Y. S. Lee, E. D. Wetzel, and N. J. Wagner. The ballistic impact characteristics of kevlar woven fabrics impregnated with a colloidal shear thickening fluid. *J. Mater. Sci.*, **38**, pp. 2825–2833, 2003. URL https://doi.org/10.1023/A:1024424200221.

[63] A. Leonardi. Ph.D Thesis, ETH Zurich, 2015.

[64] A. Leonardi, F. K. Wittel, M. Mendoza, and H. J. Hermann. Coupled dem-lbm method for the free-surface simulation of heterogeneous suspensions. *Comp. Part. Mech.*, **1**, pp. 3–13, 2014. URL https://doi.org/10.1007/s40571-014-0001-z.

[65] A. Leonardi, M. Cabrera, F. K. Wittel, R. Kaitna, M. Mendoza, W. Wu, and H. J. Herrmann. Granular-front formation in free-surface flow of concentrated suspensions. *Phys. Rev. E*, **92**:052204, pp. 1–13, 2015. URL https://doi.org/10.1103/PhysRevE.92.052204.

[66] M. J. Lighthill. On the squirming motion of nearly spherical deformable bodies through liquids at very small reynolds numbers. *Commun. Pure Appl. Math.*, **5**:2, pp. 109–118, 1952. URL https://doi.org/10.1002/cpa.3160050201.

[67] A. J. Liu and S. R. Nagel. Jamming is not just cool any more. *Nature*, **396**, pp. 21–22, 1998. URL https://doi.org/10.1038/23819.

[68] A. J. Liu and S. R. Nagel. Granular and jammed materials. *Soft Matter*, **6**, pp. 2869, 2010. URL DOIhttps://doi.org/10.1039/C005388K.

[69] I. Llopis and I. Pagonabarraga. Hydrodynamic interactions in squirmer motion: Swimming with a neighbour and close to a wall. *J. Non-Newton. Fluid. Mech.*, **165**:17, pp. 946–952, 2010. URL https://doi.org/10.1016/j.jnnfm.2010.01.023.

[70] S. Luding. Cohesive, frictional powders: contact models for tension. *Granul. Matter.*, **10**, pp. 235–246, 2008. URL https://doi.org/10.1007/s10035-008-0099-x.

[71] R. Maharjan, S. Mukhopadhyay, B. Allen, T. Storz, and E. Brown. Constitutive relation for the system-spanning dynamically jammed region in response to impact of cornstarch and water suspensions. *Phys. Rev. E*, **97**:052602, pp. 1–13, 2018. URL https://doi.org/10.1103/PhysRevE.97.052602.

[72] R. Mari and R. Seto. Shear thickening, frictionless and frictional rheologies in non-Brownian suspensions. *J. Rheol.*, **58**, pp. 1693–1724, 2014. URL https://doi.org/10.1122/1.4890747.

[73] R. Mari, R. Seto, J. F. Morris, and M. M. Denn. Discontinuous shear thickening in Brownian suspensions by dynamic simulation. *Proc. Natl. Acad. Sci. U. S. A.*, **112**, pp. 15326–15330, 2015. URL https://doi.org/10.1073/pnas.1515477112.

[74] G. R. McNamara and G. Zanetti. Use of the Boltzmann equation to simulate lattice-gas automata. *Phys. Rev. Lett.*, **61**:20, pp. 2332–2335, 1988. URL https://doi.org/10.1103/PhysRevLett.61.2332.

[75] K. Mischaikow and V. Nanda. Morse theory for filtrations and efficient computation of persistent homology. *Dicrete. Comput. Geom*, **50**, pp. 330–353, 2013. URL https://doi.org/10.1007/s00454-013-9529-6.

[76] R. Mittal and G. Iaccarino. Immersed boundary methods. *Annu. Rev. Fluid Mech.*, **37**:1, pp. 239–261, 2005. URL https://doi.org/10.1146/annurev.fluid.37.061903.175743.

[77] Y. Miyazaki, M. Usawa, S. Kawai, J. Yee, M. Muto, and Y. Tagawa. Dynamic mechanical interaction between injection liquid and human tissue simulant induced by needle-free injection of a highly focused microjet. *Sci Rep*, **11**:14544, pp. 1–10, 2021. URL http://dx.doi.org/10.1038/s41598-021-94018-6.

[78] M. Moghisi and P. T. Squire. An experimental investigation of the initial force of impact on a sphere striking a liquid surface. *J. Fluid. Mech.*, **108**, pp. 133–146, 1981. URL https://doi.org/10.1017/S0022112081002036.

[79] S. Mukhopadhyay, B. Allen, and E. Brown. Testing constitutive relations by running and walking on cornstarch and water suspensions. *Phys. Rev. E*, **97**:052604, pp. 1–11, 2018. URL https://doi.org/10.1103/PhysRevE.97.052604.

[80] C. Ness, R. Seto, and R. Mari. The physics of dense suspensions. *Ann. Rev. Condens. Matter Phys.*, **13**:1, pp. 97–117, 2022. URL https://doi.org/10.1146/annurev-conmatphys-031620-105938.

[81] N. Q. Nguyen and A. J. C. Ladd. Lubrication corrections for lattice-Boltzmann simulations of particle suspensions. *Phys. Rev. E*, **66**:046708, pp. 1–12, 2002. URL https://doi.org/10.1103/PhysRevE.66.046708.

[82] N. Q. Nguyen and A. J. C. Ladd. Sedimentation of hard-sphere suspensions at low Reynolds number. *J. Fluid Mech*, **255**, pp. 73–104, 2005. URL https://doi.org/10.1017/S0022112004002563.

[83] M. Otsuki and H. Hayakawa. Critical scaling near jamming transition for frictional granular particles. *Phys. Rev. E*, **83**:051301, pp. 1–9, 2011. URL https://doi.org/10.1103/PhysRevE.83.051301.

[84] M. Otsuki and H. Hayakawa. Shear jamming, discontinuous shear thickening, and fragile states in dry granular materials under oscillatory shear. *Phys. Rev. E*, **101**:032905, pp. 1–8, 2020. URL https://link.aps.org/doi/10.1103/PhysRevE.101.032905.

[85] C. S. Peskin. Flow patterns around heart valves: A numerical method. *J. Comput. Phys.*, **10**, pp. 252–271, 1972. URL https://doi.org/10.1016/0021-9991(72)90065-4.

[86] I. R. Peters, S. Majumdar, and H. M. Jaeger. Direct observation of dynamic shear jamming in dense suspensions. *Nature*, **532**, pp. 214–217, 2016. URL https://doi.org/10.1038/nature17167.

[87] Pradipto and H. Hayakawa. Simulation of dense non-Brownian suspensions with the lattice Boltzmann method: shear jammed and fragile states. *Soft Matter*, **16**, pp. 945–959, 2020. URL https://doi.org/10.1039/C9SM00850K.

[88] Pradipto and H. Hayakawa. Impact-induced hardening in dense frictional suspensions. *Phys. Rev. Fluids*, **6**:033301, pp. 1–17, 2021. URL https://doi.org/10.1103/PhysRevFluids.6.033301.

[89] Pradipto and H. Hayakawa. Viscoelastic response of impact process on dense suspensions. *Phys. Fluids*, **33**:093110, pp. 1–12, 2021. URL https://doi.org/10.1063/5.0061196.

[90] Pradipto and H. Hayakawa. Effective viscosity and elasticity of dynamically jammed region and their role for the hopping motion on dense suspensions. arXiv:2205.13822, 2022.

[91] Pradipto and H. Hayakawa. Correction: Simulation of dense non-Brownian suspensions with the lattice Boltzmann method: shear jammed and fragile states. *Soft Matter*, **18**, pp. 685–686, 2022. URL http://dx.doi.org/10.1039/D1SM90226A.

[92] J. G. Puckett, F. Lechenault, and K. E. Daniels. Local origins of volume fraction fluctuations in dense granular materials. *Phys. Rev. E*, **83**:041301, pp. 1–8, 2011. URL https://doi.org/10.1103/PhysRevE.83.041301.

[93] M. H. Raibert and E. R. Tello. Legged robots that balance. *IEEE Expert*, **1**:4, pp. 89–89, 1986. URL https://doi.org/10.1109/MEX.1986.4307016.

[94] P. Raiskinmaki, J. A. Åstrom, M. Kataja, M. Latva-Kokko, A. Koponen, A. Jasberg, and A. Shakib-Manesh. Clustering and viscosity in a shear flow of a particulate suspension. *Phys. Rev. E*, **68**:061403, pp. 1–5, 2003. URL https://doi.org/10.1103/PhysRevE.68.061403.

[95] M. Roche, E. Myftiu, M. C. Johnston, P. Kim, and H. A. Stone. Dynamic fracture of nonglassy suspensions. *Phys. Rev. Lett.*, **110**:148304, pp. 1–5, 2013. URL https://doi.org/10.1103/PhysRevLett.110.148304.

[96] C. H. Rycroft. A three-dimensional voronoi cell library in c++. *Chaos*, **19**:041111, pp. 1, 2009. URL https://doi.org/10.1063/1.3215722.

[97] S. Saha and M. Alam. Revisiting ignited–quenched transition and the non-newtonian rheology of a sheared dilute gas–solid suspension. *J. Fluid Mech.*, **833**, pp. 206–246, 2017. URL http://dx.doi.org/10.1017/jfm.2017.722.

[98] S. Saha and M. Alam. Burnett-order constitutive relations, second moment anisotropy and co-existing states in sheared dense gas–solid suspensions. *J. Fluid Mech.*, **887**, 2020. URL http://dx.doi.org/10.1017/jfm.2019.1069.

[99] K. Saitoh and H. Hayakawa. Quantitative test of the time dependent gintzburg-landau equation for sheared granular flow in two dimensions. *Phys. Fluids*, **25**:070606, pp. 1–13, 2013. URL https://doi.org/10.1063/1.4812816.

[100] A. S. Sangani, G. Mo, H. Tsao, and D. L. Koch. Simple shear flows of dense gas-solid suspensions at finite stokes numbers. *J. Fluid Mech.*, **313**, pp. 309–341, 1996. URL http://dx.doi.org/10.1017/s0022112096002224.

[101] R. Seto, R. Mari, J. F. Morris, and M. M. Denn. Discontinuous shear thickening of frictional hard-sphere suspensions. *Phys. Rev. Lett.*, **111**:218301, pp. 1–5, 2013. URL https://doi.org/10.1103/PhysRevLett.111.218301.

[102] L. E. Silbert. Jamming of frictional spheres and random loose packing. *Soft Matter*, **6**, pp. 2918–2924, 2010. URL https://doi.org/10.1039/C001973A.

[103] A. Singh, R. Mari, M. M. Denn, and J. F. Morris. A constitutive model for simple shear of dense frictional suspensions. *J. Rheol.*, **62**, pp. 457–468, 2018. URL https://doi.org/10.1122/1.4999237.

[104] S. Succi. *The lattice Boltzmann equation: for fluid dynamics and beyond*. Oxford University Press, 2001.

[105] K. Suzuki and H. Hayakawa. Theory for the rheology of dense non-Brownian suspensions: divergence of viscosities and μ–J rheology. *J. Fluid Mech*, **864**, pp. 1125–1176, 2019. URL https://doi.org/10.1017/jfm.2019.5.

[106] O. Švec, J. Skocek, H. Stang, M. R. Geiker, and N. Roussel. Free surface flow of a suspension of rigid particles in a non-Newtonian fluid: A lattice Boltzmann approach. *J. Non-Newton. Fluid.*, **179-180**, pp. 32–42, 2012. URL https://doi.org/10.1016/j.jnnfm.2012.05.005.

[107] Y. Tagawa, N. Oudalov, A. E. Ghalbzouri, C. Sun, and D. Lohse. Needle-free injection into skin and soft matter with highly focused microjets. *Lab Chip*, **13**, pp. 1357–1363, 2013. URL http://dx.doi.org/10.1039/C2LC41204G.

[108] S. Takada, H. Hayakawa, A. Santos, and V. Garzó. Enskog kinetic theory of rheology for a moderately dense inertial suspension. *Phys. Rev. E*, **102**:022907, pp. 1–23, 2020. URL http://dx.doi.org/10.1103/physreve.102.022907.

[109] T. Takahashi, A. H. Clark, T. Majmudar, and L. Kondic. Granular response to impact: Topology of the force networks. *Phys. Rev. E*, **97**:012906, pp. 1–10, 2018. URL https://doi.org/10.1103/PhysRevE.97.012906.

[110] J. E. Thomas, K. Ramola, A. Singh, R. Mari, J. F. Morris, and B. Chakraborty. Microscopic origin of frictional rheology in dense suspensions: Correlations in force space. *Phys. Rev. Lett.*, **121**:128002, pp. 1–6, 2018. URL https://doi.org/10.1103/PhysRevLett.121.128002.

[111] H. Tsao and D. L. Koch. Simple shear flows of dilute gas–solid suspensions. *Journal of Fluid Mechanics*, **296**, pp. 211–245, 1995. URL https://doi.org/10.1017/S0022112095002114.

[112] E. J. W. Verwey and J. Th. G. Overbeek. *Theory of the Stability of Lyophobic Colloids: The Interaction of Sol Particles Having an Electric Double Layer*. Elsevier, 1948.

[113] S. von Kann, J. H. Snoeijer, D. Lohse, and D. van der Meer. Nonmonotonic settling of a sphere in a cornstarch suspension. *Phys. Rev. E*, **84**:060401(R), pp. 1–4, 2011. URL https://doi.org/10.1103/PhysRevE.84.060401.

[114] S. R. Waitukaitis and H. M. Jaeger. Impact-activated solidification of dense suspensions via dynamic jamming fronts. *Nature*, **487**, pp. 205–209, 2012. URL https://doi.org/10.1038/nature11187.

[115] S. R. Waitukaitis, L. K. Roth, V. Vitelli, and H. M. Jaeger. Dynamic jamming fronts. *EPL*, **102**:4, pp. 44001, 2013. URL https://doi.org/10.1209/0295-5075/102/44001.

[116] R. V. Williamson and W. W. Heckert. Some properties of dispersions of the quicksand type. *Ind. Eng. Chem*, **23**:6, pp. 667–670, 1931.

[117] M. Wyart and M. E. Cates. Discontinuous shear thickening without inertia in dense non-Brownian suspensions. *Phys. Rev. Lett.*, **112**:098302, pp. 1–5, 2014. URL https://doi.org/10.1103/PhysRevLett.112.098302.

[118] N. Yoshinaga and T. B. Liverpool. Hydrodynamic interactions in dense active suspensions: From polar order to dynamical clusters. *Phys. Rev. E*, **96**:020603, pp. 1–6, 2017. URL https://doi.org/10.1103/PhysRevE.96.020603.

[119] J. Zhang, Behringer R. P., and I. Goldhirsch. Coarse-graining of a physical granular system. *Prog. Theor. Phys.*, **184**, pp. 16–30, 2010. URL https://doi.org/10.1143/PTPS.184.16.